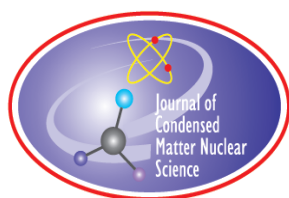


JOURNAL OF CONDENSED MATTER NUCLEAR SCIENCE

Experiments and Methods in Cold Fusion

**Proceedings of the 11th International Workshop
on Anomalies in Hydrogen Loaded Metals,
Toulouse, October 15–16, 2015**

VOLUME 23, May 2017



JOURNAL OF CONDENSED MATTER NUCLEAR SCIENCE

Experiments and Methods in Cold Fusion

Editor-in-Chief

Jean-Paul Biberian
Marseille, France

Editorial Board

Peter Hagelstein
MIT, USA

Xing Zhong Li
Tsinghua University, China

Edmund Storms
KivaLabs, LLC, USA

George Miley
*Fusion Studies Laboratory,
University of Illinois, USA*

Michael McKubre
SRI International, USA

JOURNAL OF CONDENSED MATTER NUCLEAR SCIENCE

Volume 23, May 2017

© 2017 ISCMNS. All rights reserved. ISSN 2227-3123

This journal and the individual contributions contained in it are protected under copyright by ISCMNS and the following terms and conditions apply.

Electronic usage or storage of data

JCMNS is an open-access scientific journal and no special permissions or fees are required to download for personal non-commercial use or for teaching purposes in an educational institution.

All other uses including printing, copying, distribution require the written consent of ISCMNS.

Permission of the ISCMNS and payment of a fee are required for photocopying, including multiple or systematic copying, copying for advertising or promotional purposes, resale, and all forms of document delivery.

Permissions may be sought directly from ISCMNS, E-mail: CMNSEditor@iscmns.org. For further details you may also visit our web site: <http://www.iscmns.org/CMNS/>

Members of ISCMNS may reproduce the table of contents or prepare lists of articles for internal circulation within their institutions.

Orders, claims, author inquiries and journal inquiries

Please contact the Editor in Chief, CMNSEditor@iscmns.org or webmaster@iscmns.org



JOURNAL OF CONDENSED MATTER NUCLEAR SCIENCE

Volume 23

2017

CONTENTS

PREFACE

RESEARCH ARTICLES

- | | |
|---|----|
| A Study on the Possibility of Initiating Tungsten Alpha Decay Using Electric Explosion
<i>L.I. Urutskoev, D.V. Filippov, D.A. Voitenko, G.I. Astapenko, A.O. Birykov, A.A. Markoliya and K.A. Alabin</i> | 1 |
| Simulation of the Behavior of Exotic Neutral Particles by a Monte-Carlo Modelisation
<i>Jacques Ruer</i> | 27 |
| Nuclear Catalysis Mediated by Localized Anharmonic Vibrations
<i>Vladimir Dubinko</i> | 45 |
| Electron Deep Orbits of the Hydrogen Atom
<i>J.L. Paillet and A. Meulenberg</i> | 62 |
| Calorimetric Investigation of Anomalous Heat Production in Ni–H Systems
<i>K.P. Budko and A.I. Korshunov</i> | 85 |
| Perspective on Low Energy Bethe Nuclear Fusion Reactor with Quantum Electronic Atomic Rearrangement of Carbon
<i>Stephane Neuville</i> | 91 |

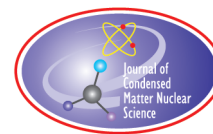
Preface

ISCMNS workshop 15–16 October 2015

The workshop was sponsored by Airbus and held at their Blagnac Center near Toulouse, signifying that this company is interested in the LENR field. About 50 people attended the event, mainly from France but also seven from Russia and seven from the U.S. There were 15 presentations and a lot of discussions, sometimes passionate! While it might seem normal that French researchers should attend a conference in their own country, still, it was good to see so many French researchers present their work in the LENR field, showing that LENR science is as much alive and well in France as it is in the rest of Europe. In addition, the workshop was the occasion for the French to announce a conference in French, which took place in Avignon on March 2016. Industries, in addition to Airbus, were also well represented showing that LENR is of interest to the industrial sector. As one of the organizers, together with William Collis and Jenny Darja Vinko, I would like to thank all those who have participated and I hope that they had a good time in Toulouse.

Sincerely,

Jean-François Geneste
(Airbus Group)
May 2017



Research Article

A Study on the Possibility of Initiating Tungsten Alpha Decay Using Electric Explosion

L.I. Urutskoev*

The Russian Presidential Academy of National Economy and Public Administration (RANEPA), 82/5 Prospect Vernadskogo, Moscow 119571, Russian Federation

D.V. Filippov

Russian Foreign Trade Academy of the Ministry for Economic Development of the Russian Federation (RFTA), 4A Pudovkina Str., Moscow 119285, Russia

A.O. Birykov

Presidential Executive Office

G.I. Astapenko, D.A. Voitenko and A.A. Markoliya

Sukhumi Institute of Physics and Technology, Sukhumi, Republic of Abkhazia, 665 Kodori Highway, Sukhumi, Republic of Abkhazia

K.A. Alabin

Prokhorov General Physics Institute, Russian Academy of Sciences, Vavilov Str. 38, 119991 Moscow, Russia

Abstract

Experiments with electric explosion of tungsten wires are described. These are intended to check the results of G.L. Wendt and C.E. Irion's experiments published in 1922. The historical and theoretical background of this study are described in detail. The gas phase formed in the chamber after the electric explosion was carefully studied in the experiments. The results of the study do not contradict with the results of the Wendt and Irion experiments.

© 2017 ISCMNS. All rights reserved. ISSN 2227-3123

Keywords: Alpha- beta-decay, Alpha-decay, Electrical explosion of conductors, Gas phase analysis, Gas mass-spectrometer, Optical spectral line

*Corresponding author. E-mail: urleon@yandex.ru

1. Historical Background, Experiment of G.L. Wendt and C.E. Irion [1]

In the second decade of the last century, work on the use of electric explosion of conductors (EEC) for laboratory simulation of astrophysical processes were started in the United States. The pioneer of this new research field was John August Anderson, who demonstrated that by using a high-current EEC one can reach very high temperatures [2]. The temperature of the plasma, which was generated by electric explosion of wire, was $T \approx 2 \times 10^4$ K as estimated by Anderson using the luminance method [2]. It was the highest recorded temperature obtained under laboratory conditions up to that time. Staff at the Chicago University chemical laboratory, Gerald Wendt and Clarence Irion, decided to use the electric explosion method developed by J. Anderson to test a hypothesis. Their hypothesis was based on two facts firmly established by then: the temperature of the sun surface is about 6×10^3 K and there are no characteristic optical lines of heavy chemical elements in the visible spectrum.

Based on these facts, Wendt and Irion suggested that the absence of the spectral lines of heavy chemical elements in the radiation spectrum of the sun and other stars can be explained by the fact that heavy chemical elements are unstable at solar temperatures.

In 1919, E. Rutherford, using high energy α -particles, was able to produce a nuclear reaction of ^{14}N nuclei. Thus, the fundamental possibility of nuclear reactions in laboratory conditions was demonstrated. However, in the early 1920s, the difference in scale of energies of atomic and nuclear phenomena was not yet been fully understood. Probably, therefore, the emergence of the Irion and Wendt hypothesis did not trigger strong rejection in the scientific community, as it would have if such a hypothesis had been proposed 5 or 10 years later.

The idea of the experiment of Wendt and Irion was to pass a strong electric current through a tungsten wire, thereby heating it up to 2×10^4 K, and then observe the decomposition of W atoms. Since the methods of solid state mass spectrometry were not yet developed at the time, the main diagnostic objective of the experiment was the spectrum analysis of gas generated after the electric explosion of tungsten wire.

A capacitor ($C = 0.1\text{mkF}$) charged to $Vd = 35$ kV was used to create a current pulse in the experiment [1]. The high-voltage discharge switching was done using an untriggered discharger. Electric explosion of tungsten wire was conducted in a spherical bulb made of Pyrex glass. Tungsten wire, length $l = 40$ mm and diameter $d = 35$ mm, was placed “as a spacer” between the two tungsten electrodes that were sealed in the bulb at two opposite sides. In equatorial cross section, with respect to the electrodes, the “spectral” electrode was sealed. It served as one of the electrodes for the ignition of plasma discharge in the gas formed after the electric explosion.

It should be emphasized that the preparations for the experiments were carried out very carefully. Before the electric explosion of wire the inner surface of the bulb was heated in oven continuously for 15 h at $t = 300^\circ\text{C}$ simultaneously with evacuation. At the same time with the heating of the glass bulb an electric current was passed through the tungsten wire which heated it to a temperature of $\sim 2000^\circ\text{C}$. After completion of the degassing procedure, the glass tube connecting the flask to a mercury pump was melted using a burner, and sealed.

The volume of gas generated after the EEC, averaged over the 21 shots, was $V \approx 1\text{ cm}^3$ (under normal conditions), i.e. about 10^{19} particles. The volume of gas observed after EEC was so large that an attempt to explain its appearance due to the release of gas previously dissolved or absorbed by the wire seemed very unlikely to the authors. The average volume of gas produced was 26 500 times more than an average volume of wire (0.0381 cm^3).

According to the authors of this work, the spectral analysis of gas formed by electric explosion, revealed the presence of the characteristic bright-yellow line of helium (^4He) in all of the experiments. Another no less important statement was the fact that the spectral analysis did not show any characteristic lines of hydrogen. This fact indicates the exceptional care taken in these experiments because, it is well known, getting rid of water vapor on the chamber glass walls and hydrogen dissolved in a tungsten wire is a very difficult task. Moreover, according to the authors, they also observed but did not identify two lines in the red part of the spectrum, a bright line in the blue part and a pale purple line. In certain experiments, the presence of two additional weak yellow lines was observed. The authors of [1]

interpreted the results of the experiment as a confirmation of their hypothesis. In modern terms their conclusion was that with the help of a high-current EEC it is possible to initiate α -decay of one or more isotopes of tungsten nuclei.

It is quite understandable that the publication [1] caused a reaction in the scientific community of the time. Rutherford expressed deep doubts that the voltage (about 30 kV) used in the experiment was sufficient to ensure that the electrons could induce nuclear reactions. To check the reliability of the published results, Rutherford used a 100 kV electron beam on a tungsten target. He directed a beam on the target and did not observe any nuclear reactions. He described this in a short message [3] in quite a harsh form. Wendt entered into scientific discussion with Rutherford, noting that the cause of discrepancies in the results could be the difference in the power input to the tungsten target [4]. The power dissipated in the wire during the capacitor discharge and the amount of current flowing through it is much greater than the one which was used by Rutherford in his electron beam. The scientific community took Rutherford's side, and the work [1] was considered erroneous and was forgotten.

In subsequent decades, dozens of research groups [5–9] studied the electric explosion of wires. To date, the generally accepted opinion in the scientific community is that in a high-temperature plasma that occurs in powerful EEC, only nuclear fusion reactions can take place (such as $D + D$); i.e. the processes that occur with the participation of strong nuclear interactions. Therefore, the focus of the EEC experimental studies has been to measure the neutron flux [10] and the soft X-ray radiation [11,12]. Scientists studied the electric explosions of tungsten wires very carefully, and because no one has ever reported the observation of the spectral lines of helium, at first glance it may seem that Rutherford was right and there is no effect. On the other hand, we have not managed to find any publication which reported the chemical composition of the gas which forms in the explosion chamber at the moment of EEC.

Even though the original hypothesis of Wendt and Irion appears deeply flawed today, considering the care with which they conducted the experiment [1] we decided to test their results using modern diagnostic methods and relying on modern theoretical concepts.

2. Modern Theoretical Concepts

First of all, it should be noted that for all five isotopes of tungsten α -decay is an energetically favorable process. Moreover, quite recently the half-life of one of the tungsten isotopes was $^{180}\text{W} : T_{1/2} = (1.8 \pm 0.2) \times 10^{18}$ years [13]. Thus, if we assume that the results of [1] are not wrong, they do not directly contradict the law of conservation of energy, but significantly contrary to the laws of probability. According to the classical theory of α -decay, the probability of α -decay is proportional to the product of the probability of α -particle formation inside the nucleus at its surface and the likelihood P_α of subsequent α -particle tunneling through a potential barrier D_α . The probability of α -particle formation, in the framework of the shell model of the nucleus, is calculated as the square of the matrix element of transition M_α from the initial kernel state into a state where four nucleons form α -particle [14]. Calculating the probability of quantum particle tunneling through a potential barrier is a classical problem of quantum mechanics. It consists of finding the distribution of the wave function of α -particle, which is the solution of the Schrodinger wave equation of quantum particle motion in the pit, the walls of which is a field of nuclear forces and the Coulomb potential.

For a long time, it was believed that the α -decay probability is determined solely by strong nuclear forces, and the form of the Coulomb potential does not affect the α -decay probability. However, in 1957, Erma published a theoretical article [15], in which he showed that the presence of electrons in the atom increases the α -decay probability compared to the α -decay probability of fully ionized atoms.

First, the field of atomic electrons reduces the barrier for α -particle; and, secondly, the charge of the nucleus decreases by two units during α -decay, resulting in a change in the energy of the electron shell. Accounting for the effects of the atomic electrons leads to the fact that in calculating the α -decay constant the energy of α -particle should be replaced by “efficient” energy, which is greater than real $E \rightarrow E + 73Z^{4/3} + 65Z^{5/3}$ eV. Because of the exponential dependence of the probability of α -decay from α -particle energy, the impact of the atomic electrons can be significant.

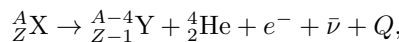
In other words, it is much easier for the quantum particle to overcome a “high”, but “narrow” barrier rather than a “low”, but “wide” one. As expected, the atomic electrons have stronger influence on the processes taking place with small energies. For example, for the ^{147}Sm (α -particle energy ~ 2.31 MeV; $T_{1/2} = 7 \times 10^{11}$ years) the presence of the electron shell increases the probability of α -decay by 2.6 times compared with the nucleus of a fully ionized atom [15].

From the results of [15] it follows that the probability of α -decay can be increased with the help of external electromagnetic influences, such as the application of a strong magnetic field. Influence of superstrong magnetic field on the probability of α -decay can be qualitatively described as follows. An external superstrong magnetic field, due to the deformation of the electron shell, changes both the spatial distribution of the electric potential and energy of the electron shell of an atom and, therefore, the energy of any nuclear decay, because the decay energy is equal to the difference of the total energies of the initial and final systems, taking into account the ionization energies of atoms or ions. The role of these factors was analyzed in more detail in [16–18].

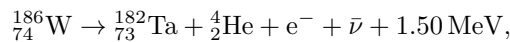
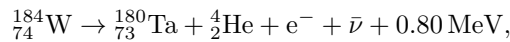
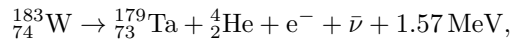
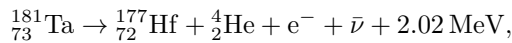
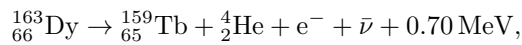
In 1970, experimental work was published [19] from which it followed that the violation of spatial parity was observed during α -decay of ^{16}N . Since the violation of spatial parity is a characteristic property of weak nuclear interactions, the results of the experiment [19] clearly indicate that α -decay phenomenon involves all three types of interactions: electromagnetic, weak and strong nuclear interactions. Since the constant of the weak nuclear interaction α_w is considerably less than the constant of electromagnetic interaction α_e , this indicates, at least in principle, the possibility of indirectly initiating of α -decay, due to the influence of electromagnetic processes on the probability of occurrence of weak nuclear processes. Possible ways of initiation of low-energy nuclear processes, taking place with the participation of the weak interactions, are discussed in detail in [16,20].

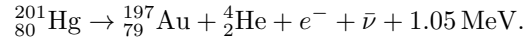
It is well known that the probability of nuclear processes that take place with the participation of leptons (k -capture, β^\pm -decay) depends on the density of the real (occupied) and virtual (free, unoccupied) lepton states of the nucleus [17,18,21]. Thus, nuclear processes can be affected by changing the density of lepton states externally (by imposing external electromagnetic fields or ionizing the electron shells of the atom). Moreover, such indirect changes in the probability of nuclear processes can reach several orders of magnitude under the influence of an external electromagnetic field [22]. In [20], the possibility of participation of virtual (free, unoccupied) electron states in the process of α -decay of heavy nuclei was discussed. In this case, a significant indirect increase in the probability of decay in superstrong electromagnetic fields is also possible due to changes in the density of these unoccupied electron states at the core.

Another, hypothetical decay channel, leading to the induced decay of heavy nuclei, is an energetically favorable process of α -decay that occurs simultaneously with β -decay (“ $\alpha\beta$ -decay”).



where X and Y – a nuclei with atomic weight A and (A – 4) and charges Z and (Z – 1), respectively, $\bar{\nu}$ – antineutrino, Q – the released energy. For example:



**Table 1.** Isotopes for which $\alpha\beta$ -decay is energetically favorable.

Initial nu- cleus			Product of $\alpha\beta$ -decay			Energy of $\alpha\beta$ -decay (keV)	Energy of α -decay (keV)	Energy of β -decay (keV)
Name	Z	A	Name	Z	A			
La	57	138	Ba	56	134	0.59	−2057	1045
Nd	60	145	Pr	59	141	2159	1578	−164
Nd	60	146	Pr	59	142	437	1182	−1470
Nd	60	148	Pr	59	144	917	597	−540
Nd	60	150	Pr	59	146	651	−415	−87
Pm	61	145	Nd	60	141	499	2321	−615
Sm	62	147	Pm	61	143	1269	2311	−1720
Sm	62	149	Pm	61	145	1707	1870	−691
Eu	63	151	Sm	62	147	2189	1963	−463
Eu	63	153	Sm	62	149	1345	272	−485
Gd	64	155	Eu	63	151	158	79	−822
Gd	64	157	Eu	63	153	118	−689	−59
Tb	65	159	Gd	64	155	113	−140	−366
Dy	66	161	Tb	65	157	284	343	−859
Dy	66	163	Tb	65	159	727	−242	−1.42
Ho	67	165	Dy	66	161	733	138	−376
Er	68	167	Ho	67	163	663	666	−747
Er	68	170	Ho	67	166	537	51	−313
Tm	69	169	Er	68	165	824	1201	−908
Yb	70	171	Tm	69	167	811	1557	−1479
Yb	70	173	Tm	69	169	1297	946	−671
Yb	70	174	Tm	69	170	426	738	−1357
Yb	70	176	Tm	69	172	1462	571	−105
Lu	71	175	Yb	70	171	1716	1619	−685
Lu	71	176	Yb	70	172	3448	1568	1192
Hf	72	177	Lu	71	173	1574	2245	−1166
Hf	72	178	Lu	71	174	709	2084	−1912
Hf	72	179	Lu	71	175	2276	1807	−109
Hf	72	180	Lu	71	176	1177	1281	−854

Table 1 continued

Ta	73	180	Hf	72	176	3224	2029	708
Ta	73	181	Hf	72	177	2024	1524	–188
W	74	183	Ta	73	179	1571	1682	–556
W	74	184	Ta	73	180	804	1657	–1483
W	74	186	Ta	73	182	1496	1123	–580
Re	75	185	W	74	181	2007	2195	–1013
Os	76	187	Re	75	183	2165	2720	–1501
Os	76	188	Re	75	184	660	2143	–2808
Os	76	189	Re	75	185	2409	1974	–533
Os	76	190	Re	75	186	797	1377	–2000
Os	76	192	Re	75	188	711	362	–1045
Ir	77	191	Os	76	187	2086	2084	–1019
Ir	77	193	Os	76	189	2027	1016	–55
Pt	78	195	Ir	77	191	1472	1158	–225
Pt	78	198	Ir	77	194	184	87	–324
Au	79	197	Pt	78	193	898	953	–600
Hg	80	199	Au	79	195	598	823	–1445
Hg	80	201	Au	79	197	1053	333	–483
Hg	80	204	Au	79	200	148	–512	–346
Tl	81	203	Hg	80	199	1363	909	–974
Tl	81	205	Hg	80	201	1419	143	–51
Pb	82	207	Tl	81	203	883	390	–2399
Pb	82	208	Tl	81	204	171	519	–2879
Bi	83	209	Pb	82	205	3086	3138	–1893
Th	90	232	Ac	89	228	4129	4082	–495
U	92	234	Pa	91	230	3549	4858	–1809
U	92	235	Pa	91	231	5068	4678	–123
U	92	238	Pa	91	234	4543	4269	–145

For such types of decays, as well as for classical β -decays, one can expect a significant increase in the probability of decay when an atom is exposed to an external superstrong magnetic field. However, even if individually α - and β -decays (e.g., for the core) are energetically forbidden, the simultaneous “ $\alpha\beta$ -decay” can be an energetically favorable process. The essential difference of the process from the classical α -decay is as follows: in $\alpha\beta$ -decay total energy (i.e. mass sum and kinetic energy) of the final nucleus ${}_{Z-1}^{A-4}Y$ and the α -particle is always smaller than the mass of the compound nucleus ${}_{Z+1}^A\tilde{X}$. For example, for the first decay the sum of energies of α -particle and the ${}_{65}^{159}\text{Tb}$ is less than the mass of ${}_{67}^{163}\text{Ho}$ nucleus. It obviously follows from the fact that the original nucleus is β -stable. That is, an artificial combination of α -particle and the ${}_{65}^{159}\text{Tb}$ nucleus cannot give a real ${}_{67}^{163}\text{Ho}$ nucleus – obtained nucleus can only be “virtual”, with energy lesser than the energy of the ground state for ${}_{67}^{163}\text{Ho}$ nucleus.

All stable isotopes, for which $\alpha\beta$ -decay is energetically favorable, are shown in Table 1. The table shows: the decaying isotope, decay product and energy of $\alpha\beta$ -decay. The sign “–” in the line of energy means that process is energetically unfavorable, and hence its absolute prohibition.

Although the probability of such a process is very low in normal conditions, a superstrong magnetic field may be

a good “catalyst.” Since, in a superstrong magnetic field, the phase volume of bound states of electrons, in which the β -decay can occur, significantly increases [22]. The magnetic field “pulls out” the electron, which, for these isotopes, can be born only with the departure of an α -particle: i.e. a “torn out” α -particle provides the necessary energy. The development of $\alpha\beta$ -decay theory and calculation of the process probability is similar to the calculation of the probability of forbidden β -decays [22], but the nuclear function of the final state should include the birth of an α -particle. Note that, for β -decay of nucleus in a superstrong magnetic field, the electron will be born in a bound state.

As mentioned above, the $\alpha\beta$ -decay process is fundamentally different from the classical α -decay in that it occurs through the formation of an intermediate nucleus, the energy of which is less than the energy of the ground state of the nucleus ${}^A_{Z+1}\tilde{X}$. Since the intermediate nucleus formed from an α -particle and final nucleus ${}^{A-4}_{Z-1}Y$ is virtual, the wave functions of the α -particles produced during the $\alpha\beta$ -decay and during classical α -decay differ greatly. In case of classical α -decay the wave function of α -particle describes the virtual particle in the potential barrier, but a real one both outside and inside the nucleus. In the test problem of the wave function of $\alpha\beta$ -decay the energy of α -particle inside the nucleus should be less than the potential energy inside a nucleus. That is, in contrast to the classical α -decay the wave function Ψ of α -particle will describe a real particle outside of the nucleus, but virtual, both inside the barrier and in the nucleus inner region. Thus, α -particle is created virtual [20].

Since, similar to the classical β -decay, the lepton (electron and neutrino) wave functions do not change significantly at the distances of the order of size of the nucleus, the lepton factor can be taken outside the integral of the nuclear matrix element. Integrands of nuclear matrix elements that depend on the spatial coordinates can always be represented as an expansion in orthonormal spherical functions. In this case (as in the case of classic β -decay [22]), when the square of the matrix element is calculated, the nuclear part of the matrix element can be taken out outside the summation sign of the lepton states, and the square of each element of the matrix will be equal to:

$$|M_i|^2 = |M_{Ni}|^2 f_s(ZQ),$$

Where M_{Ni} is the corresponding first non-zero moment of the nuclear part of the matrix element, f_s is the Fermi integral function, which determines the phase volume of the final lepton states, Q is the energy of the nuclear transition. An “explosive” increase in the lepton phase volume f occurs, when an external superstrong (on the atomic scale) magnetic field is applied to an atom, due to the increase in the density of free states of electrons of the discrete spectrum. It can be assumed that these magnetic fields are small compared to “nuclear” level, and the nuclear part of the matrix elements remain practically unchanged. In [22] electron wave functions are calculated in cylindrical coordinates in an external static uniform superstrong magnetic field and in the central electric field of the nucleus, and the spectrum of bound states of electrons is shown. The sum of the lepton phase volume (i.e. the density of electron states in the area of the nucleus) over all electronic states of the discrete spectrum is proportional to $\Sigma_\chi (B_\chi/\chi)$, where χ is the quantum number of the longitudinal state (along the magnetic field) in which the electron is born and B_χ -coefficients which are determined by the form of the solution of the electron equation in the central electric and static uniform magnetic fields (where the exact solution is given in [22]). The reason why the electron density is inversely proportional to the degree of longitudinal quantum number in a superstrong magnetic field lies in the fact that influence of a superstrong magnetic field on the atom reduces spherical symmetry to the one-dimensional Coulomb problem. In the superstrong magnetic field electron orbit transformed into the cylinders stretched along the magnetic field with a transverse dimension equal to the Larmor radius and a longitudinal dimension equal to the Bohr radius (which is proportional to the quantum number χ of longitudinal motion). Formally, this sum diverges at large χ (B_χ factors are limited from below), it shows that the excited states of longitudinal motion provide the main contribution to the β -decay probability.

For the allowed and the unique-forbidden $\alpha\beta$ -decay, among matrix elements only one is dominant and, in these cases, it is obvious that the probability of decay is proportional to the square of this matrix element. Thus, the proba-

bility of decay is proportional to the Fermi function f , which, in turn, in superstrong magnetic field, is proportional to the phase volume of bound states of electrons and neutrinos. Since the phase volume of the neutrino is proportional to the square of the neutrino energy, then for the decay to a bound state of the electron, the probability of such decay is proportional to the square of the energy Q released during the nuclear reaction [22]:

$$\lambda_{\alpha\beta} \propto Q^2 \sum_{\chi} \left(\frac{B_{\chi}}{\chi} \right).$$

For the forbidden (non-unique) decays among matrix elements there are those that will have close values, and the probability of decay will be calculated in a more complicated way. But, in any case, you can always use this expression for a rough estimation.

Thus, we can see that in a superstrong magnetic field, the Larmor radius of the electron becomes small compared to the Bohr radius, and the phase volume of unoccupied lepton states increases infinitely, i.e. the so-called “burst phase volume” is observed [22]. This leads to an increase in the number of final states of the system, in which the decay may occur, which, in turn, leads to an increase in the probability of nuclear decays with the birth of an electron. Energetically favorable nuclear processes, in which α -decay occurs at the same time with β -decay to a bound state (“ $\alpha\beta$ -decay”), can acquire a finite probability in a superstrong magnetic field due to “an explosion of lepton phase volume.”

As seen from the above, our understanding of nuclear physics have changed considerably over the past 90 years, and today, Rutherford’s point of view no longer appears to be as inviolable as before. Of course, the above arguments in favor of the possibility of initiating α decay via influence of a superstrong magnetic field on the heavy atoms are purely theoretical and the probability of such processes are very small, but it is important that their implementation is not forbidden by the conservation laws. The possibility of initiating nuclear processes that occur with the participation of weak nuclear interactions, with the help EEC, has not yet been investigated experimentally.

3. Experimental Section

Experiments on electric explosion of a tungsten wire were conducted in 2010–2011 at the Sukhumi Institute of Physics and Technology (The Republic of Abkhazia) with the “HELIOS” experimental setup.

3.1. Description of the experimental setup and procedure for conducting experiments

The electrical part of the setup consists of four IMN 100-0.1 capacitors with capacitance $C = 0.1 \mu\text{F}$ and an inductance of 150 nH connected in parallel. To reduce the total inductance, the bus of capacitors is made of sheet copper 1 mm thick. Charging was performed by an AII-70 power supply unit through a rectifier and a charging resistor to the voltage $U = 35\text{--}40 \text{ kV}$.

The capacitor bank was closed using a three-electrode low-inductance controlled air discharger. The discharger was connected to the explosion chamber by eight parallel radiofrequency cables ($\rho = 50 \Omega$, $L = 200 \text{ nH/m}$) two meters long each.

A schematic diagram of the vacuum system of the setup is shown in Fig. 1. Vacuum pumping of the chamber (6) was carried out with an oil-free spiral vacuum pump Varian SH-110 (1) and a turbo-molecular pump 01AB-450-003 (14) (with the limit of $4 \times 10^{-5} \text{ Pa}$) up to the pressure $\sim 10^{-4} \text{ Pa}$.

The explosion chamber (6) was attached to the vacuum gate (10) via an intermediate flange 25 mm height and 120 mm in diameter (9) which has a center hole for vacuum pumping. At the same time, the flange (9) served as the place connecting to the FRG700 pressure sensor and devices for the study of the gas mixture resulting after the EEC. The joint for the leak valve (7) was located in the upper flange of the explosion chamber coupler. The leak valve

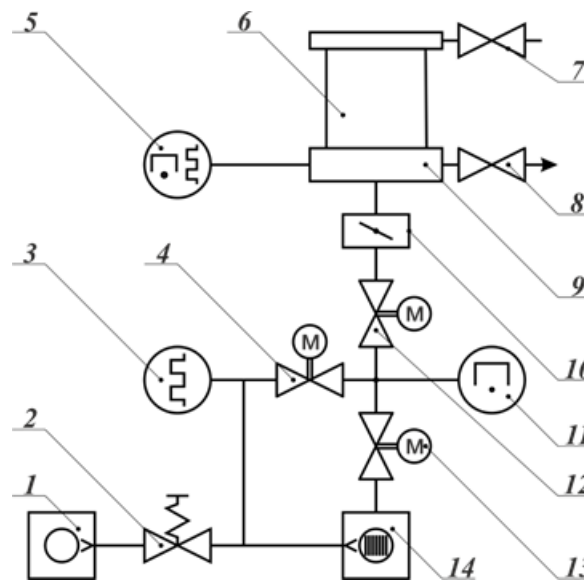


Figure 1. Diagram of the vacuum system. 1 – backing pump Varian SH-110; 2 – off valve; 3 – manometer gauge Pirani PMT-6; 4, 12, 13 solenoid valves type KEUN-40; 5 – combined full-range vacuum sensor Varian FRG700; 6 – blast chamber; 7 – manual “fine” leak valve; 8 – valves for connection of gas diagnostics; 9 – intermediate flange; 10 – manual gate valve type Varian VGA0631M; 11 – manometric sensor PMM-32; 14 – turbo molecular pump TMP 01AB-450-003.

(7) served as the inlet for air, calibration gas mixtures or “service” gas required for cleaning the inner surface of the chamber.

In the experiments described here, two types of explosion chambers were used: drawn quartz tube (inner diameter 55 mm, height 110 mm, wall thickness of 2–3 mm) and a stainless steel cylinder ($^{12}\text{Cr}^{18}\text{Ni}^{10}\text{Ti}$, internal diameter 55 mm, height 110 mm, wall thickness 2.5 mm). The volume of explosion chamber itself was $V_{\text{chamber}} \approx 250 \text{ cm}^3$ and the total volume to the place of the gate setup, including all the technological appendages, $V_{\text{sum}} = 397 \pm 4 \text{ cm}^3$. The value of the total volume V_{sum} is very important for a correct measurement of the absolute number of particles with $m = 4$. The following procedure was used to precisely measure the total volume. A pre-evacuated calibration tank, with the precisely measured volume V_{cal} , was joined to the closed valve 5 (Fig. 2). Then, with gate 10 closed and valve 5 opened, the chamber was filled with gas, the pressure of which was controlled by a digital gauge. After that, the valve on the calibration tank was opened and the pressure equalized in both volumes V_{sum} and V_{cal} . After closing the gate 5, calibration tank was disconnected and evacuated, and then the procedure was repeated several times. By controlling the amount of pressure on each step of the procedure, and assuming that temperature is constant, it is quite simple to calculate V_{sum} , and multiple repetition of procedure reduces the measurement error.

Figure 2a shows a schematic of explosion chamber, and Fig. 2b shows a photo of it. Contact between the electrodes (1) and the wire (4) was provided by a collet seal. In experiments electrodes made of tungsten and stainless steel were used. Using the latter promoted reduction of electron emission from the electrode surface, which improved the reproducibility of the results. Tungsten wires (4) of different cross sections (10, 50, 70, 130 and $200 \mu\text{m}$) and length ranging from 24 to 40 mm were used in these experiments. In test experiments iron (Fe) wires of the same dimensions were exploded.

In order to reduce the amount of gas adsorbed by the walls of the explosion chamber, before the electric explosion,

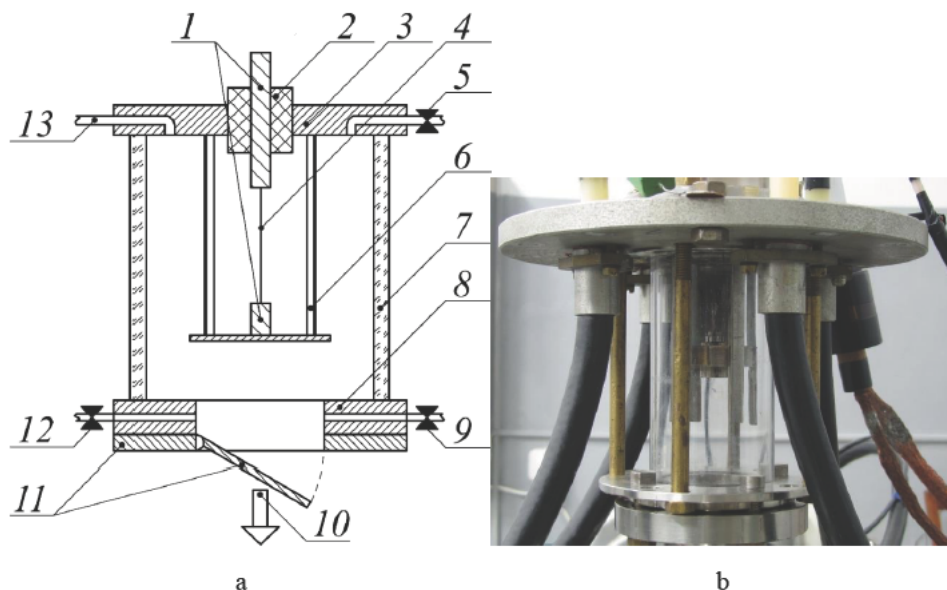
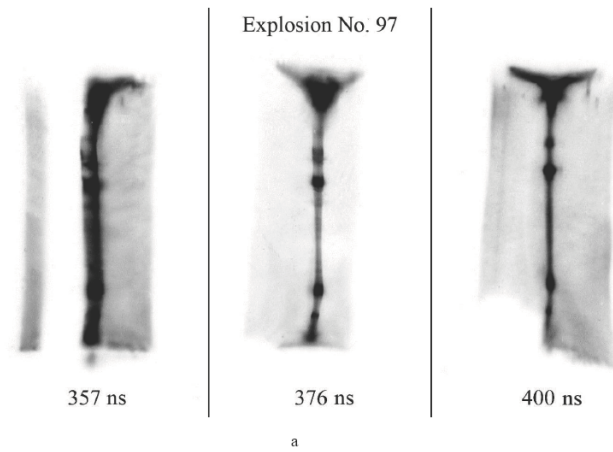


Figure 2. Blast chamber: (a) 1 – mounting electrodes; 2 – insulator; 3 – top flange; 4 – wire; 5 – leak valve for the inlet of argon; 6 – current-return pathway; 7 – chamber wall; 8 – lower flange; 9 – valve for MS-200; 10 vacuum pumping; 11 – gate; 12 – MS-40 valves; 13 – hole for pressure lamp connection. (b) photo of the quartz blast chamber.

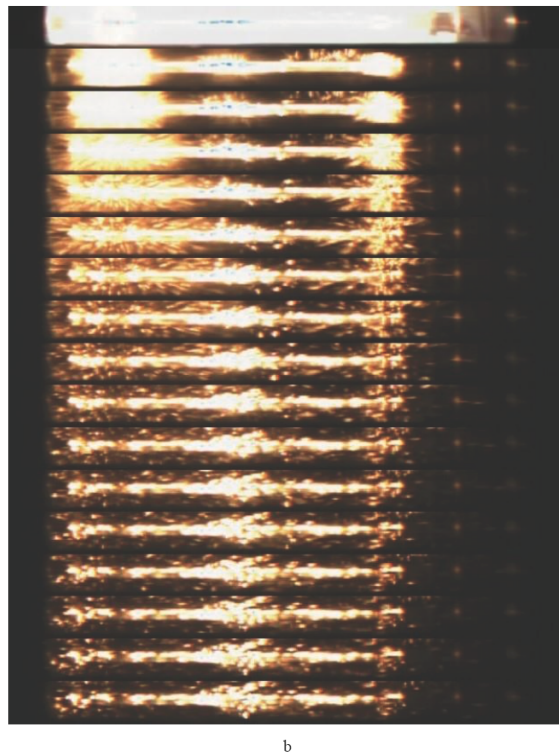
the chamber was filled with argon and it was ignited with the high-frequency glow discharge. Then chamber was pumped out to the required pressure using a vacuum pump. In order to degas the tungsten wire before the EEC it was heated by the current of 0.2–2 A (depending on wire diameter) to the temperature ~ 1500 K for 0.5–2 h. The source for wire heating was inductively decoupled from the setup, which allows us to trigger the electric explosion without turning off the heating (hereinafter referred to as a “hot start”). The electric explosion of a tungsten wire was produced in the explosion chamber, which was cut off from the vacuum system immediately before the electric pulse. This technique allowed us to investigate the gas produced by EEC of tungsten wire. Preparations for the electric explosion were carried out in the following order:

- (1) Setting the wire in the load node (coaxial assembly).
- (2) Setting the load node in explosion chamber.
- (3) Cleaning the chamber using glowing discharge in argon.
- (4) Vacuum pumping of the chamber up to the pressure about $1 - 2 \times 10^{-5}$ Pa.
- (5) Degassing the wire by heating it.
- (6) Slowly turning off wire heating.
- (7) Cutting off vacuum chamber from pumping system.
- (8) Conducting electric explosion.
- (9) Analysis of the resulting gas medium.

The time interval t between entries 7 and 8 was $t \leq 10$ s.



(a) Typical IIT photo



(b) Set of frames from high-speed camera

Figure 3. Photorecording diagnostics: (a) Typical IIT photo. (b) Set of frames from high-speed camera.

3.2. Main diagnostic method

All diagnostic methods that were used in the experiment can be divided into four groups: electrical, photorecording, optical and gas diagnostics.

3.2.1. Electrical diagnostics

Electrical diagnostics were used to monitor the parameters of electric explosion. The sensors that were used included: a voltage divider, Rogowski coil and current loops. That is quite a common set of sensors which are always used in experiments of this type.

3.2.2. Photorecording diagnostics

Equipment used as photorecording diagnostics included: a high-speed video camera with a frame rate up to 10 kHz and a three-frame electron-optical system (three image intensifier tubes, IIT) which was photographing with an exposure time $\tau \sim 15$ ns. The time delay between shots can be changed.

The high-speed video camera allowed us to control the dynamics of the explosion as a whole and three-frame IIT system provided control of emission uniformity along the length. A typical IIT photo sequence is presented in Fig. 3a. Figure 3b presents a set of frames from the high-speed video camera obtained in one of the experiments. Figure 3a shows the inhomogeneity of emission along the length of the wire and the emergence of the so-called “hot spots”.

Figure 3b shows that complete destruction of the wire core takes place only by the end of the second millisecond. The fact that the wire core exists much longer than the current pulse duration was known long ago, but the application of high-speed video camera allowed us to clearly verify this. Using this same technique, it was possible to judge the degree of dispersion of tungsten powder formed during the destruction of the wire core. The degree of dispersion increases with decreasing the diameter of the exploded wire. Comparison of frames from the photorecording diagnostics with current waveforms showed that, under the same experimental conditions, the current and voltage waveforms vary little from experiment to experiment, but the visual dynamics of the EEC may undergo significant changes.

3.2.3. Optical diagnostic

The main objective of the optical diagnostics was to obtain information on parameters and the chemical composition of the plasma formed as a result of EEC [23]. The time behavior of the integral (over the wavelength) light intensity was measured using an FD-263-01 silicon photodiode with amplifier. The signal from this device was sent to a Tektronix TDS-2024B digital oscilloscope. It should be noted that the data obtained by a photodiode served as a more reliable marker of reproducibility of experiments than the current–voltage characteristics of the electric explosion.

To determine the chemical composition of the plasma at the time of the electric explosion by spectral characteristics of light radiation two types of optical spectrometers were used. The spectrometers differ in spectral resolution.

An Abbe prism is used in one of them (UM-2) as a dispersing element, which does not allow high spectral resolution, but provides sufficient optical efficiency. Its other advantage is the fact that the entire visible spectral region fits into a length of ~ 30 mm. This size corresponds to the diameter of the image intensifier photocathode, allowing the use of an electron-optical converter (IIT) as a light amplifier. To register the intensified spectrum, we used a high-sensitivity film that was pressed against IIT fiberglass exit port or CCD array, connected by a fiberglass washer with the tube output window. Due to its high sensitivity, this spectrometer allowed us to obtain an overview spectrum of optical radiation at every electric explosion of tungsten wire.

In the other type of optical spectrometer (STE-1), a diffraction grating is used as a dispersing element. This allowed us to record the spectrum at high resolution. However, the STE-1 sensitivity was significantly worse than that of the

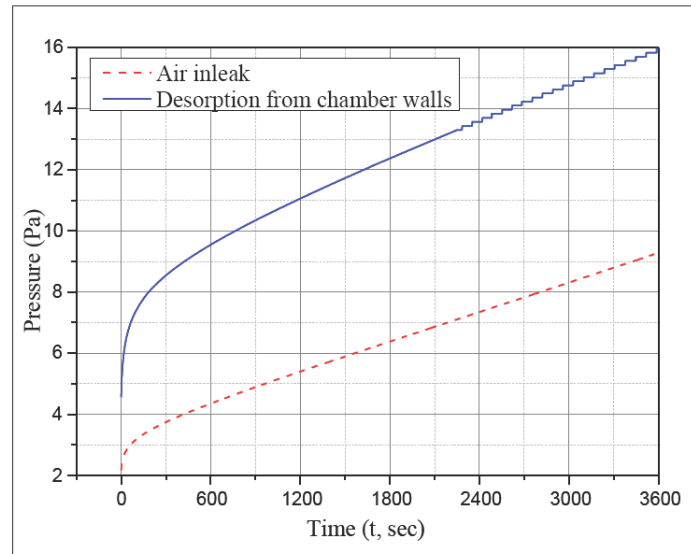


Figure 4. The time dependence of pressure in the chamber after the gate closing.

prism spectrometer; therefore, it was possible to measure spectra only at large light fluxes. With this instrument, we also used a CCD array as a photo-recording element and so the measured spectral range was limited by the geometrical size of the CCD array (29 mm).

3.2.4. Gas diagnostic

The specifics of the task required the study of the gas phase formed after the electric explosion. The main objectives of these methods was to identify helium atoms by weight, and to measure their quantity. As far as we know from the literature, the study of the chemical composition of the gas formed in the explosion chamber after the electric explosion of wires has never been carried out.

Registration of pressure in the explosion chamber was carried out with the help of inverted magnetron gauge VARIAN FRG-700 with an operating range 10^{-5} – 10^5 Pa. The data from the gauge was transferred to a computer, allowing us to continuously monitor the pressure changes in the setup and, therefore, evaluate gas leakage rate into the chamber with 5% accuracy in on-line mode, both before and after the electric explosion. The technique of continuous measurement of pressure played an important role in the process of preparation for the experiment (viz: wire heating, cleaning of the explosion chamber surface with glow discharge in argon, leakage elimination).

When the explosion chamber was cut off from the vacuum pumping system, the pressure increase rate in the chamber is determined by the diffusive flux from the chamber walls and inleakage of air due to imperfect sealing. However, since the diffusive flux associated with the desorption is defined as $Q_d \sim \sqrt{t}$, and the flux associated with atmospheric inleakage is $Q_{at} \sim t$ (where t is the time), therefore based on the type of curve of leakage speed time dependence, it can be determined which process is dominant at a given pressure. The typical form of pressure increase time dependence after gate closing is shown in Fig. 4. If from the type of pressure increase curve it followed that diffusive flux was decisive, this was an indication for further purification of quartz chamber surface with glow discharge. If the pressure increases linearly with time, that means the determining factor is leakage from the atmosphere, and the

sealing of vacuum chamber need to be improved. Usually the level of leakage was

$$\frac{dp}{dt} \approx 1 \text{ to } 5 \text{ Pa/h},$$

which made it possible to conduct EEC at a pressure $P_0 < 10^{-3}$ Pa (including the closing time of the gate).

A compact TOF mass spectrometer (MC-200) was used for a qualitative analysis of the chemical composition of the gas formed in the explosion chamber. This was connected to valve 12 (Fig. 2). This device has resolution $R \sim 200$ in investigated mass range, allowing us to confidently identify all the mass in the range of $M = 2$ to 500. In order to resolve light mass doublets (D_2 and ^4He , HD and ^3He) it was necessary to use a special device with high sensitivity and resolution $R \sim 900$ in light mass region.

A helium leak detector (MS-40 DryCE; hereinafter MS-40) was used to measure the amount of gas particles with $m = 4$ a.m.u. (hereinafter $m = 4$). It was connected to the chamber via valve 9 (Fig. 2) using a short stainless steel pipe. Two parallel-connected shut-off valves, which had different throughput capacity, were mounted between the explosion chamber and pipe. Gas formed after electric explosion was pumped out first through the valve having a small hole, and further, with decreasing of pressure in the chamber, through the second valve with a larger hole. This procedure allows us to stay within the linear counting mode of the MS-40 device and correctly measure of the gas flux with $m = 4$ during the entire gas evacuation process, regardless of the initial pressure in the explosion chamber.

The MS-40 sent data to a computer, where it was processed using specially written software. The sensitivity of the device allows us to confidently detect the atmospheric helium and carry out quantitative measurements of particles with $m = 4$ starting from the flow rate $\sim 10^{10}$ at. $\text{cm}^3 \text{ s}^{-1}$. Periodically (every 10 measurements), the MS-40 is automatically calibrated according to value of the helium flow in the built-in calibration leak (flow $\sim 3 \times 10^{-8}$ bar $\text{cm}^3 \text{ s}^{-1}$).

The following procedure was developed to calibrate the method of measuring particles $m = 4$ using the MS-40. In the explosion chamber, previously evacuated to pressure 10^{-4} Pa, a known amount of air was let in and then pumped through the leak detector, counting the number of ^4He atoms. Since ^4He concentration in the atmosphere and

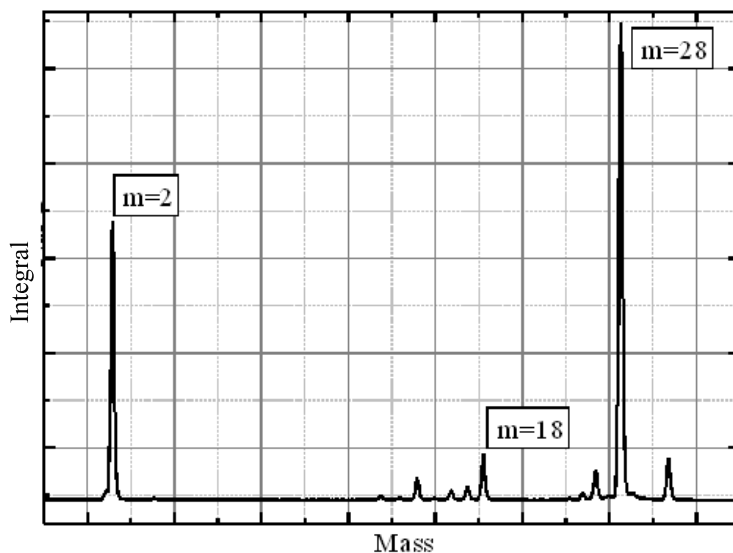


Figure 5. Mass spectrum of gas produced as a result of EEC.

the amount of V_{sum} of the chamber are known, it is possible to relate the experimentally measured quantity of ^4He particles to theoretically calculated value for a given volume of the chamber. To account for the nonlinearity of the MS-40 ionization unit and detector, the calibration was carried out at all pressure ranges (10, 20, 50, 67 Pa, and so on), which were observed in the explosion chamber after EEC. To calibrate the MS-40 for the study of gas mixtures with ^4He concentration higher than in the atmosphere ($\gamma = 5 \times 10^{-6}$) calibration gas mixtures with a known concentration of ^4He were created. A special stand was designed to create such calibration mixtures. These efforts have allowed to use the MS-40 device as a measurement tool.

Due to its low mass resolution, the leak detector cannot distinguish D_2 molecule from ^4He atom, which creates uncertainty in the results obtained. Spectral optical methods were designed to eliminate this uncertainty.

There were attempts to detect fast neutrons. Neutron search methodology was based on the registration of the recoil protons. An organic scintillator detector (diameter 40 mm and length 60 mm) combined with PMT was used for that purpose. However, no signals indicating the birth of neutrons at the moment electric explosion had been recorded during the experiments.

3.3. Experimental results

3.3.1. Gas diagnostic

Pressure of about $P_1 \sim 50$ Pa was observed in the chamber after EEC, which correlates well with the results of [1]. Chemical analysis of the gas, resulting from the electric explosion, conducted using an MS-200 mass spectrometer [24] showed that the gas consists of about 40% hydrogen and the remaining 60% is a gas mixture that is similar in chemical composition to air. As can be seen from the typical gas mass spectrum shown in Fig. 5, the peaks $m = 2$ a.m.u. (hydrogen molecule H_2) and $m = 28$ a.m.u. (molecules of nitrogen N_2 or carbon monoxide CO) are prevalent in the spectrum. However, considering the fact that the peak of $m = 14$ a.m.u. (nitrogen atom N) and the peak of $m = 32$ a.m.u. (oxygen molecule O_2) are relatively small, we can confidently say that the peak of $m = 28$ a.m.u. is a gas mixture of nitrogen and carbon monoxide. Peaks of water and its “fragments” (H_2O , OH , O), which are always present in any mass spectrometry equipment, are also visible in the spectrum. This is due to the fact that water molecules are adsorbed by the surface very easily.

The pressure surge and chemical composition of the gas depend weakly on the wire parameters (its radius and length). This means that the major contribution to the gas phase EEC was conditioned by degassing of the chamber walls and other structural elements. One way to reduce the amount of degassed particles is to increase the damping coefficient of the discharge circuit. A non-linear resistance (depending on temperature) was mounted between the cables, which conveying the pulse from the battery to the load, and the wire to achieve an aperiodic current pulse. Figure 6 shows current waveforms of experiments with different modes: oscillating current (Run No. 147) and almost aperiodic current pulse (Run No. 109). With the same dimensions of the W wire, in experiments with low Q -value of the circuit, gas pressure after EEC averaged over a series of five experiments, was $PL = 22 \pm 2$ Pa and in experiments with a high Q -value of the circuit pressure was $PH = 61 \pm 5$ Pa. Comparing obtained pressure values with current waveforms we can conclude that more than half of the total gas is produced after the passage of the first half period of the current, i.e., by oscillating discharge.

The peak in the area of $m = 3$ a.m.u. is barely noticeable in the mass spectrum presented in Fig. 5. Figure 7 shows a magnified fragment of mass spectrum where a peak with $m = 3$ a.m.u. is clearly visible. Due to the fact that the MS-200 mass-spectrometer does not have sufficient resolution, the $m = 3$ peak may be interpreted as: HD molecule, the hydrogen ion, hydrogen isotope ^3H and helium isotope ^3He . The presence of tritium ^3H in the experiment seems unlikely, as there no significant level of radioactivity was detected. It is also difficult to attribute peak $m = 3$ to hydrogen ions because such ions lifetime very small compared to the measurement time. The possibility of formation of such ion in the mass spectrometer ionizer is negligible [25]. Thus, the peak of $m = 3$ a.m.u. in the spectrum can

be associated with the appearance of either HD molecules, or with ^3He atoms. It should be noted that MS-40 has an option for measuring the number of particles with $m = 3$, but our inability to carry out the calibration, due to the lack of ^3He calibration source, did not allow us to use the MS-40 function to count the number of particles with $m = 3$.

The sources of hydrogen could be: water that remained on the metal surfaces; Viton gaskets used for sealing or hydrogen, which did not completely diffused during the heating of tungsten wire. Based on the research we performed it is difficult to clearly indicate the origin of such a large amount of hydrogen. But since there is a noticeable amount of water fragments in the mass spectrum, it can be argued that a significant portion of hydrogen owes its origin to the water remained on the chamber walls. The ratio between normal water H_2O and semi-heavy water DHO is about 3500: 1. Approximately the same ratio is valid for the H_2 and HD gases, therefore the same ratio between the peak amplitudes of the second and third mass peaks should be expected in gas mass spectrum. However, the ratio between these peaks, in the experiments, was in the range of 30–200:1.

The MS-200 mass-spectrometer is able to record the time dependence of values of the ion currents for selected masses. The time dependence of peaks $m = 2$ and $m = 3$ is shown in Fig. 8. Assuming that the presence of peak $m = 3$ is associated with the molecules of HD, time dependence of peaks $m = 2$ and $m = 3$ should correlate, since both peaks are caused by the presence of hydrogen in the measured gas mixture. As it can be seen from Fig. 8 $m = 3$ peak quickly disappears and the time trend of peaks $m = 2$ and $m = 3$ does not correspond to our assumption. Thus, the experimental data indicates that the appearance of a peak with $m = 3$ a.m.u. can be associated with the formation of ^3He . Since the optical spectra of ^3He and ^4He are very similar, such a conclusion does not contradict the results of [1], but it is significantly contrary to theoretical considerations expressed in our article.

The method of continuous measurement of total pressure was very helpful during the counting the number of $m = 4$ particles contained in the explosion chamber with the help of MS-40 leak detector, as it allowed, with good accuracy, to consider the number of ^4He leaked into the explosive chamber from the air in the atmosphere.

The procedure for measuring the number of $m = 4$ particles was as follows. After the electric explosion all the gas located in the explosion chamber was pumped through a helium leak detector, which allow us to calculate the total

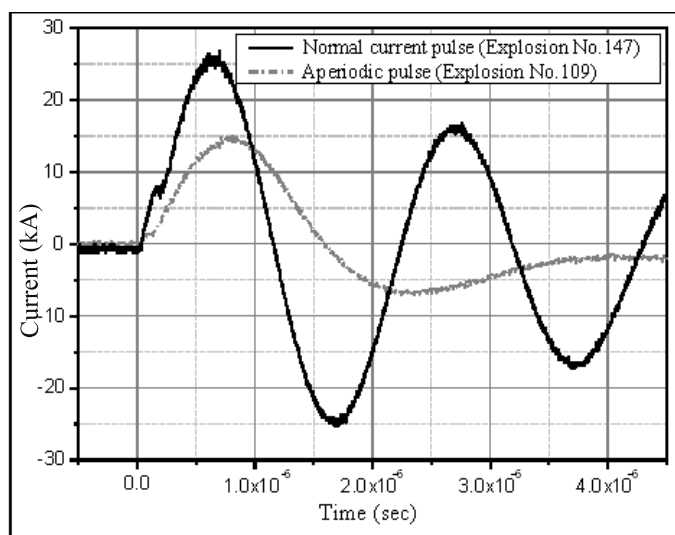


Figure 6. Current pulse waveforms for different damping coefficients.

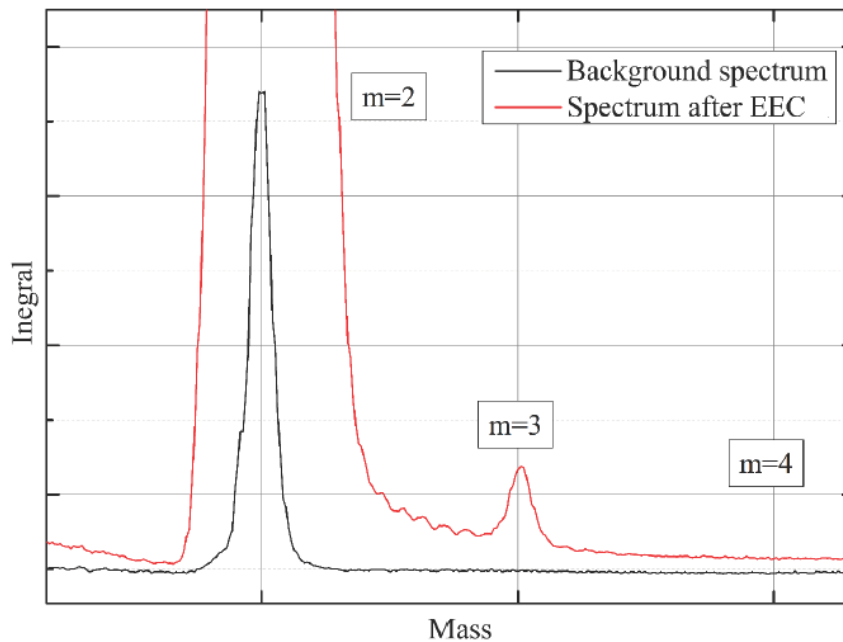


Figure 7. Mass spectrum fragment in the area of light masses.

number of $m = 4$ particles. Then, the valve connecting the explosion chamber with the leak detector was closed, and for several hours the pressure in the chamber grew, due to the diffusion of gas from chamber walls and leakage of air through the seals. Then the procedure of pumping gas through leak detector was repeated. The measurement results are shown on the graph (Fig. 9).

The figure shows that the rate of $m = 4$ particle formation after the electric explosion of tungsten wire decreases with time, and after the time $T \sim 70$ h it becomes constant. A possible explanation of the time dependence of the concentration of particles with $m = 4$ is that ^4He atoms, formed during EEC, have high energy and are “hammered” into the surface of the quartz cylinder to a certain depth and then slowly diffuse out of the quartz chamber walls. It should be noted that helium has an abnormally high diffusion coefficient in quartz [26]. It can be seen from the curve form shown in Fig. 9 that after 70 h a leakage of helium from the atmosphere through the connecting seals becomes the primary mechanism which determines the formation of helium in the explosion chamber.

In order to ensure that the $m = 4$ particles detected after the electric explosion are indeed ^4He atoms and their formation is due to the electric explosion of tungsten wire, a series of test experiments was carried out in which iron wire was used as a load. Iron wire was chosen because the α -decay of iron isotopes is energetically forbidden, unlike tungsten isotopes. If the accumulation effect of $m = 4$ particles was associated only with external factors, then the time dependence of the particle accumulation rate after the electric explosion of iron wire would not have been different from the curve shown in Fig. 9. However, in experiments with iron, the wire leakage rate was constant and determined completely by the gas leakage from atmosphere. The number of $m = 4$ particles, measured within 2 h after the EEC of iron wire, was $(6.2 \pm 0.9) \times 10^{11}$ U/Pa, which corresponds to the natural concentration of helium in the atmosphere $(5.2 \pm 0.2) \times 10^{11}$ U/Pa. Whereas $m = 4$ particle concentration for the EEC of tungsten wire reached 6×10^{12} U/Pa or higher. Thus, our verification experiments with iron wire allow us to reach a preliminary conclusion that a portion

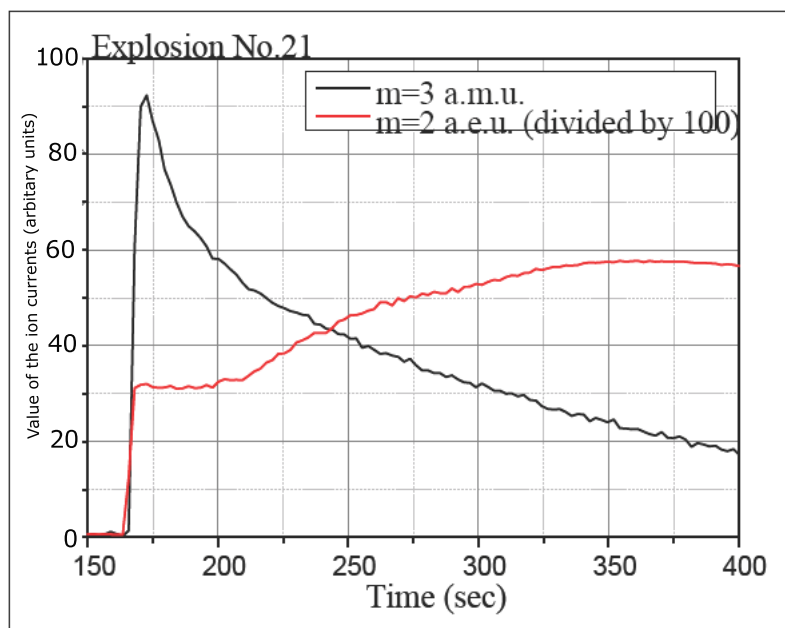


Figure 8. The time dependence of peaks $m = 2$ a.m.u. and $m = 3$ a.m.u.

of particles with $m = 4$ a.m.u. measured after EEC are connected with electric explosion of tungsten wire.

Attempts were made to establish the dependence of the measured amount of particles $m = 4$ with the length and diameter of the tungsten wire. However, because of the little excess of $m = 4$ particles over the background and lack of reproducibility of the experiments, statistically significant ($\sigma \geq 3$) results were not achieved.

3.3.2. The results of measurements of optical methods

The high sensitivity of the method, that combines prism optical monochromator UM-2 and image intensifier tube, allows us to obtain a panoramic spectrum of the visible range for each electric explosion of tungsten wire in vacuum.

Figure 10 shows the panoramic optical spectrum of light registered in the moment of electric explosion of tungsten wires of different diameters (10, 70 and 200 μm). The analyzed spectrum of optical radiation is located in the central area of each figure. The calibration spectra of mercury–helium and hydrogen lamps are located in the lower and upper areas. With its help the identification of the individual lines of the investigated range was made. The brightest lines in the examined spectrum were: $H\alpha$ line of atomic hydrogen ($\lambda_{H\alpha} = 6563 \text{ \AA}$), and two lines in the red region, which could not be identified with the help of this diagnostic due to the low resolution of the UM-2 optical spectrometer.

As a rule, the panoramic spectrum was a combination of discrete and continuous spectra. However, continuum spectrum was practically absent (Fig. 10a) at small wire diameters (10 μm), and for large wire diameters (200 μm) the intensity of it was so great that in the red region of optical spectrum range a discrete component generally is not visible on the continuum spectrum background (Fig. 10c). As seen from Fig. 10b for the mid-value diameters (70 μm), the intensities of discrete and continuous spectrum were approximately the same.

The study of the behavior of time dependence of integral light intensity was carried out using a semiconductor

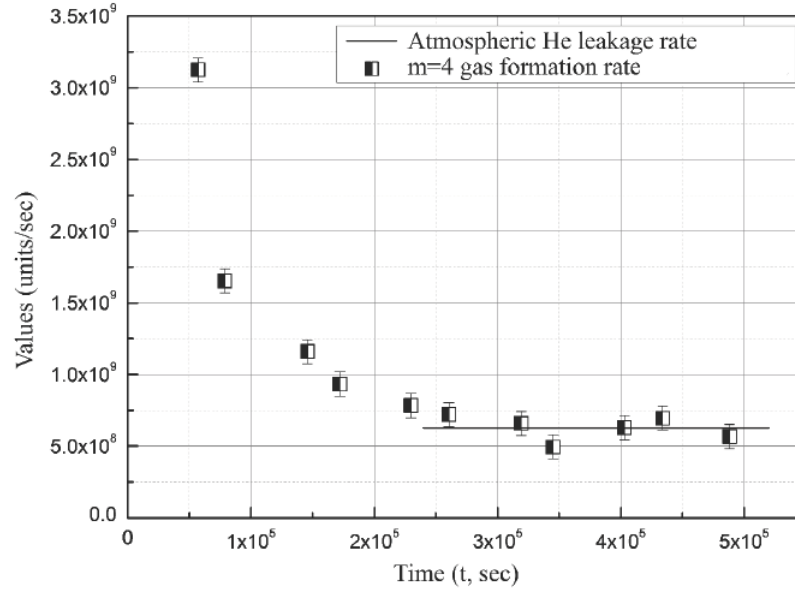


Figure 9. The rate of $m = 4$ particles formation in the chamber after the EEC (experiment No. 54).

photodiode in addition to the registration of the spectra. It has been found that for the wires with diameter larger than $100 \mu\text{m}$, radiation intensity has two maxima. The maximum intensity of the second peak occurs at approximately $200 \mu\text{s}$ from the beginning of EEC. By this time, the capacitor bank has discharged almost completely, energy input into the wire has stopped, so the observed behavior of light seems very unexpected. The second peak does not appear for wires with a diameter of less than $100 \mu\text{m}$. The signals from the photodetector, adjusted to a common scale, are shown in Fig. 11.

Comparison of the spectral measurement results presented in Fig. 10 with the data from photodetector (Fig. 11) suggests that the presence of the first maximum of intensity of radiation is associated with a discrete component of the optical spectrum, and presence of a second peak – with a continuous component of the spectrum. This result is easily reproduced and was observed in each experiment with wires with diameters larger than $100 \mu\text{m}$. Based on the available experimental data, it is difficult to say anything certain about the physical cause of the second peak of integral light intensity. However, the fact that the distance between the light peaks does not depend of the diameter of exploded wire (see Fig. 11) suggests that the appearance of the second peak is associated with the plasma recombination on the chamber walls. Based on the above assumption, the average plasma expansion velocity can be estimated - $V_p \sim 2 \times 10^4 \text{ cm/s}$.

For a more precise identification of the spectral lines of optical radiation, an STE-1 spectrometer combined with the CCD array was used as a recording instrument. A few lines were observed in the panoramic spectra, but their identification was difficult due to the low resolution of the UM 2 spectrometer, so they were identified using the STE-1. They were: Na spectral lines double in the yellow region $\lambda_{\text{Na}} = 5889 \text{ to } 5895 \text{ \AA}$ (Fig. 12), atomic oxygen line $\lambda_{\text{O}} = 7771\backslash 7774\backslash 7775 \text{ \AA}$ (Fig. 13), and carbon ion line $\lambda_{\text{C}^+} = 7231 \text{ to } 7236 \text{ \AA}$ (Fig. 14).

Comparing our results with the results of [1] we can assume that it was those lines that Wendt and Irion observed in their experiment, but were unable to decipher.

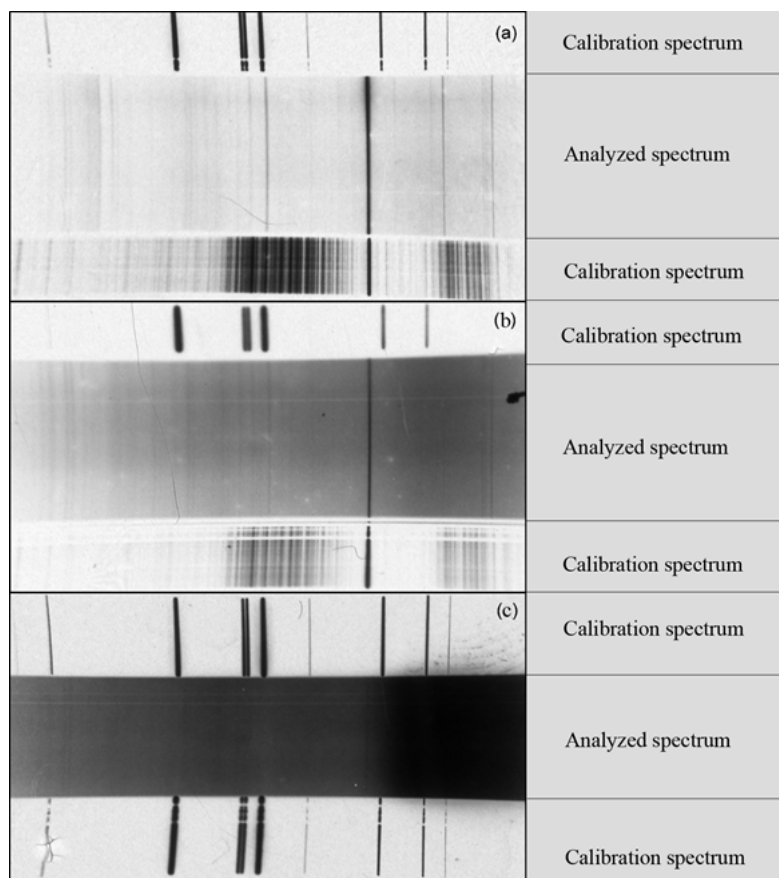


Figure 10. Panoramic radiation spectra of electric explosion of tungsten wires of different diameters: (a) 10 μm , (b) 70 μm and (c) 200 μm .

Registration of the emission spectrum of radiation with high resolution made it possible to measure the temperature of the electrons in the emerging tungsten plasma. A model of local thermodynamic equilibrium (LTE) has been used for the calculations [27,28]. Since the measurement of the absolute intensity of the lines – a very difficult task, the calculations use the relative intensities of the spectral lines, which were obtained through the study of individual spectral regions. Considering the possibility or strength of transition oscillator [29], tungsten plasma electron temperature has been determined for a number of spectral line pairs using the formula:

$$\frac{I_2}{I_1} = \frac{g_2}{g_1} \frac{f_2}{f_1} \frac{\lambda_1^3}{\lambda_2^3} \exp\left(-\frac{\Delta E}{kT_e}\right),$$

where I_i is relative intensity of the tungsten spectral lines, g_i the statistical weight of levels, f_i the transition oscillator strength, λ_i the spectral line wavelength, ΔE the difference between the excitation energies of investigated lines and T_e is the plasma electron temperature. Table 2 shows the values required to calculate relative intensities of the tungsten lines, experimental and tabulated values are given in [29]:

Table 2 shows that the average electron temperature in the tungsten plasma, formed as a result of EEC, is about 0.5 eV. As it can be seen the plasma temperature was several times smaller than the value that Wendt and Irion were

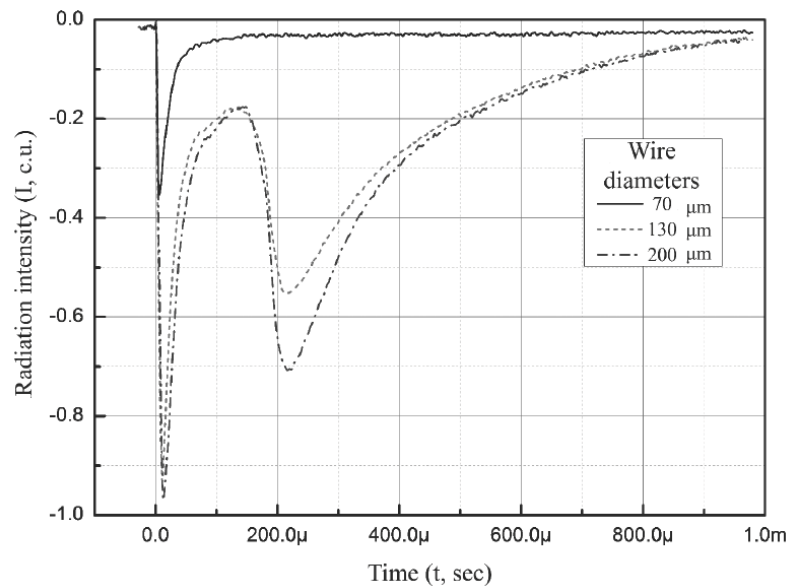


Figure 11. Time dependence of the integral light intensity for the wires of different diameters.

expected to reach in their experiments [1].

The data of optical spectral analysis and gas mass spectrometer showed clearly that the gas mixture with a high concentration of hydrogen appears in the explosion chamber after EEC. As for the helium presence in the gas phase formed after EEC, in many experiments, the data obtained with the help of the MS-40 indicated the presence of

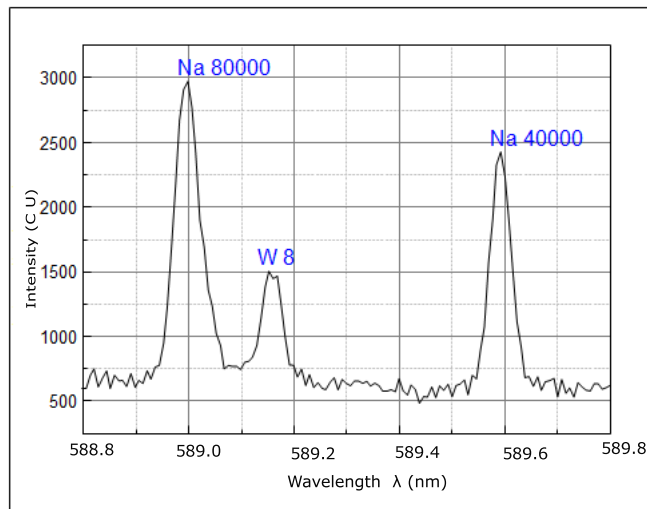


Figure 12. Fragment of high-resolution linear spectrum with Na spectral lines.

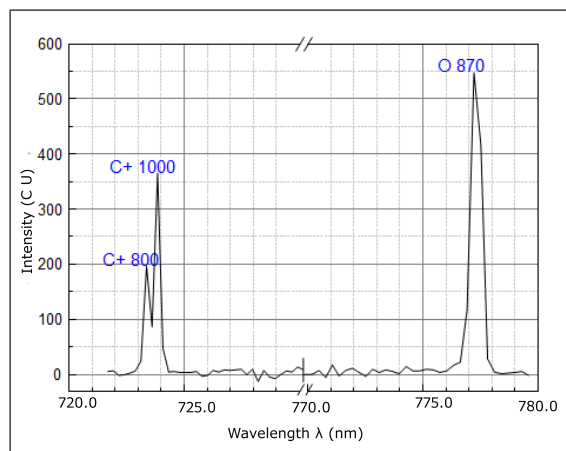


Figure 13. Fragment of spectrum with lines of atomic oxygen and carbon ion (next to the lines indicating its intensity, taken from a reference book) registered at the moment of the electric explosion using UM-2 with CCD-array as a recording element.

particles with $m = 4$ in the explosion chamber with a concentration greater than the concentration of ^4He in the atmosphere, but the He optical lines were registered only in several experiments. Therefore, the influence of hydrogen on the emissivity of the helium atoms was studied. These studies were carried out in a hydrogen–helium medium at various ratios of the partial pressures of ^4He and H_2 .

The plasma discharge was excited in the explosion chamber using the capacitor bank of “HELIOS” setup. A test mixture with a known concentration ^4He and H_2 was let into the chamber until the pressure is set up to $P \sim 1$ Torr, which is in order of magnitude corresponds to a pressure PB after the electric explosion. From verification experiments it follows that, with a ratio of $^4\text{He} : \text{H}_2 = 1 : 20$ the transition corresponding to ^4He wavelength $\lambda_2 = 6678.15 \text{ \AA}$ become barely visible, and strong molecular hydrogen line appears near the helium line with wavelength

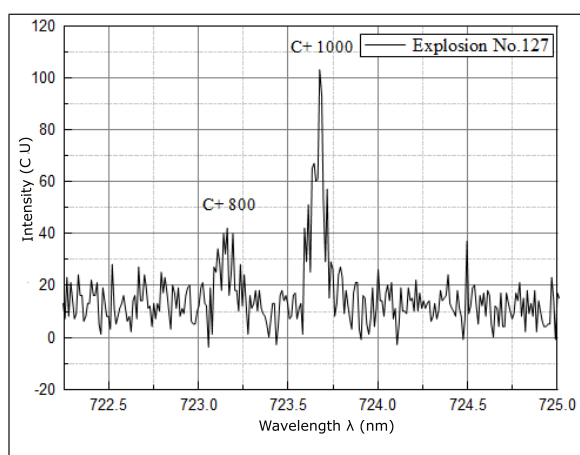


Figure 14. High resolution fragment of a spectrum with lines of carbon ion.

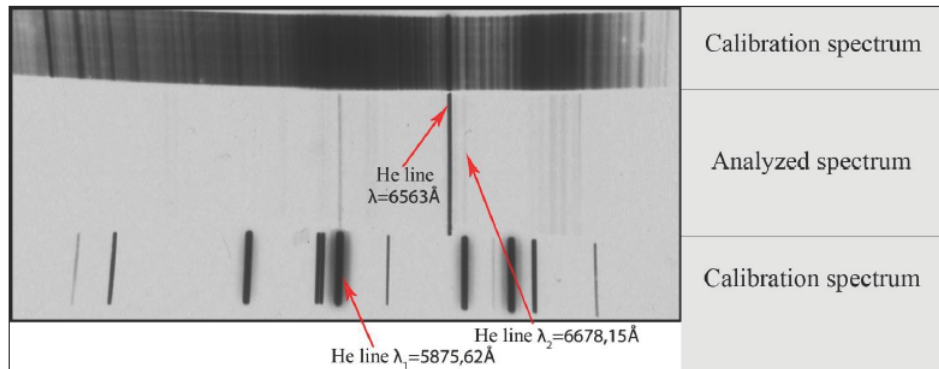


Figure 15. The radiation spectrum of gas mixture obtained after the series discharges.

$\lambda_1 = 5875.62 \text{ \AA}$. And with a ratio of $^4\text{He} : \text{H}_2 = 1 : 50$ helium line with a wavelength $\lambda_1 = 5875.62 \text{ \AA}$ ceases to radiate at all. Apparently excitement is removed due to collisions with hydrogen molecules. From the conducted methodical work, it is clear that, without reducing the partial pressure of hydrogen in the resulting gas mixture, identification of helium by optical methods at the time of EEC seems unlikely.

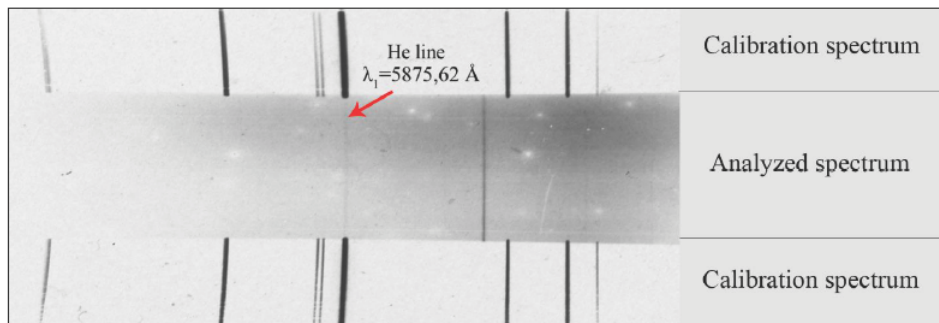


Figure 16. The radiation spectrum of the gas mixture obtained during the EEC.

Table 2. The values for the calculation of the electron plasma temperature.

$\Lambda(\text{\AA})$	$I(\text{relative units})$	$gf, \text{ ea.}$	$E(\text{cm}^{-1})$	$T_e \text{ (K)}$
5864.63	800	0.036	36 874	4568
5804.87	1200	0.45	43 452	
5947.58	870	0.016	30 587	
5735.09	1000	0.82	44 920	5295
6964.12	130	0.0022	14 355	5893
7140.54	310	0.0046	14 000	

From the dependence shown in Fig. 9, it follows that the number of atoms with $m = 4$ a.e.u., measured using the helium leak detector within 1–3 h after the EEC, by an order of magnitude greater than when measured immediately after the EEC. It should be noted that this result was quite unexpected. In addition, almost all of the hydrogen formed in the explosion chamber as a result of the EEC is pumped out through the leak detector during the first measurement of particles and thereafter no longer found in the chamber. Consequently, in the gas phase formed after the first measurement, ${}^4\text{He}:\text{H}_2$ ratio is significantly higher than in the gas mixture formed immediately after the electric explosion. The latter circumstance allowed us to hope that in the gas mixture with a higher ratio of ${}^4\text{He}:\text{H}_2$ we will be able to detect the helium optical spectrum. For the implementation of this idea, the residual gas, which was formed within several hours after the EEC, was excited with the help of high-voltage pulses in a quartz chamber and, in these conditions the spectrum shown in Fig. 15 was detected.

Since during the aperiodic EEC regime hydrogen generation is less than during the EEC with high Q -value, the ratio of ${}^4\text{He}:\text{H}_2$ at the moment of electric explosion is higher. This fact led to the registration of ${}^4\text{He}$ line ($\lambda_1 = 5875.62 \text{ \AA}$) directly at the moment of the EEC in one of the experiments. That spectrum is shown in Fig. 16.

3.3.3. The results of analysis of solid EEC product

The analysis of surface of quartz fragments of the explosion chamber was carried out to determine the chemical composition of solid products of the tungsten wire explosion. The analysis of the inner surface of the quartz chamber, in which a series of EEC experiments with tungsten wires were made, was conducted using a scanning X-ray photoelectron microprobe (PHI Quantera SXM).

The X-ray fluorescence analysis showed the presence of carbon, sodium and nitrogen. The presence of nitrogen appears to indicate that the quartz, in the preparation stage of the experiment, was not heated properly, because this effect is usually observed as a result of quartz contact with air.

Typically, the presence of carbon and sodium is interpreted as surface contamination, but the outer side of the same quartz cylinder fragment did not show any traces of Na spectral lines. The presence of Na and C spectral lines on the inner surface of the quartz chamber fragment, identified using XPS, is consistent with the results obtained by means of optical methods. Therefore, the presence of these elements is apparently not due to contamination of its surface.

For mass spectrometric analysis of solid residues obtained as a result of EEC, a laser mass spectrometer with magnetic separation of ions was used, with sensitivity of 10^{-4} – 10^{-5} at.%. Mass spectrometry analysis of the initial tungsten wire showed that it is made up of 98.5 at.% W atoms, and its original isotopic composition was totally natural. Isotopic analysis of the residues of tungsten wire after EEC showed a complete absence of tungsten isotope ${}^{180}\text{W}$, although in the initial wire, it was consistently detected at 0.14%. However, the statistical significance of these measurements is not sufficient to draw conclusions based on solid mass spectrometric measurements.

4. Conclusions

The following conclusions can be drawn from the data obtained.

- (1) The amount of gas formed as a result of EEC of tungsten wire is 10^{18-19} atoms, which coincides with the data in [1]; but most of the gas is formed by desorption. We can assume that in [1], most of detected gas was also from impurities. There was no hydrogen in the explosion chamber, but mercury vapor (from the mercury pump) was present in the glass bulb used in [1], which greatly eased the excitement of the levels of helium atoms. Based on its parameters, the explosion chamber in [1] was identical to the mercury-helium lamp. Thus, the number of helium atoms formed during the electric explosion of tungsten wire [1] could be quite small
- (2) Despite all measures taken we could not fully purge hydrogen from the system, which significantly complicated the diagnosis of He.

- (3) In some experiments, the presence of particles with $m = 3$ a.m.u. was detected with confidence. It was not possible to identify it uniquely, but current article presents experimental arguments in favor of the hypothesis that the registered $m = 3$ particles could be ^3He . This is an unexpected result, but it does not contradict the results of [1], although it is in contradiction with the stated theoretical premises.
- (4) The presence of atoms with $m = 4$ a.m.u. was reliably detected in the gas mixture formed after the electric explosion, but on the basis of available data it is impossible to be sure that these are helium atoms. Quantitative measurements show that the concentration of $m = 4$ atoms in the gas, formed after the electric explosion is higher than concentration of ^4He atoms in air mixture.
- (5) Contrary to expectations, the highest number of $m = 4$ atoms was detected not immediately after of EEC, but within 1–3 h after it.
- (6) In results similar to [1], several bright lines in the red part of the optical spectrum were observed, which were identified with the help of modern techniques.
- (7) No fast neutrons were observed during the EEC of tungsten wires.

Thus, the obtained results are not contrary to the results of Wendt and Irion. But, in order to confidently speak about presence of low energy nuclear reactions during EEC it is necessary to specify all the daughter nuclei and calculate the energy balance of reactions.

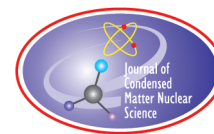
Acknowledgements

To our great regret, due to circumstances beyond our control, the present study remains unfinished, but it is still a pleasant duty to thank our colleagues for their help in carrying out the experiments: V.I. Mizhiritskii and R.M. Arshba, as well as our younger colleagues, students of MIPT: P.V. Belous, T.V. Shpakovskii, G.K. Steshenko, G.I. Zhotikov, A.A. Levanov and A.V. Steblevskii (IGIC RAS) for carrying out a solid mass spectrometry analysis; I.L. Fedechkin (Ioffe Institute) for help with the gas mass spectrometry; E.G. Silkis (Institute for Spectroscopy RAS) for help with the optical spectroscopy; D.V. Petrov (Skobeltsyn Institute of Nuclear Physics MSU) for carrying out analyzes on a scanning microscope; B.A. Lazba (Sukhumi Institute of Physics and Technology) for organizational support in the establishment of the laboratory and during the experiments. Special gratitude is for Anri Amvrosievich Rukhadze for interest in the work, stimulating discussions and scientific support.

References

- [1] G. L. Wendt and C.E. Irion, Experimental attempts to decompose tungsten at high temperatures, *Amer. Chem. Soc.*, Chicago **44** (1922) 1887–1894, Contribution from the Kent Chemical Laboratory, University of Chicago.
- [2] J.A. Anderson, The spectrum of electrically exploded wires, *Astrophys. J.* **51**, pp. 37–48.
- [3] E. Rutherford, *Nature* London **109** (1922) 418.
- [4] G.L. Wendt, *Science* **55** (1922) 567.
- [5] A.A. Volkov, A.P. Govorun, A.A. Gulyaev et al., Study of electric explosion of wires with microsecond current pulses in a longitudinal magnetic field (in Russian), *Zhurnal-tekhnicheskoy fiziki* **72** (2002) 115–120.
- [6] A.A. Rukhadze (Ed.), Exploding wires (in Russian), Moscow, IL, 1963.
- [7] A.A. Rukhadze and I.S. Shpigel (Eds.), *Electrical Explosion of Conductors* (in Russian), Moscow, MIR, 1965.
- [8] A.G. Russkih, R.B. Baksht, A. Yu. Labetsky et al., Influence of polarity of the high voltage electrode and pre-heating of tungsten micro-strip on its power characteristics in an explosion in vacuum (in Russian), *Fizika Plasmi*. Moscow **32**(10) (2006) 893–906.
- [9] V.A. Gribkov, Encyclopedia of low-temperature plasma (in Russian), Moscow: Yanus K **IX-3** (2007) 288–332.
- [10] S.S. Ananiev, Y.L. Bakshaev, P.I. Blinov et al. (in Russian), *Fizika Plasmi*. **36**(6) (2010) 1–9.
- [11] G.S. Volkov E.V. Grabowski, K.N. Mitrofanov and G.M. Oleinik (in Russian), *Fizika Plasmi*. **30** (2) (2004) 99.

- [12] R.B. Spielman, C. Deeney, G.A. Chandler et al., *Phys. of Plasmas* **5**(5) (1998) 2105–2112.
- [13] C. Cozzini et al., *Phys. Rev. C* **70** (2004) 064606.
- [14] O. Bohr and B. Mottelson, *Nuclear Structure*, Vol. 1, Benjamin, New York, Amsterdam, 1969.
- [15] V.A. Erma, *Phys. Rev.* **105** (1957) 1784.
- [16] D.V. Filippov, A.A. Rukhadze and L.I. Urutskoev, *Ann. Fond. L.de Broglie* **29** Hors Serie No. 3 (2004) 1207–1217.
- [17] S.V. Starodubtsev and A.M. Romanov, Radioactive transformations nuclei and nuclear envelope (in Russian), Tashkent: Publising House, *Proc. Akad. Uzbek SSR*, 1958, p. 495.
- [18] L.I. Urutskoev and D.V. Filippov, *Physics-Uspekhi*. **47**(12) (2004) 1257–1260.
- [19] H. Hatting, K. Hunchen and H. Waffer, *Phys. Rev. Lett.* **25** (1970) 941.
- [20] D.V. Filippov, L.I. Urutskoev, A.O. Biryukov, A.A. Rukhadze and P.V. Bilous (in Russian), *Prikladnaya Fizika* **4** (2012) 5–14.
- [21] F. Bosch, T. Faestermann, J. Friese et al., *Phys. Rev. Lett.* **77**(26) (1996) 5190–5193.
- [22] D.V. Filippov, *Phys. Atomic Nuclei* **70** (2) (2007) 258–264; **70**(12) (2007) 2016–2024.
- [23] L.I. Urutskoev, A.A. Rukhadze, Filippov D.V. et al., Study of the spectral composition of optical radiation during electrical explosion of a tungsten wire, *Bulletin Lebedev Phys. Institute* **39**(7) (2012) 199–203.
- [24] N.N. Aruev, A.V. Kozlovsky, I.L. Fedichkin et al. (in Russian), *JTP Lett.* **23** (1997) 83, 87.
- [25] Akulov, Yu. A. et al., Helium-isotope mass-spectrometric method for studying tritium beta decay (idea, experiment, nuclear and molecular physics applications), *Physics-Uspekhi* **46**(11) (2003) 1153.
- [26] J. Groszkowski, *Technika wyskiej prozni*, Wydawnictwa Naukowo-Techniczne, Warszawa, 1972.
- [27] R. Haddtstoun and S. Leonard, *Plasma Diagnostics* (in Russian), S. Yu. Lukyanova (Ed.), MIR, Moscow, 1967, 165 p.
- [28] Collection of Reports: Temperature and Its Measurement (in Russian), A. Armand and K. Wolfson, Moscow, Publishing House of Foreign Literature, 1960.
- [29] C. Corliss and W. Bozeman, The Transition Probabilities and Oscillator Strength Of 70 Elements (in Russian), R. Zolina (Ed.), MIR, Moscow, 1968, 515–518.



Research Article

Simulation of the Behavior of Exotic Neutral Particles by a Monte-Carlo Modelisation

Jacques Ruer*

Abstract

Hot spots are small features that some authors suppose are created by a sudden local release of thermal energy. For example, the estimation of the energy involved in the formation of a $2\ \mu\text{m}$ crater is $3 \times 10^{-8}\ \text{J}$ or $2 \times 10^5\ \text{MeV}$. Some theories attempting to explain these phenomena, and excess heat in general, involve the role of Exotic Neutral Particles (ENP), like Polyneutrons or Erzions. According to such theories, these ENPs are relatively rare. The problem investigated in this paper is whether a single particle may trigger a series of many reactions within a short time in solids that are properly loaded. A Monte-Carlo simulation has been written to study the potential behavior of ENPs. It is shown that the ENPs follow a developed and Brownian type movement. The number of reactions occurring at a given depth below the surface is calculated, as well as the probability for a series to exceed a given value. From a pure mathematical viewpoint, a parallel can be made between the diffusion laws and Brownian motion. It is shown that a small fraction of the ENP flux can trigger large series of reaction, to the point that the energy that can be produced is not limited if the ENP is stable as long as it is present in the lattice. It is necessary to introduce a limited lifetime with a decay to reconcile the model with the experimental observations. The discussion of the simulation results in the light of experimental data leads me to propose a mean free path on the order of $100\ \text{\AA}$, and a lifetime in the nanosecond range.

© 2017 ISCMNS. All rights reserved. ISSN 2227-3123

Keywords: Brownian motion, Exotic neutral particles, Hot spots, Monte-Carlo, Particle lifetime, Simulation

1. Introduction

Low Energy Nuclear Reactions (LENR) are thought to be responsible for the generation of excess heat in some experimental conditions. Positive experimental results have been obtained in many instances. This form of energy could prove immensely important in the future, but the lack of a comprehensive theory of the phenomena impedes the development.

LENR are difficult to explain if we base the theoretical analysis on classical physics. Many theories have been proposed to explain how atoms could fuse at relatively low temperatures [1,2].

Among these theories, one category involves the role of hypothetical particles that could lower the energy barrier between atoms and make reactions possible. The Polyneutron theory proposed by Fisher [3,4] proposes that neutrons are exchanged between nuclei.

*E-mail: jsr.ruer@orange.fr.

Bazhutov [5,6] supposes the existence of a hypothetical particle called Erzion, which could lead to a similar effect. Collis [7–9] remarks that these theories share common features and proposes the name Exotic Neutral Particle (ENP) to describe them. He thinks that the rates of reaction are expected to be very high, permitting a tiny number of ENPs to create substantial heat and transmutation products.

The purpose of this paper is to follow up on this basic idea and investigate some of the properties ENP would require to be able to describe the phenomena observed.

2. LENR Effects

LENR phenomena have been confirmed in different kinds of experimental setups, from electrolysis to gas phase reactors [1]. The excess power is reported to be sometimes as high as 1 W cm^{-2} . In some cases, the surface of the samples exhibits small features looking like tiny craters [10,11]. Figure 1 shows an example of craters. Some authors think that violent reactions caused the melting of the metal during the formation. If this is the case, it can be demonstrated that the crater formation is very rapid [12]. The energy required to create a crater has been estimated. For example, a crater with a diameter of $2 \mu\text{m}$ corresponds to an energy of $2 \times 10^{-9} \text{ J}$, released in about $6 \times 10^{-9} \text{ s}$. In other cases, hot spots have been detected with infrared cameras [10].

It can be calculated that the energy released during the formation of craters and hot spots is only a small fraction of the excess heat measured from samples during positive experiments. This means that besides localized energy, a large fraction of the energy is generated in a diffuse manner without leaving apparent traces.

This paper does not analyze the detailed mechanism of the reactions involving ENPs. The purpose is rather to examine how ENPs could produce sufficient quantities of energy to explain the observed phenomena. A model is presented which attempts to describe the statistical behavior of the ENPs, and to find out what the properties of these hypothetical particles should be in order to explain the experimental results.

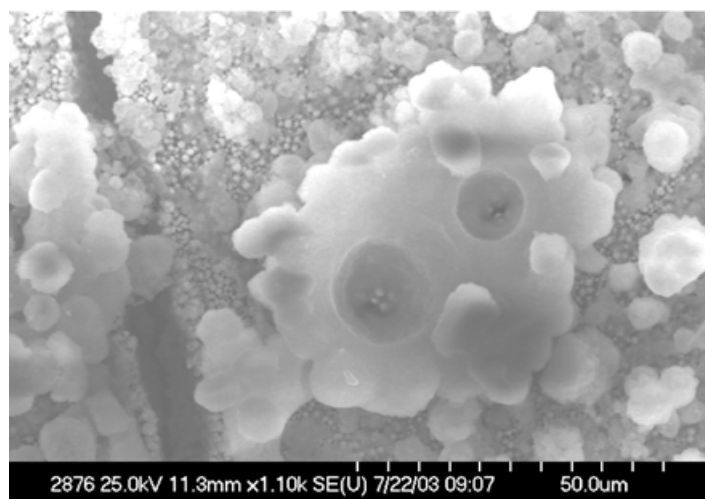


Figure 1. Example of craters observed after co-deposition experiment [10]. The rounded shape of the voids and the debris around the rim suggest that metal was melted during the formation of the craters.

3. Simulation Model

In order to develop a better understanding of the problem, a simple Monte-Carlo type model has been developed and written. The model assumes as a starting point that ENPs exist and are responsible for the LENR phenomena. The objective of the simulation is to compare mathematical results with the experimental results, in an attempt to develop some arguments in favor or against ENP theories. For instance, should the simulation lead to some contradiction between the hypotheses and the results of the simulation, the theory might have to be rejected. We see in the following that this is not the case. However, it is demonstrated that the ENPs should have specific properties to reconcile model and experimentation.

Assuming that ENPs are at the origin of the heat, the model must take into account the following assumptions:

- ENPs are deemed relatively rare. The logical consequence of this assumption is that a single particle should be able to trigger a series of many reactions within the metal lattice. One ENP is not destroyed by the reactions but remains available for further reactions, at least for some time.
- Some of the ENPs must remain a sufficient time to develop the quantity of energy corresponding to a hot spot or a crater.

3.1. Hypotheses

The following set of hypotheses {H} is taken into consideration to elaborate the simulation model. Figure 2 shows a sketch of the model:

- H1: The metal lattice, properly loaded and processed is reactive, so that the ENPs interacting with the lattice trigger LENR reactions.
- H2: One ENP enters the metal and triggers a first reaction at a given depth below the surface Z_0 . This depth may be zero.
- H3: After a reaction, the ENP retains its capacity to trigger further reactions.
- H4: The ENP travels along a straight line in the metal lattice until it reacts again.

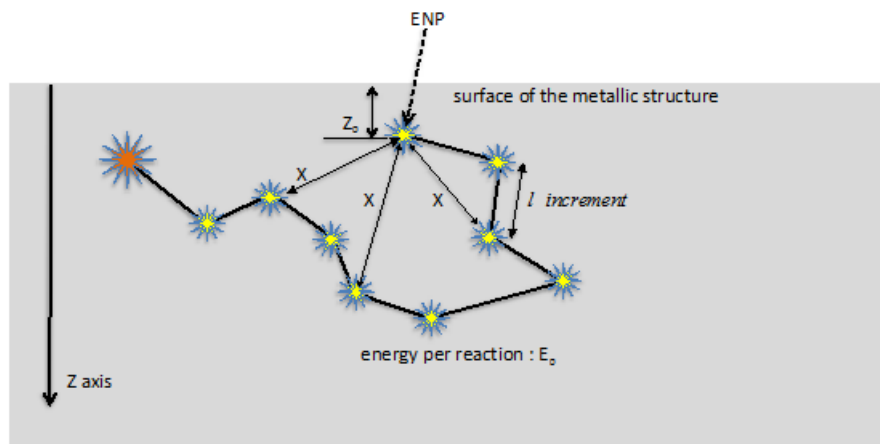


Figure 2. Sketch of the model – The ENP (origin unknown) starts to react at a depth Z_0 under the surface (Z_0 may be zero) – It travels at random in the lattice, triggering reactions at some spots – The activity stops if the ENP leaves the lattice, or after a given number of reactions Λ .

- H5: To simplify the model, all the reactions are assumed to be of the same nature and to release the same energy E_0 .
- H6: The direction of the velocity vector after a reaction may be completely independent of the velocity before the reaction, or this new vector may be compounded with a fraction of the vector before the reaction.
- H7: If the ENP trajectory again crosses the metal surface, the ENP is lost in the environment and the series of reactions is interrupted.
- H8: In the simulation, the series are limited by a maximum number of reactions, called the Life Number: Λ . This life number proves to be a governing factor for the overall behavior, as explained hereafter.
- H9: The space increment is given by a classical absorption exponential law [13]. The probability that a particle will travel at least a length l is represented by the equation:

$$P(l) = e^{-l/L_0}. \quad (1)$$

According to this equation, the mean free path is L_0 .

3.2. Basic assumptions

Three main unknowns can be identified in the simulation:

- (1) The value of the mean free path L_0 .
- (2) The average time lapse between successive reactions, which depends on the travel time along L_0 and of the reaction time itself of the excited compound. At this stage of the study, we suppose that the reaction time is zero. The moving velocity U of ENPs within the lattice is a parameter that is not known and needs to be evaluated.
- (3) The quantity of energy E_0 released by a single reaction. For the purpose of this simplified simulation, a precise value is not critical. According to the theories, not all reactions are alike, and the energies are different [2–9]. In this simulation, only an average value is required. We use, quite arbitrarily, an average energy of $E_0 = 4$ MeV per reaction. With this hypothesis, the formation of a $2 \mu\text{m}$ crater would correspond to 50 000 reactions.

3.3. Description of the model

The model is a Monte-Carlo simulation that operates as follows:

- One ENP is first located at the depth Z_0 .

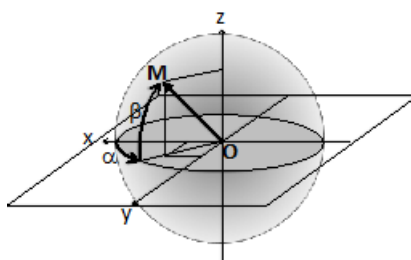


Figure 3. Generation of a new velocity vector OM.

- The three components of the new velocity vector are generated using two different pseudo-random number generators PRNG#1 and PRNG#2 (see Fig. 3). The method used to generate the random numbers is presented in the Appendix.
- The mean free path in the mathematical model is unity, by convention. The length l of the space increment between successive reactions is given by a third pseudo-random number generator PRNG3:

$C_n \in [0, 1]$ value from pseudo-random generator #3,

$$l = -\text{Log}(C_n). \quad (2)$$

- The new velocity vector may be compounded with a fraction of the old vector before the reaction, to take into account the conservation of the momentum in the interaction, should the ENP have a mass different from zero.
- The reactions are counted. The statistical distribution of the reactions around the introduction site is calculated. This makes it possible to evaluate the spatial distribution of the energy.
- The series of reactions for a given ENP is interrupted by one of the following events:
 - The ENP is located at a negative depth (escape out of the metal).
 - The number of reactions reaches the predefined Λ value.
- A new ENP is introduced and the simulation proceeds.
- In order to obtain representative statistical results, a large number of ENPs is used, from 10^5 to 10^7 .

$A_n \in [0, 1]$ value from pseudo random generator #1,

$B_n \in [0, 1]$ value from pseudo random generator #2,

$$\alpha = 2\pi A_n, \quad \alpha \in [0, 2\pi],$$

$$b = 2B_n - 1, \quad b \in [-1, +1],$$

$$\beta = \sin^{-1}(b), \quad \beta \in [-\pi/2, +\pi/2].$$

New velocity vector components:

$$V_x = \cos \alpha \cos \beta,$$

$$V_y = \sin \alpha \cos \beta,$$

$$V_z = \sin \beta.$$

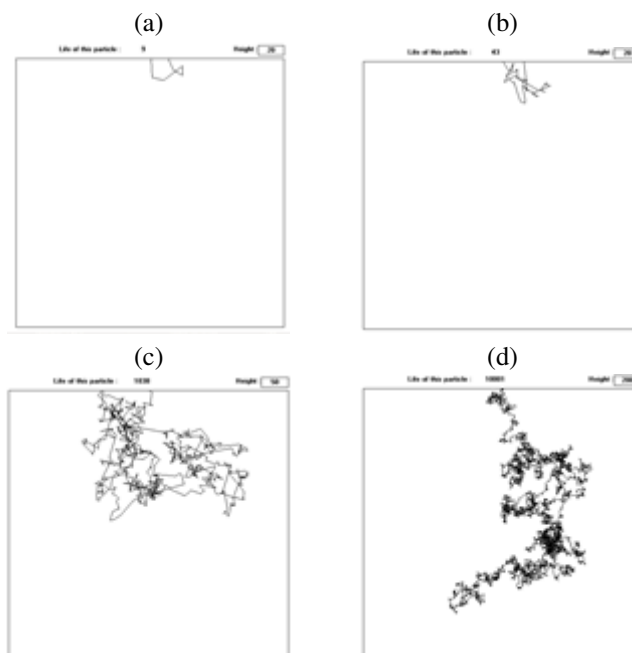


Figure 4. Typical examples of trajectories – Most ENPs give a small number of reactions (Fig. 4a or 4b). Only exceptional cases give long series (Fig. 4c or 4d) – Life numbers are, respectively 9, 43, 1038, and 10 001 – Please note that the different scales (Heights: 4a = 20, 4b = 20, 4c = 50, and 4d = 200 mean free paths).

4. Brownian Motion

This kind of simulation results in a random trajectory of the ENP. Some examples are shown in Fig. 4. They are typical of Brownian motion.

The above pictures display the trajectories of some individual ENPs. If we follow the behavior of many particles introduced at the same site, we obtain the statistical spatial distribution of the reactions, or the spatial distribution of the energy released. Figure 5 shows a typical result. One can see that for $Z_0 = 0$ the average energy distribution is contained in spheres tangent to the surface at the introduction point.

The mathematical definition of Brownian motion is the fact that the mean value of the squares of the excursions X (Eq. (3)) is proportional to the time [14,15]. Figure 2 illustrates the meaning of X . The distance, or excursion, travelled since $t = 0$ is measured in the $3d$ space, or projected along one direction ($d = 1$). We write Eqs. (3) and (4)

$$\langle X^2(t) \rangle = \frac{1}{t} \int_0^t X^2(t) dt, \quad (3)$$

$$\langle X^2(t) \rangle = dDt, \quad (4)$$

where X is the excursion of the particle at time t , d the dimensionality of the configuration ($d = 1$ for a 1-dimension diffusion problem and $d = 3$ for a 3-d space) and D is the diffusion coefficient.

Diffusion coefficients are measured in m^2s^{-1} . The model utilizes a length unit (L_0), which is unknown, and does not take the time into account. So, it can only verify the type of relationship, rather than the diffusion coefficient itself.

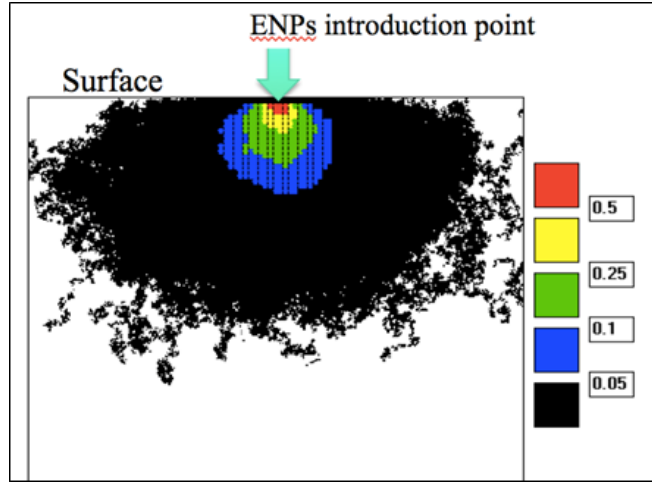


Figure 5. Spatial distribution of the reactions with many particles introduced at the same point on the surface. Result obtained with 10^5 particles - Life Number $\Lambda = 10^4$ - In this picture, the number of reactions are computed in a grid of 100×100 elements perpendicular to the surface. The third coordinate perpendicular to the plane of the picture is not monitored (all reaction spots are projected on the grid plane). The size of a grid element is $5L_0$. The color scale shows the ratio of the number of reactions in one grid element to the peak one in the grid element located just below the introduction point.

Figure 6 shows the results obtained by the model. The relationships between $\langle X^2 \rangle$ and the number of reactions n are

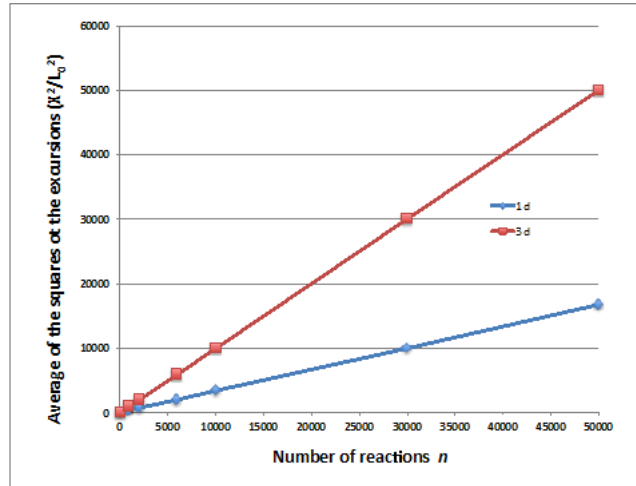


Figure 6. Results of simulations – Relationship between the number of reactions and the average square values of the excursions – For these calculations, Z_0 has been deliberately chosen very high so that no ENP could escape even for high life numbers Λ . All series have a number of reactions n equal to Λ . Equivalent diffusion coefficient $\Delta = 0.33$ in 1d and $\Delta = 1.0$ in 3d.

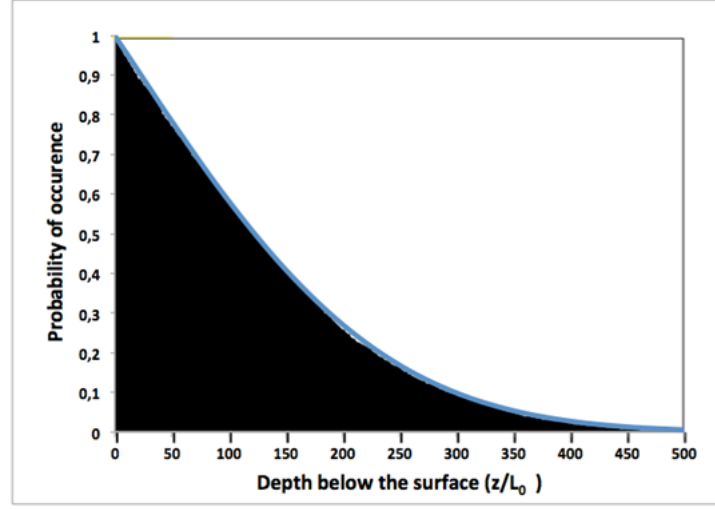


Figure 7. Comparison between the probabilities of occurrence calculated by the simulation and application of the second Fick's law – simulation with 10^6 particles and $Z_0 = 0$, Life Number $\Lambda = 50\,000$, and $\Delta = 1/3$.

linear, both in 1d or 3d, typical of Brownian motion:

$$\Delta = \frac{\langle X^2 \rangle}{nd}. \quad (5)$$

The value of the proportional constant is:

$$\Delta = 0.33 \quad \text{for } d = 1 \text{ along the } z\text{-axis,}$$

$$\Delta = 1.0 \quad \text{for the spatial diffusion } (d = 3).$$

It is known in the literature that a duality exists between Brownian motion and the diffusion described by Fick's equations [16]. The same behavior is found here again. Figure 7 compares the statistical presence of the ENPs at different depths obtained by application of the classical diffusion laws to the distributions given by the model for $Z_0 = 0$.

The statistical distributions of the model can be fitted with the curves (*in blue*) given by the equation, similar to the second Fick's law of diffusion:

$$C(z, n) = a \left[1 - \operatorname{erf} \left(\frac{z}{2\sqrt{\Delta n}} \right) \right]. \quad (6)$$

5. Statistical Results of the Simulation

5.1. Simulations with $Z_0 = 0$

The probability of occurrence of ENPs decreases as a function of depth. Most of the events are close to the surface. However, for large Λ values, the occurrence of ENPs at depths as large as a few hundreds of mean free paths is possible (see Fig. 7). When $Z_0 = 0$, half of the ENPs escape at the beginning of the sequence (see, e.g. Fig. 4a and b). On the other hand, some ENPs remain within the metal up to Λ , whatever its value.

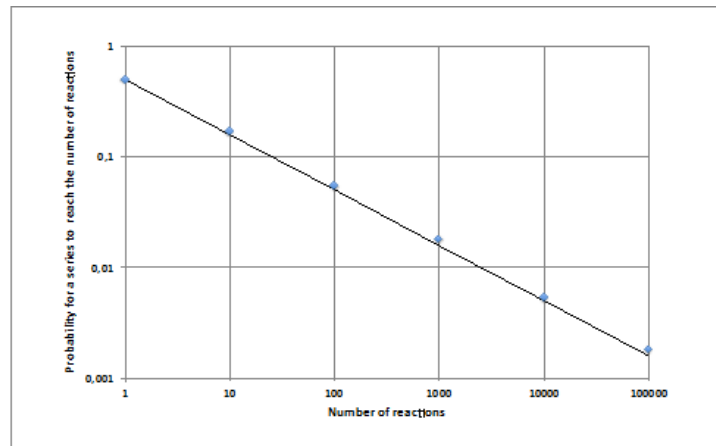


Figure 8. Proportion of particles still present under the surface after a given number of reactions – Calculations made with 10^5 particles – $Z_0 = 0$ – The line corresponds to Eq. (7).

Figure 8 shows the distribution of the probability for a particle to reside in the metal during a series of a given length. The graph uses logarithmic coordinates. It indicates that the probability that a series will reach a given number of reactions N is well approximated by the equation:

$$P(N) = 0.5 \times N^{-0.5}. \quad (7)$$

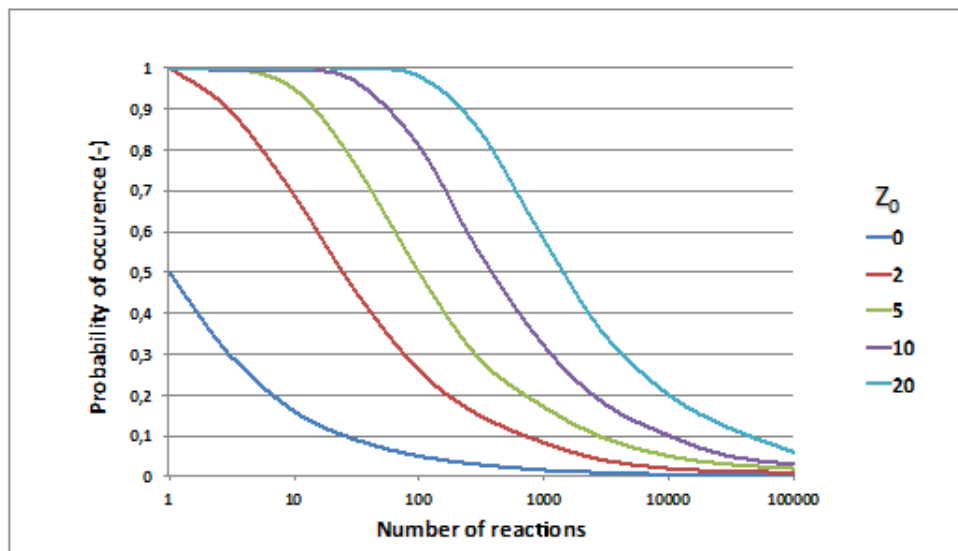


Figure 9. Distributions of probabilities for different Z_0 values.

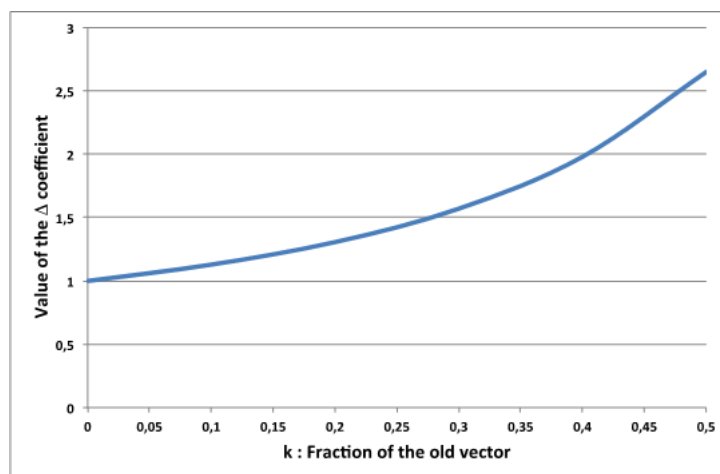


Figure 10. Influence of the compounding of the velocity vectors on the Δ coefficient.

5.2. Simulations with $Z_0 > 0$

If the first reaction takes place below the surface, the probability of observing a long series is greatly enhanced. Figure 9 shows the distributions of the probabilities to reach a given number of reactions for different Z_0 values.

It can be seen that the probability of a large series is increased even for modest Z_0 values. This is an important result, as shall be discussed below.

5.3. Simulations with compounded velocity vectors

The simulation can take into account a combination of the new velocity vectors after the reaction with a fraction of the velocity before the reaction. This combination represents the effect of the conservation of the momentum of the particles during the interaction. The value of k depends on the relative masses of the ENP and the atoms that are reacting.

$$\vec{V}_r = \left(k \cdot \vec{V}_{\text{old}} + \vec{V}_{\text{new}} \right). \quad (8)$$

The effect of the compounding is an increase in the diffusion coefficient Δ . Figure 10 shows the relationship between k and Δ .

The mass of the ENP is unknown. This simulation indicates that the influence of a mass greater than zero does not change the behavior to a great extent. The only effect is to increase the diffusion coefficient. The same effect would be obtained by the simulation with $k = 0$ and a mean free path equal to:

$$L = \sqrt{\Delta} L_0. \quad (9)$$

In the following, L is called the equivalent mean free path.

6. Discussion of the Results

It can first be remarked that most series end up with a modest value of the number of reactions. Such series could correspond to the majority of the events that contribute to the generation of heat but leave no traces on the samples.

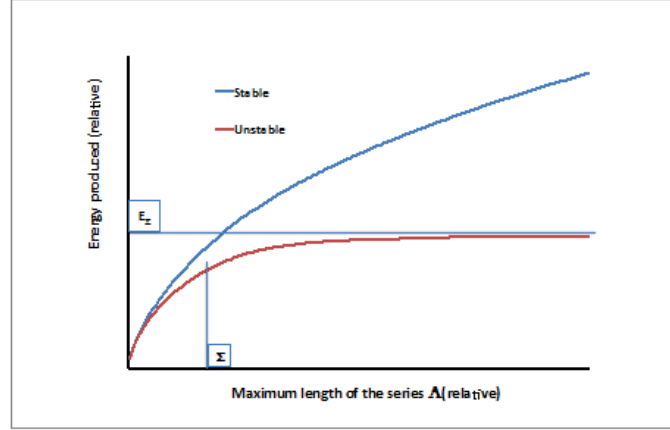


Figure 11. Schematic comparison of the energy released by stable and unstable ENPs. If ENPs are stable, there is no limit to the energy if there is no limit to Λ . If the ENPs are unstable, the energy converges to an asymptotic value for large reaction numbers Λ .

However, some series reach Λ , whatever its value. This is an essential result, because the major share of the energy released is created by the large series, as shown here. Let us consider again the occurrence probabilities calculated by Eq. (7).

The average energy produced by ENPs with a lifetime Λ can be calculated by the equation:

$$E = E_0 \int_0^{\Lambda} P(n) \, dn. \quad (10)$$

We obtain

$$E = E_0 \Lambda^{0.5}. \quad (11)$$

This equation gives a diverging result. If there is no limit to Λ , there is no limit to the average energy produced! This does not correspond to experience. Therefore, we must admit that Λ is limited for some reason. Potential phenomena able to provide the limitation are listed here. This list is probably not exhaustive.

- The energy locally increases the temperature. The lattice may lose its reactivity when the temperature is too high.
- The lattice may be active only in small spots. When the ENP leaves this active zone, it does not trigger additional reactions, even if it is present in the lattice, in an inactive area.
- The ENP may lose its properties prematurely.

Among these hypotheses, the last one is interesting. We may suppose that the ENP is unstable. Let us suppose that the ENP follows a decay law similar to radioactive elements. We write the probability of the presence of the ENP as

$$Q(t) = e^{-t/T}, \quad (12)$$

where T is the time constant of decay. The number of reactions is proportional to the time of presence, so that we can define a mean life number Σ , and the number of reactions during the time T . Equation (12) may be replaced by the

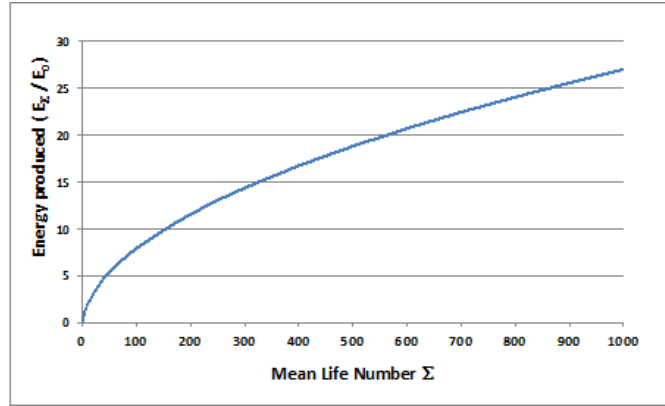


Figure 12. Relationship between Σ and E_{Σ} .

equation:

$$Q(N) = e^{-N/\Sigma}. \quad (13)$$

With this additional hypothesis, the probability that a series will reach the number of reactions N is the product of the probability of the series to reach N by the probability that the ENP will still be present at that moment:

$$P(N) = 0.5 N^{-0.5} e^{-N/\Sigma}. \quad (14)$$

The average energy E_{Σ} is then obtained by the equation:

$$E_{\Sigma} = E_0 \int_1^{\infty} 0.5 n^{0.5} e^{-n/\Sigma} dn. \quad (15)$$

Figure 11 compares the energies produced by ENPs that are stable and unstable. Figure 11 also shows that, although the average energy has a limit, some rare events are still possible yielding an amount of energy NE_0 even if N is larger than Σ . Figure 12 shows the relationship between Σ and E_{Σ} . Equation (15) is integrated via a numerical method.

We may conclude that the LENR energy created by an ENP depends on the number of reactions this particle triggers in the reactive lattice. In most cases, the number of reactions is limited to a value in the range of Σ . If we consider for example a surface power W of 1 W cm^{-2} , and $\Sigma = 10\,000$, the flux Φ of incoming ENPs should be:

$$\Phi = \frac{W}{E_0 \Sigma}. \quad (16)$$

For $E_0 = 4 \text{ MeV}$ or $6.4 \times 10^{-13} \text{ J}$, we obtain $\Phi = 1.5 \times 10^8 \text{ ENPs cm}^{-2} \text{ s}^{-1}$.

Some of the particles can trigger much more reactions than Σ . This may be the source of the craters. If Z_0 is different from zero, large series are frequent (Fig. 8). This does not reflect reality, otherwise craters would be the rule and their size would be larger than the few microns reported in the literature. Therefore, it should be concluded that ENPs, if they exist, react on the surface or at a very shallow depth.

Let us consider the case of $\Lambda = 50\,000$, and try to correlate the results with a typical $2 \mu\text{m}$ crater. Figure 7 shows that for this Λ value, the average of the squares of the excursions along the z -axis is 16 666. The square root of this value can be considered a measure of the penetration depth of the ENPs below the surface. This makes it possible to

make an estimation of the Mean Free Path:

$$\frac{Z_{\text{ave}}}{L} = \sqrt{16\,666} = 129 = 2 \times 10^{-6} \text{ m/L.} \quad (17)$$

We obtain

$$L = \frac{2 \times 10^{-6} \text{ m}}{129} = 155 \text{ Å.} \quad (18)$$

This estimation of the mean free path is an upper limit. If the crater is 2 μm in diameter, the Nuclear Active Environment responsible for its formation can only be smaller.

If we accept the time lapse of $\tau = 6 \text{ ns}$ for the formation of this 2 μm crater, we can derive the order of magnitude of the velocity U of the ENP travelling within the lattice:

$$50\,000 L = \tau U = 775 \times 10^{-6} \text{ m} = 6 \times 10^{-9} \text{ s } U. \quad (19)$$

We obtain:

$$U = 129 \times 10^3 \text{ ms}^{-1}. \quad (20)$$

Other assumptions regarding the average energy E_0 per reaction would lead to different values of Σ , Λ , L , T and U . However, this would not change the overall behavior revealed by this simulation.

If ENPs exist and are the source of the phenomenon, and according to the assumptions considered in this simulation, we conclude that:

- The mean free path of ENPs in the metal is in the 100 Å range.
- The lifetime is in the nanosecond range.

7. Conclusion

If we take as a hypothesis that craters are created by a local burst of heat and that ENP are at the origin of the phenomena observed, a mathematical simulation leads to the following conclusions:

- The ENP reacts first at the surface or very close to the surface.
- The mean free path of the ENPs in the crystal structure is in the range of 100 Å.
- The ENP is not stable in the lattice and decays in about 1 ns.

This simulation alone cannot produce confirmation of the theories based on ENP. It can only give some clues concerning their properties in order for them to explain the experimental results.

Acknowledgments

The author thanks the referee for his very helpful comments and suggestions, and Jed Rothwell for his precious editorial assistance.

Appendix

A.1. Generation of Pseudo-random Numbers

The model requires the generation of three suites of random numbers comprised in the interval $[0 - 1]$. There are many algorithms available in the literature able to satisfy this need [17]. The theory shows that true randomness is

Table A1. Parameters used for the pseudo-random number generators.

	Multiplier M	Divider D
PRNG#1	16811	31
PRNG#2	29717	17
PRNG#3	24571	53

not achievable by algorithms. They are therefore described as Pseudo-random Number Generators (PSNG). John von Neumann wrote: “Anyone who considers arithmetical methods of producing random digits is, of course, in a state of sin.” This problem is not critical, provided it is checked by statistical analysis that the PRNG suit the purpose of the intended use. In the present Monte-Carlo simulation, what is required is

- (1) PRNGs with a distribution density sufficiently uniform across the $[0 - 1]$ interval.
- (2) Three PRNGs, each giving numbers which are independent from the two others.

The author decided to use his own generators, and test the results obtained according to these requirements. This experience proved interesting, so that it is briefly reported here, to show to the reader examples of potential traps, and as a testimony to von Neumann’s words.

A.2. Algorithms Utilized

Most PRNGs are of the Linear Congruent type [18]. They are generally designed to generate pseudo-random numbers in large series, with a fast algorithm in order to minimize computation time. The general form is

$$X_{n+1} = (a X_n + c) \bmod m.$$

It can be demonstrated that the series generated have a period, dictated by the values of a and m . For details, see [18]. If $c = 0$, the generator is called a multiplicative congruential generator [18]. In the case of this study, the simulation was developed in Visual Basic, and the PRNGs had to use algorithms written in this language. The set of equations is

$$B = M X_n / D,$$

$$X_{n+1} = \text{frac}(B),$$

where $\text{frac}(x)$ is the fractional part of x :

$$\text{frac}(x) = x - \text{integer}(x).$$

All numbers are defined in double precision and are calculated with 15 digits. B is an intermediate result. The value of the new iteration X_{n+1} is the fractional part of the intermediate number B . M is called the multiplier and D the divider. These numbers must be relatively prime in order to obtain a satisfactory randomness. Table A1 gives the values utilized for the simulation. All values in the table are prime numbers.

The value of M/D is large in order to get a uniform distribution of the values over the interval $[0-1]$. Following the intended use of the PRNG, different validity tests should be performed. In order to test the uniformity, 10^7 draws were made, and classified in 1000 bins between 0 and 1. The average number of draws per bin is 10 000.

The theoretical variance is

$$\sigma = \sqrt{10\,000} = 100.$$

Table A2. Test of uniformity of the independent PRNGs.

	Variance
PRNG#1	268.67
PRNG#2	108.90
PRNG#3	106.96

Table A3. Test of correlation between odd and even iterations.

	Variance
PRNG#1	63.26
PRNG#2	26.27
PRNG#3	56.39

The results of the test are listed in Table A2. We see that PRNG#1 is seriously flawed, while the others seem to pass this test.

An additional test is the correlation between successive odd and even iterations. The 10^7 draws are classified in a 100×100 grid. There should be 500 draws per cell, and the variance should be 22.36.

Another method to visualize the results is to plot the number of draws per cell using a false color code, as shown in Fig. 13. The color scale extends from mean -4 sigma (*dark red*) to mean $+4$ sigma (*violet*). In the case of a satisfactory test, the spots should appear as a shade of green, ranging from yellow–green to green–light blue.

Figure 13 proves that the three generators do not pass this test. Patterns are clearly visible on all pictures, and in the case of PRNG#1 and 3, the green is not the dominant color.

A known method to improve the randomness is to combine several generators [19]. This is the method followed here. The three generators are combined in a cyclic fashion, as follows:

$$X1_n = \text{frac} [M1/D1X1_{n-1} + LX3_{n-1}],$$

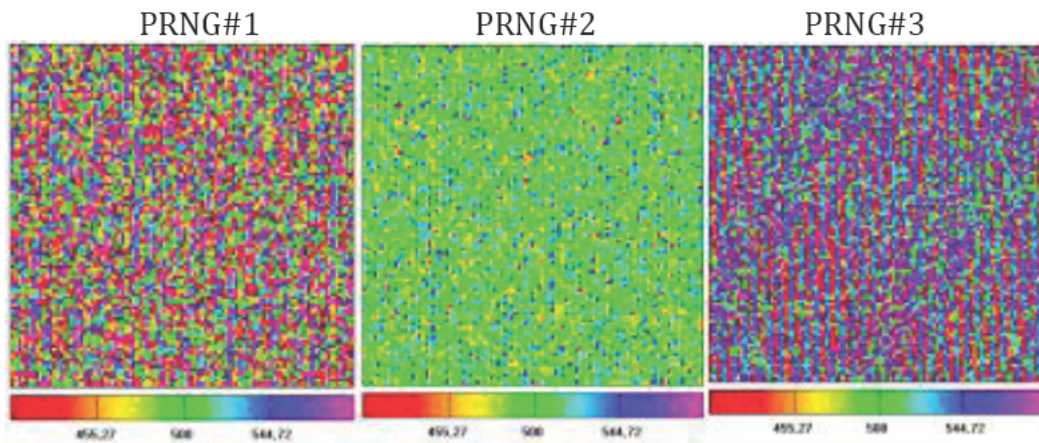


Figure 13. Correlation plots between odd and even iterations – 10^7 draws classified in 100×100 bins – Mean value per bin is 500 – sigma value is 22.36 – The color scale extends from mean -4 sigma = 410 (*dark red*) to mean $+4$ sigma = 589 (*violet*).

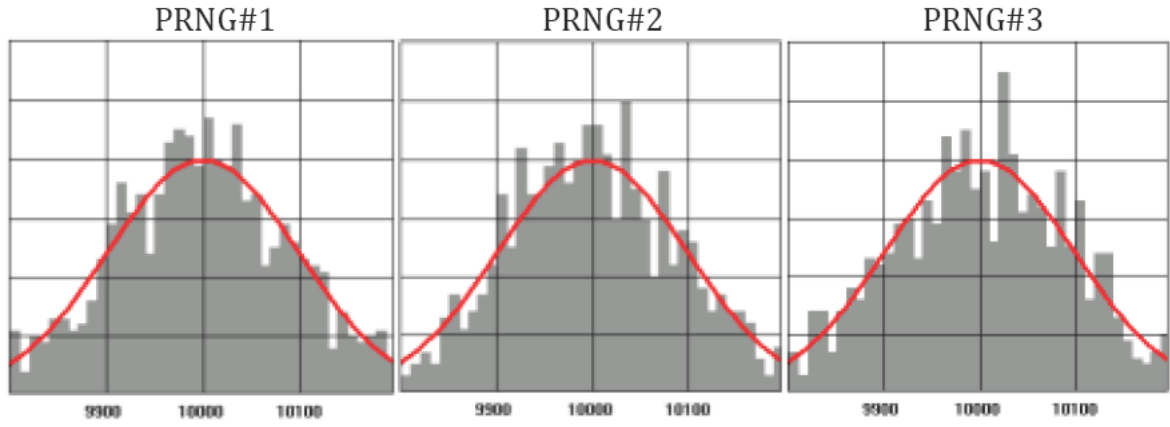


Figure 14. Histograms of the combined generators – $L = 3 - 10^7$ draws in 1000 bins – The red curves show the normal Gaussian distribution.

$$X2_n = \text{frac} [M2/D2X2_{n-1} + LX1_{n-1}],$$

$$X3_n = \text{frac} [M3/D3X3_{n-1} + LX2_{n-1}],$$

where L is a positive number called link L values different from zero improve the results of the uniformity test. All PRNGs passed this test with L larger than 1. Figure 14 shows the histograms of the combined generators with a link $L = 3$. Comparison of the histograms with the normal Gaussian distribution (*red curves*) shows that the statistical distribution is satisfactory.

Figure 15 shows the influence of L on the correlation test results. The three generators are considered acceptable and suited for the simulation with $L = 3$. The correlation test is satisfied if $L > 1$.

The color plots are reproduced in Fig. 16. The main color is now green. The generators are now linked via L . It is therefore necessary to check that they are not correlated. A similar procedure was followed to test the correlation

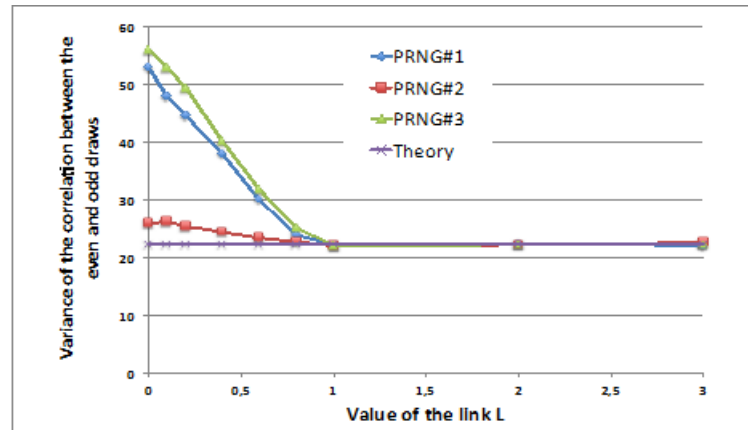


Figure 15. Influence of L on the variance of the correlation tests.

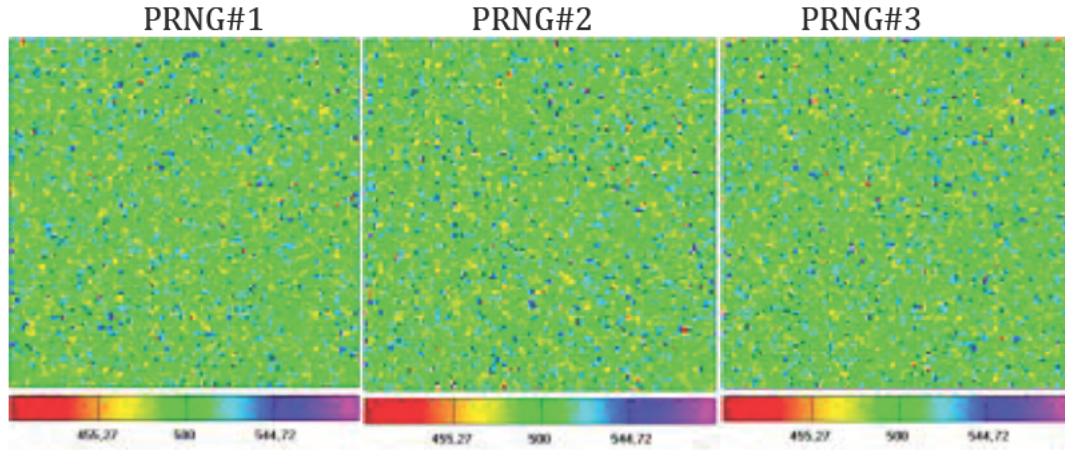


Figure 16. Color plots of the correlation plots test between odd and even iterations – 10^7 draws classified in 100×100 bins – Theoretical mean value per bin is 500 – Theoretical sigma value is 22.36 – The color scale extends from mean -4 sigma = 410 (*dark red*) to mean $+4$ sigma = 589 (*violet*).

between pairs of draws. Figure 17 shows the color plots and the variance of the different couples. The test is made with 10^7 draws classified in 100×100 bins. The mean number per cell is 1000 and the theoretical variance is: $\sigma = 31.62$. We see that the generators are not statistically correlated.

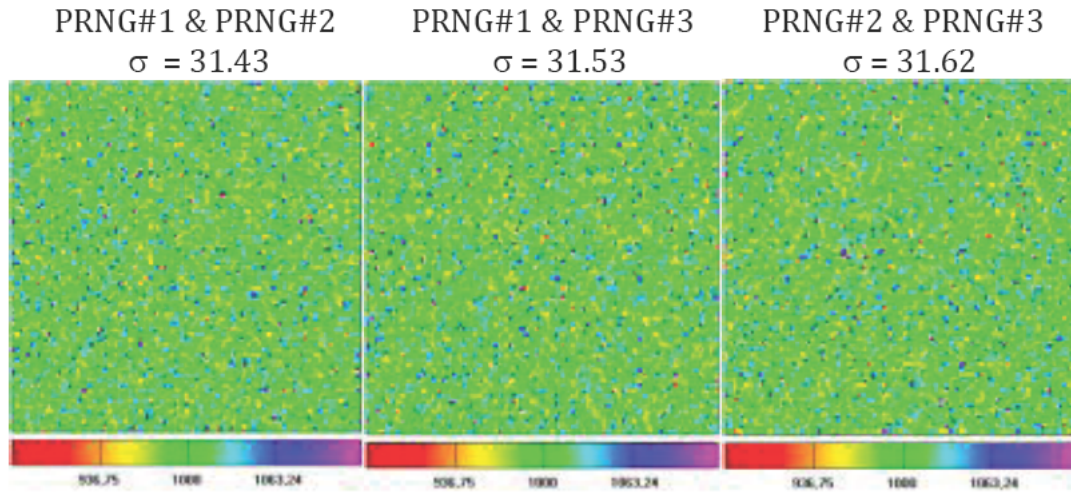


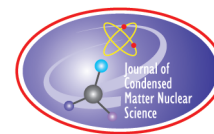
Figure 17. Correlation plots of couples of generators – 10^7 draws classified in 100×100 bins – Theoretical mean value per bin is 1000 – Theoretical sigma value is 31.62 – The color scale extends from mean -4 sigma = 874 (*dark red*) to mean $+4$ sigma = 1126 (*violet*).

A.3. Conclusion

This study shows that the PRNGs considered are suitable for the model used in this paper. They generate numbers uniformly distributed, and no statistical correlation is detected between the three generators. It is also shown that the random behavior desired might not be obtained in the first attempt, and that a thorough statistical analysis is necessary.

References

- [1] E. Storms, *The Explanation of Low Energy Nuclear Reaction*, Infinite Energy Press, ISBN 978-1-892925-10-7 (2014).
- [2] V.A. Chechin, V.A. Tsarev, M. Rabinowitz and Y.E. Kim, Critical review of theoretical models for anomalous effects in deuterated metals, *Int. J. Theoret. Phys.* **33** (1994) 617–670.
- [3] J.C. Fisher, Poly-neutrons as agents for Cold Fusion reactions, *Fusion Technol.* **22** (1992) 511.
- [4] J.C. Fisher, Neutron isotope theory of LENR process, *J. Condensed Matter Nucl. Sci.* **15** (2015) 183–189.
- [5] Y.N. Bazhutov, Erzion model features in cold nuclear transmutation experiments, *Proc. 8th Int. Workshop on Anomalies in Hydrogen/Deuterium Loaded Metals*, pp.12–18, www.iscmns.org/catania07/procw8.
- [6] Y.N. Bazhutov, Erzion model interpretation of the experiments with hydrogen loading of various metals, preprint of ICCF 17, *J. Condensed Matter Nucl. Sci.* **13** (2014) 29–37.
- [7] W. Collis, Nuclear reactions of cold fusion – a systematic study, *Proc ICCF5*, Monte Carlo.
- [8] W. Collis, ENSAP software tool to analyse nuclear reactions, in *The Seventh Int. Conf. on Cold Fusion*, 1998, Vancouver, Canada: ENECO Inc., Salt Lake City, UT.
- [9] W. Collis, Improving the Erzion model, *Book of abstracts of the 8th Int. Workshop on Anomalies in Hydrogen/Deuterium Loaded Metals*.
- [10] S. Szpak, P.A. Mosier-Boss and F.E. Gordon, Experimental evidence for LENR in a polarized Pd/D lattice, NDIA 2006 Naval S&T Partnership Conference, Washington DC, <http://lenr-canr.org/acrobat/SzpakSexperiment.pdf>.
- [11] David J. Nagel, Characteristics and energetics of craters in LENR experimental materials, *J. Condensed Matter Nucl. Sci.* **10** (2013) 1–14.
- [12] J. Ruer, Simulation of crater formation on LENR cathodes surfaces, *J. Condensed Matter Nucl. Sci.* **12** (2013) 1–16.
- [13] https://en.wikipedia.org/wiki/Mean_free_path.
- [14] https://en.wikipedia.org/wiki/Brownian_motion.
- [15] https://fr.wikipedia.org/wiki/Mouvement_brownien.
- [16] https://en.wikipedia.org/wiki/Fick%27s_laws_of_diffusion.
- [17] https://en.wikipedia.org/wiki/Pseudorandom_number_generator.
- [18] https://en.wikipedia.org/wiki/Linear_congruential_generator.
- [19] https://en.wikipedia.org/wiki/Combined_Linear_Congruential_Generator.



Research Article

Nuclear Catalysis Mediated by Localized Anharmonic Vibrations

Vladimir Dubinko*

National Science Center “Kharkov Institute of Physics and Technology”, Kharkov 61108, Ukraine

Abstract

In many-body nonlinear systems with sufficient anharmonicity, a special kind of lattice vibration, namely, Localized Anharmonic Vibrations (LAVs) can be excited either thermally or by external triggering, in which the amplitude of atomic oscillations greatly exceeds that of harmonic oscillations (phonons) that determine the system temperature. The coherency and persistence of LAVs may have a drastic effect on quantum tunneling due to correlation effects discovered by Schrödinger and Robertson in 1930. These effects have been applied to the tunneling problem by a number of authors, who demonstrated a giant increase of sub-barrier transparency during the increase of the correlation coefficient at a special high-frequency periodic action on the quantum system. Recently, it has been proposed that discrete breathers (a sub-class of LAVs arising in periodic systems) present the most natural and efficient way to produce correlation effects in regular crystals due to time-periodic modulation of the potential well (or the Coulomb barrier) width and hence to act as breather ‘nano-colliders’ catalyzing low energy nuclear reactions (LENR) in solids. It has been shown that the tunneling probability for D–D fusion under electrolysis of heavy water increases enormously with increasing number of oscillations resulting in the fusion rates comparable with those observed experimentally. In the present paper, we discuss possible ways of engineering the nuclear-active environment (NAE) and catalyzing LENR in NAE based on the LAV concept. We propose some practical ways of catalyzing LENR that are based on a special electro-magnetic treatment or electron and gamma irradiation, which could trigger LAVs in crystals and clusters.

© 2017 ISCMNS. All rights reserved. ISSN 2227-3123

Keywords: Correlation effects, Discrete breathers, Localized anharmonic vibrations, Low energy nuclear reactions, Nuclear active sites

1. Introduction

Catalysis is at the heart of almost every chemical or nuclear transformation process, and a detailed understanding of the active species and their related reaction mechanism is of great interest [1–3]. There is no single theory of catalysis, but only a series of principles to interpret the underlying processes. An important parameter of the reaction kinetics is the *activation energy*, i.e. the energy required to overcome the reaction barrier. The lower is the activation energy, the faster the reaction rate, and so a catalyst may be thought to somehow reduce the activation energy. Dubinko et al. have shown [4,5] that in a crystalline matrix, the activation energy may be reduced at some sites due to a special class of

*E-mail: vdubinko@hotmail.com.

localized anharmonic vibrations (LAV) of atoms, known also as *discrete breathers* [6] or *intrinsic localized modes* [7] arising in regular crystals. Discrete breathers (DB) can be excited thermally or by external driving, resulting in a drastic acceleration of *chemical reaction* rates in their vicinity. What is more, recently, discrete breathers have been proposed as *catalysts of nuclear D–D fusion* in palladium deuteride under heavy water electrolysis [8]. This new concept does not require any modification of *conventional nuclear physics* laws, in a marked contrast to the most of LENR models that attempted introducing various types of transient quasi-particles and structures such as Hydrino, Hydron, Hydrex, etc. that were created *ad hoc* to lower the Coulomb barrier, but which have not been verified by nuclear physics.

One of the most important practical ways to confirm the new concept is to look for the environment where the reaction is expected, which can be enriched with sites of *zero or small threshold energies* for the excitation of DBs. Such sites are expected to become the *nuclear active sites*, according to the model [8]. In this context, a striking *site selectiveness* of LAV formation in disordered structures [5] allows one to suggest that their concentration in quasicrystals may be very high as compared to regular crystals where DBs (a sub-class of LAV) arise homogeneously, and their activation energy is relatively high. Direct experimental observations [9] have shown that in the decagonal quasicrystal $\text{Al}_{72}\text{Ni}_{20}\text{Co}_8$, *mean-square thermal vibration amplitude* of the atoms at special sites greatly exceeds the mean value, and the difference increases with temperature. This might be the first experimental observation of LAV, which has shown that they are arranged just a few nanometers from each other, which means that their average concentration was about 10^{20} per cubic cm, which is orders of magnitude higher than one could expect to find in periodic crystals [4,5,8]. So in this case, one deals with a kind of ‘*organized disorder*’ that stimulates formation of LAV, which may explain the strong catalytic activity of some quasicrystals and open new ways towards *engineering of NAE* based on computer modeling of LAVs in periodic and aperiodic crystals and nano clusters. The main goal of the present paper is to develop this concept to the level of quantitative comparison with some of the LENR experiments and to suggest some practical ways of catalyzing LENR.

This paper is organized as follows. In Section 2, we briefly discuss the problem of tunneling through the Coulomb potential barrier, taking into account the *correlation effects*, as proposed by Dodonov et al. [10] and more recently by Vysotskii et al. [11]. A giant increase of sub-barrier transparency (up to hundreds of orders of magnitude) during the increase of the correlation coefficient at special periodic action on a quantum system will be demonstrated.

In Section 3, we will show that such an action can be most naturally achieved with time-periodic modulation of the width of potential wells for atoms oscillating in the vicinity of a DB or, more generally, LAV. We find the critical parameters of LAVs required to form *coherent correlated states* (CCS) via ‘parametric resonance’ conditions.

In Section 4, based on the LAV concept, an alternative to heating (currently used for triggering LENR) is proposed that is based on a special electro-magnetic treatment or electron irradiation, which can trigger LAVs in crystals and clusters and thus catalyze LENR. Methods of experimental verification of the proposed concept are discussed in Section 5. A summary and outlook is given in Section 6.

2. Tunneling enhancement due to formation of CCS in non-stationary potential well

2.1. Heisenberg uncertainty relation, Gamow TC and screening potential effects

The problem of tunneling through the Coulomb potential barrier during the interaction of charged particles is the key to modern nuclear physics, especially in connection with low energy nuclear reactions (LENR) observed in solids [12–14].

The tunneling (a.k.a. transmission) coefficient (TC) first derived by Gamow (1928) for a pure Coulomb barrier is

the Gamow factor, given by

$$G \approx \exp \left\{ -\frac{2}{\hbar} \int_{r_1}^{r_2} dr \sqrt{2\mu (V(r) - E)} \right\}, \quad (1)$$

where $2\pi\hbar$ is the Planck constant, E is the nucleus CM energy, μ is the reduced mass, r_1, r_2 are the two classical turning points for the potential barrier, which for the D–D reaction are given simply by $\mu = m_D/2$, $V(r) = e^2/r$. For two D's at room temperature with thermal energies of $E \sim 0.025$ eV, one has $G \sim 10^{-2760}$, which explains the pessimism about whether LENR can exist, and shows the need for some *special conditions* arising in solids under typical LENR conditions (D₂O electrolysis [12,13] or Ni–H reaction [14], etc.), which help to overcome the Coulomb potential.

Corrections to the cross section of fusion due to the screening effect of atomic electrons result in the so-called “*screening potential*”, which acts as an additional source of energy of collisions at the center of mass [15]. The screening potential was measured by the yields of protons or neutrons emitted in the D(d, p)T or D(d, n)³He reactions induced by bombardment of D-implanted solid targets with deuterons accelerated to kinetic energies of several keV, equivalent to heating up to $\sim 10^7$ K [16]. However, even the maximum screening potentials found in Pt (675 eV), PdO (600 eV) and Pd (310 eV) are far too weak to explain LENR observed at the temperatures of the experiments, which are below melting point of solids. Besides, the absence of significant radiation under typical LENR conditions indicates that *other reactions* should take place, based on interactions between ‘slow’ particles, which may be qualitatively different from the interactions between accelerated ones.

The most promising and universal mechanism of the stimulation of nuclear reactions occurring at low energy is connected with the formation of *coherent correlated states* of interacting particles, which ensures the large probability of nuclear reactions under these conditions, where the ordinary tunneling probability is negligible. These states minimize a more general uncertainty relation (UR), rather than the Heisenberg UR usually considered in quantum mechanics, namely, Schrödinger–Robertson UR [17,18], which takes into account *correlations between coordinate and momentum operators*.

2.2. Schrödinger–Robertson uncertainty relation and TC

The tunneling effect for nuclear particles is closely related to the uncertainty relation (UR), which determines, in fact, the limits of the applicability of the classical and quantum descriptions of the same object. It appears that the well-known and widely used Heisenberg UR is a special case of a more general inequality, discovered independently by Schrödinger [17] and Robertson [18], which can be rewritten in the following form [10,19]

$$\sigma_x \sigma_p \geq \frac{\hbar^2}{4(1-r^2)}, \quad r = \frac{\sigma_{xp}}{\sqrt{\sigma_x \sigma_p}}, \quad \sigma_{xp} = \langle \hat{x}\hat{p} + \hat{p}\hat{x} \rangle / 2 - \langle \hat{x} \rangle \langle \hat{p} \rangle, \quad (2)$$

$$\sigma_x = \left\langle \left(x - \langle x \rangle \right)^2 \right\rangle, \quad \sigma_p = \left\langle \left(p - \langle p \rangle \right)^2 \right\rangle, \quad (3)$$

where r is the *correlation coefficient* between the coordinate, x , and momentum, p , operators. At $r = 0$ (non-correlated state) Eq. (2) is reduced to the Heisenberg UR, while in a general case, a nonzero r in the UR can be taken into account by the formal substitution

$$\hbar \rightarrow \hbar_{\text{ef}} = \frac{\hbar}{\sqrt{1-r^2}}, \quad (4)$$

which leads to the formal shift of the border between the classical and quantum descriptions of the same object in the transition from noncorrelated to correlated state [11].

Then a natural question arises: can non-zero correlations lead to real physical effects? *The answer is yes*, and the most impressive consequence is a dramatic increase of the tunneling probability, if a real Planck constant in Eq. (1) can be replaced by the effective parameter (4). This substitution was indeed justified for a very low tunneling probability in the initially uncorrelated state $G_{r=0} \ll 1$ that corresponds to the condition $E \ll V_{\max}$ [11]:

$$G_{r \neq 0} \approx \exp \left\{ -\frac{2}{\hbar_{\text{ef}}} \int_{r_1}^{r_2} dr \sqrt{2\mu (V(r) - E)} \right\} = (G_{r=0})^{\sqrt{1-r^2}}. \quad (5)$$

From Eq. (5), it follows that when a strongly correlated state with $|r| \rightarrow 1$ is formed, the product of the variances of the particle coordinate and momentum increases indefinitely, and the barrier becomes practically ‘transparent’: $G_{|r| \rightarrow 1} \rightarrow 1$ even if $E \ll V_{\max}$.

Although the substitution $\hbar \rightarrow \hbar_{\text{ef}}$ (4) is not quite correct quantitatively, it clearly demonstrates the high efficiency of the correlations in applied tunneling-related problems in the case of a high potential barrier and a low particle energy $E \ll V_{\max}$, which is typical for LENR.

The physical reason for the huge increase in barrier transparency for a particle in a CCS is the *co-phasing* of all fluctuations of the momentum for various eigenstates forming the superpositional correlated state, which leads to great dispersion of momentum and large fluctuations of positions of a particle in the potential well and *under the potential barrier*.

A CCS can be formed in various quantum systems. The most effective way to form such state is to place a particle in a *non-stationary potential well*. Exact solutions to the non-stationary Schrödinger equation for the oscillating particle wave function $\psi(x, t)$ have been found by Vysotskii et al. [11], which will be considered in the following section.

2.3. Formation of CCS under time-periodic action on a particle in the parabolic potential

Consider a harmonic oscillator in a non-stationary potential well with eigenfrequency $\omega(t)$ changing with time, t , the Hamiltonian of which is given by

$$\hat{H} = \frac{\hbar}{2M} \frac{\partial^2}{\partial x^2} + \frac{M\omega(t)^2 x^2}{2}. \quad (6)$$

The solution of the Schrödinger equation for this Hamiltonian by Dodonov and Man’ko [10,19] gives the wave function of the correlated state having the time-periodic oscillating dispersion of the particle coordinate $\sigma_x(t)$:

$$\Psi_{\text{corr}}(x, t, r) = \frac{1}{\sqrt[4]{2\pi\sigma_x(t)}} \exp \left[-\frac{x^2}{4\sigma_x(t)} \left(1 - \frac{ir(t)}{\sqrt{1-r^2(t)}} \right) \right], \quad \sigma_x(t) = \frac{x_0^2}{2\sqrt{1-r^2(t)}}, \quad (7)$$

where $x_0 = \sqrt{\hbar/M\omega_0}$ is the amplitude of zero-point oscillations, which shows the scaling of the quantum problem. With increasing $|r| \rightarrow 1$ the dispersion increases indefinitely, which means that a probability of the particle localization in the sub-barrier region increases accordingly. For example, $x_0 \approx 0.56 \text{ \AA}$ for a hydrogen nucleus, and the probability of its tunneling to a distance comparable with the crystal lattice spacing (on the order of angstroms) drastically increases with increasing $|r|$.

A model system considered by Vysotskii et al. [11] to evaluate the correlation coefficient is a particle with the mass M , coordinate $x(t)$ and momentum $p(t)$ in a non-stationary parabolic potential well (i.e. non-stationary harmonic

oscillator),

$$V(x, t) = M(x(t))^2 (\omega(t))^2 / 2, \quad (8)$$

for which a change of the eigenfrequency $\omega(t)$ was shown to result in an increase of the absolute value of $|r(t)|$. Several scenarios of time evolution $\omega(t)$ have been investigated [11], including its monotonic decrease or periodic modulation. The latter regime can be provided, e.g. at a constant well depth V_{\max} if the potential well width $L(t)$ changes periodically resulting in a time-periodic modulation of the eigenfrequency as follows:

$$L(t) = L_0 (1 + g_\Omega \cos \Omega t), \quad L_0 = \sqrt{8V_{\max}/M\omega_0^2}, \quad (9)$$

where L_0 and ω_0 are the initial parameters of the well before the action of correlated forces, g_Ω and Ω are the modulation amplitude and frequency, respectively.

From a detailed analysis [11] it follows that the process of formation of strongly correlated coherent state with $|r|_{\max} \rightarrow 1$ in response to the action of limited periodic modulation is possible only at any of two conditions: (i) $\Omega = \omega_0$ (resonant regime) or (ii) $\Omega \approx 2\omega_0$, $|\Omega - 2\omega_0| \leq g_\Omega \omega_0$ (parametric regime). An analytical solution of the Schrödinger equation in the parametric regime was obtained by Dubinko, Laptev [20]. It shows that parametric modulation of a parabolic potential well results in the increase of the coordinate, momentum and mutual dispersion with increasing number of oscillation periods, N , which results in rapidly increasing probability to find the oscillating particle far beyond the characteristic length of the stationary well $\xi = \sqrt{\hbar/M\omega_0}$ (Fig. 1).

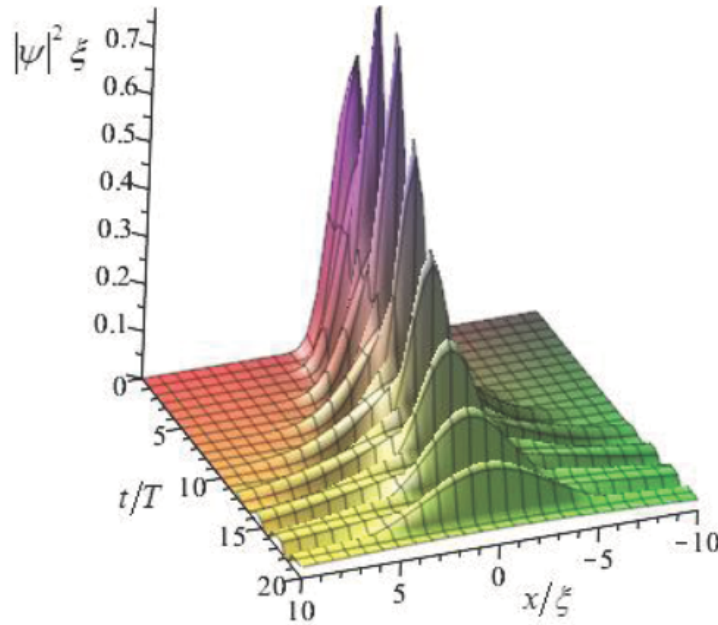


Figure 1. Localization probability distribution vs. the number of oscillation periods $N = \omega_0 t / 2\pi = t/T$ in the parametric regime $\Omega = 2\omega_0$ at $g_\Omega = 0.1$ [20].

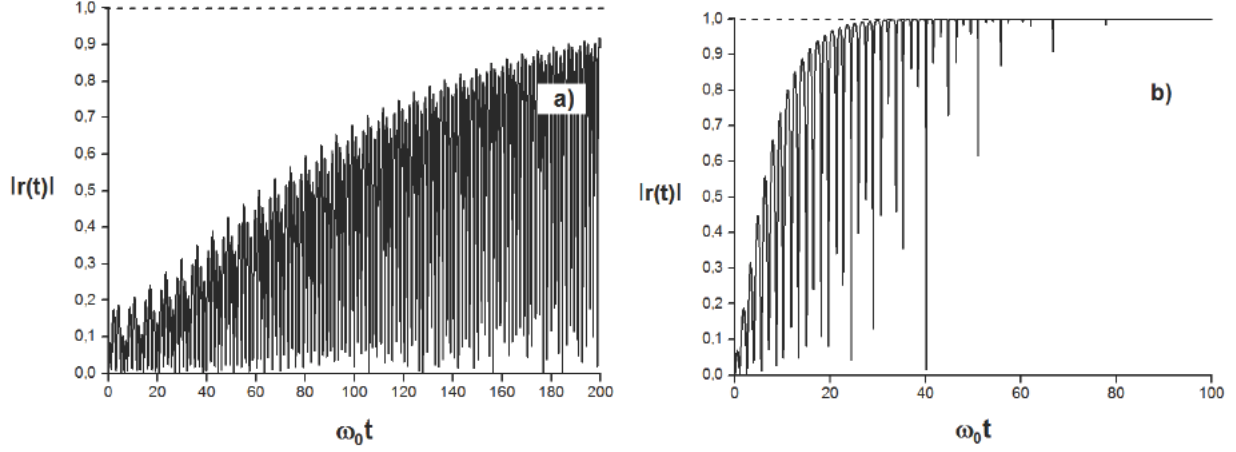


Figure 2. Correlation coefficient vs. time of action of the harmonic modulation of the well width given by eq. (10) at $g_\Omega = 0.1$ and two modulation frequencies: (a) $\Omega = \omega_0$ - resonant frequency, and (b) $\Omega = 2\omega_0$ - parametric resonance frequency [11].

Figure 2 shows evolution of the correlation coefficient in time under the action of the harmonic perturbation with frequencies $\Omega = \omega_0$ and $\Omega = 2\omega_0$ at $g_\Omega = 0.1$. Correlation coefficient oscillates with time but its amplitude $|r|_{\max}$ increases monotonously with the number of modulation cycles, $n = \omega_0 t / 2\pi$, resulting in a giant increase of the tunneling coefficient, as demonstrated in Fig. 3, which shows the TC evaluated by Eq. (10) that takes into account both the electron screening and the correlation effects [8]:

$$G^*(L, r) = \exp \left\{ -\frac{2\pi e^2}{\hbar_{\text{ef}}(r)} \sqrt{\frac{\mu}{2(E + e^2/L)}} \right\}, \quad (10)$$

where L is the minimum equilibrium spacing between D atoms determined by electron screening, E is their kinetic energy ($\sim eV/40$ at room temperature) \ll screening energy $\sim e^2/L$. One can see that the difference in electron screening and the corresponding initial D–D distances in a D_2 molecule ($L_0 = 0.74 \text{ \AA}$) and in the PdD crystal ($L_0 = 2.9 \text{ \AA}$) leads to a huge tunneling difference in the initial (uncorrelated) state, in which TC is negligible in both cases. However, with increasing number of modulation cycles, $\hbar_{\text{ef}}(r)$ increases according to Fig. 2 resulting in a giant increase of TC up to ~ 1 in several hundreds of cycles for $\Omega = \omega_0$ and in several dozens of cycles for parametric formation $\Omega \approx 2\omega_0$, which is more realistic to attain since it does not require exact coincidence of the frequencies [11].

The most important and nontrivial practical question now is how to realize such periodic action on an atomic scale? Modulation of the frequency of the optical phonon modes via excitation of the surface electron plasmons by a terahertz laser suggested in Ref. [11] as a driving force for the CCS formation is very questionable [8], and it does not explain LENR observed in the absence of the laser driving. In Section 3, we will consider a mechanism based on the large-amplitude time-periodic oscillations of atoms, which is an inherent LAV property.

3. LAV-induced Time-periodic Action on the Potential Barrier

3.1. Discrete breathers in bulk periodic crystals

The first attempts to develop a LENR mechanism in metal hydrides/deuterides (e.g. PdD or NiH) [8] were based on their crystal *periodic* structure, characteristic for *bulk* specimens or large particles. At ambient conditions, Pd

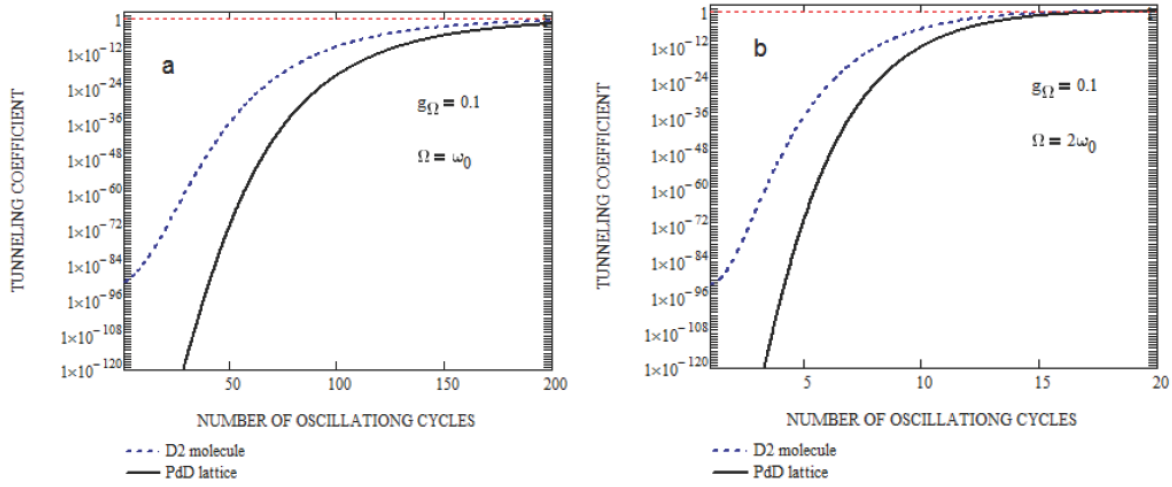


Figure 3. Tunneling coefficient increase with increasing number of the well modulation cycles, $n = \omega_0 t / 2\pi$, evaluated by Eq. (10) for $\Omega = \omega_0$ (a); $\Omega \approx 2\omega_0$ (b), $g_\Omega = 0.1$ for two D–D equilibrium spacings: in a D₂ molecule ($L_0 = 0.74$ Å) and in the PdD crystal ($L_0 = a_{\text{PdD}}\sqrt{2}/2 \approx 2.9$ Å). $a_{\text{PdD}} = 4.052$ Å is the PdD lattice constant at 295 K [8].

hydrides/deuterides crystallize in FCC structure with the space group of the Rock-salt [21], while Pd hydrides/deuterides crystallize in various structures corresponding to NiH, NiH₂ and NiH₃ [22]. Molecular dynamic (MD) simulations have revealed that diatomic crystals with Morse interatomic interactions typically demonstrate *soft type* anharmonicity [23], which means that DB's frequency *decreases* with increasing amplitude, and one can expect to find so-called gap DBs with frequencies within the phonon gap of the crystal. The large mass difference between H or D and the metal atoms is expected to provide a wide gap in the phonon spectrum, in which DBs can be excited either by *thermal fluctuations* at elevated temperatures (as demonstrated for the different weight ratios and temperatures [24]), or by some *external driving* providing a sufficiently large initial displacement of a light atom from its equilibrium position (Fig. 4).

Thus, the D–D fusion rate in *bulk* PdD should be determined by the generation rate of DBs having amplitudes near the critical value ~ 0.3 Å, which has been evaluated in [8] for typical LENR conditions, resulting in a qualitative and quantitative agreement with experimental data on the fusion rate under D₂O electrolysis at the fitted set of well-defined material parameters (Fig. 5a). In particular, the model explains the crucial role of electric current under electrolysis that produces the flux of energetic deuterons (in the eV range) through the cathode surface, which is a driving force for the DB generation. In the absence of electric current, the LENR rate is predicted to be lower by five orders of magnitude (Fig. 5b).

With increasing temperature, the concentration of DB increases, resulting in increased power generation, in a *qualitative agreement* with experiments [14] (Fig. 5b). However, the model predicts much more powerful LENR output above 600°C than what is observed in Ni–H reactions [14]. This discrepancy appears because the model [8] did not take into account effect of *temperature fluctuations* on the tunneling efficiency of DBs. As has been shown by Vysotskii et al. [26], fluctuations interfere with formation of CCS, which means that the *temperature effect is two-fold and controversial*. On the one side, heating helps to excite DBs but on the other hand, it decreases their tunneling efficiency. Therefore, the best way to facilitate LENR, according to the present concept, is to look for an environment which favors formation of DBs (or, more generally, LAVs) at lower temperatures than those explored in typical LENR

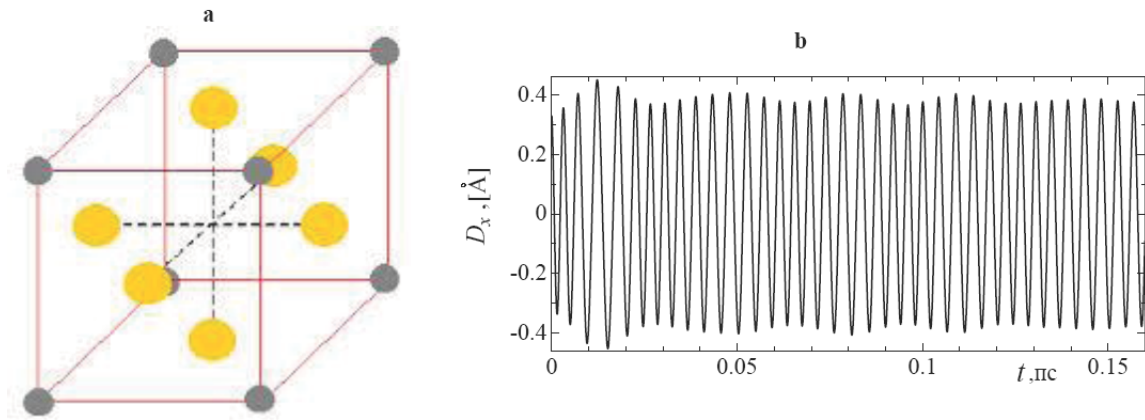


Figure 4. (a) A_3B compound based on FCC lattice with Morse interatomic potentials. Grey atoms are 50 times lighter than yellow ones. (b) DB initiated at zero Kelvin by the initial displacement $D_{x0} \sim 0.3$ Å of a light atom from its equilibrium position. It is localized on a single light atom vibrating along $\langle 100 \rangle$ direction with the frequency of 227 THz, which lies inside the phonon gap. Shown is the x -displacement of the light atom as the function of time. DB has a large amplitude of ~ 0.4 Å that should be compared to the lattice parameter of 1.35 Å [25].

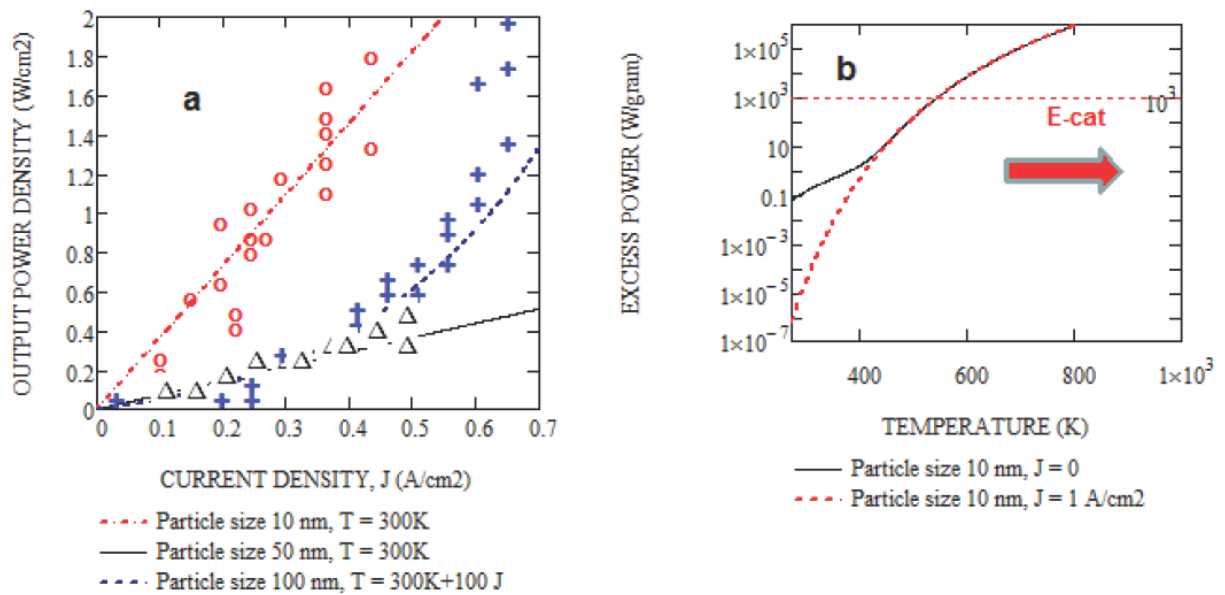


Figure 5. (a) LENR output power density according to the model in [8] vs. experimental data [13] as a function of electric current density at constant T and at T increasing with J as $T = 300$ K + 100 J. (b) LENR output power density according to the model [8] vs. temperature (broken line shows the power generation level in Ni-H reactions [14]).

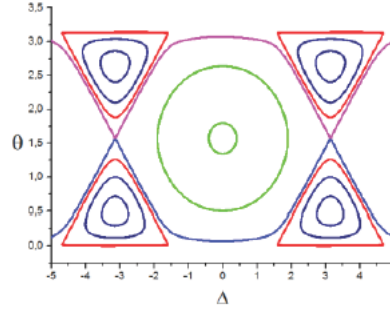


Figure 6. Phase diagram of two coupled anharmonic oscillators, according to the Ovchinnikov model [27] (see text). Separate regions in the diagram correspond to phase trajectories of the oscillators that *cannot share energy* [20].

installations. In Section 3.2, we consider LAVs in metal hydride/deuteride nanocrystals.

3.2. LAVs in nanocrystals and quasicrystals

The fact that the energy localization manifested by LAV does not require long-range order was first realized as early as 1969 by Alexander Ovchinnikov who discovered that localized long-lived molecular vibrational states may exist already in simple molecular crystals (H_2 , O_2 , N_2 , NO , CO) [27]. He realized also that stabilization of such excitations was connected with the *anharmonicity* of the intramolecular vibrations. Two coupled anharmonic oscillators described by a simple set of dynamic equations demonstrate this idea:

$$\begin{aligned}\ddot{x}_1 + \omega_0^2 x_1 + \varepsilon \lambda x_1^3 &= \varepsilon \beta x_2, \\ \ddot{x}_2 + \omega_0^2 x_2 + \varepsilon \lambda x_2^3 &= \varepsilon \beta x_1,\end{aligned}\quad (11)$$

where x_1 and x_2 are the coordinates of the first and second oscillator, ω_0 are their zero-point vibrational frequencies, ε is a small parameter, λ, β are the parameters characterizing the *anharmonicity* and the *coupling* force of the two oscillators, respectively. If one oscillator is displaced from the equilibrium and start oscillating with an initial amplitude, A , then the time needed for its energy to transfer to another oscillator is given by the integral:

$$T = \frac{\omega_0}{\varepsilon \beta} \int_0^{\pi/2} \frac{d\phi}{\sqrt{1 - (A^2 \gamma / 4)^2 \sin^2 \phi}}, \quad \gamma = \frac{3\lambda}{\beta}, \quad (12)$$

from which it follows that the full exchange of energy between the two oscillators is possible only at sufficiently small initial amplitude: $A^2 \gamma / 4 < 1$. In the opposite case, $A^2 \gamma / 4 > 1$, the energy of the first oscillator will *always be larger* than that of the second one. And for sufficiently large initial amplitude, $A \gg \sqrt{4/\gamma}$, there will be practically no sharing of energy, which will be localized exclusively on the first oscillator. This remarkable and seemingly *contra-intuitive* result is illustrated in Fig. 6 that shows the phase diagram of two coupled anharmonic oscillators.

Thus, Ovchinnikov has proposed the idea of LAV for molecular crystals, which was developed further for any nonlinear systems possessing *translational symmetry*; in the latter case, LAVs have been named *discrete breathers* (DBs) [6]^a or *intrinsic localized modes* (ILMs) [7]. Now, we are coming back to the idea of LAV arising at ‘active

^aNote that the term *discrete breathers* was coined nearly 20 years ago [6] in western nonlinear community, contrary to the recent comments [28] assigning the term to Ukrainian literature, while in the present paper we introduce a new and more general term ‘LAV’.

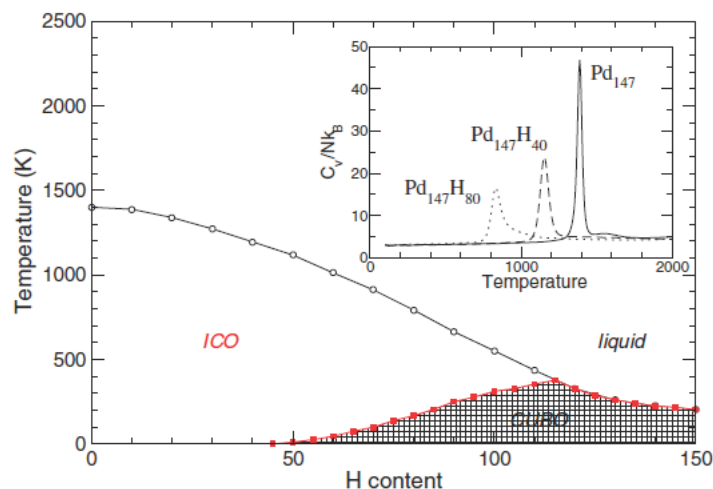


Figure 7. Schematic structural diagram of the $\text{Pd}_{147}\text{H}_x$ cluster in the icosahedral, cuboctahedral and liquid phases, after [32]. Inset: heat capacities of three clusters, in units of k_B per atom, versus canonical temperature. Icosahedral phase is predicted to be more stable above room temperature.

sites' in crystal defects, quasicrystals and nanoclusters. As noted by Storms [13], 'Cracks and small particles are the Yin and Yang of the cold fusion environment'. A physical reason behind this phenomenology is that in topologically disordered systems, sites are not equivalent and band-edge phonon modes are intrinsically localized in space. Hence, different families of LAV may exist, localized at different sites and approaching different edge normal modes for vanishing amplitudes [5]. Thus, in contrast to perfect crystals, which produce DB homogeneously, there is a striking *site selectiveness* of energy localization in the presence of spatial disorder, which has been demonstrated by means of atomistic simulations in biopolymers [5], metal nanoparticles [29] and, *experimentally*, in a decagonal *quasicrystal* $\text{Al}_{72}\text{Ni}_{20}\text{Co}_8$ [9]. In the latter case, the authors measured a so-called Debye–Waller factor defined by the mean-square thermal vibration amplitude of the atoms, and demonstrated that the anharmonic contribution to Debye–Waller factor increased with temperature much stronger than the harmonic (phonon) one. This was the first *direct observation* of a 'local thermal vibration anomaly', i.e. LAV, in our terms. The experimentally measured separation between LAVs was about 2 nm, which meant that their mean concentration was about 10^{20} per cm^3 that is many orders of magnitude higher than one could expect to find in periodic crystals [8].

The crystal shape of the nanoparticles (cuboctahedral or icosahedral) is known to affect their catalytic strength [30], and the possibility to control the shape of the nanoparticles using the amount of hydrogen gas has been demonstrated both experimentally by Pundt et al. [31], and by means of atomistic simulations by Calvo et al. [32]. They demonstrated that above room temperature the *icosahedral phase* should remain stable due to its higher entropy with respect to cuboctahedron (Fig. 7). And icosahedral structure is one of the forms quasicrystals take, therefore one is tempted to explore further the *link between nanoclusters and quasicrystals*.

Figure 8 shows the structure of $\text{Pd}_{147}\text{H}_{138}$ cluster containing 147 Pd and 138 H atoms having minimum free energy configuration, replicated using the method and parameters by Calvo et al. [32]. In particular, Fig. 8b reveals the presence of H–H–H chains aligned along the *I*-axis of the cluster. This *ab initio* simulation points out at the possibility of excitation of LAVs in these chains, with a central atom performing large-amplitude anharmonic oscillations and its neighbors oscillating in quasi-harmonic regime [34], which is similar to that considered in [8] for regular diatomic lattice of NaCl type. Such oscillations have been shown to stimulate formation of CCSs [8] and to facilitate LENR. In

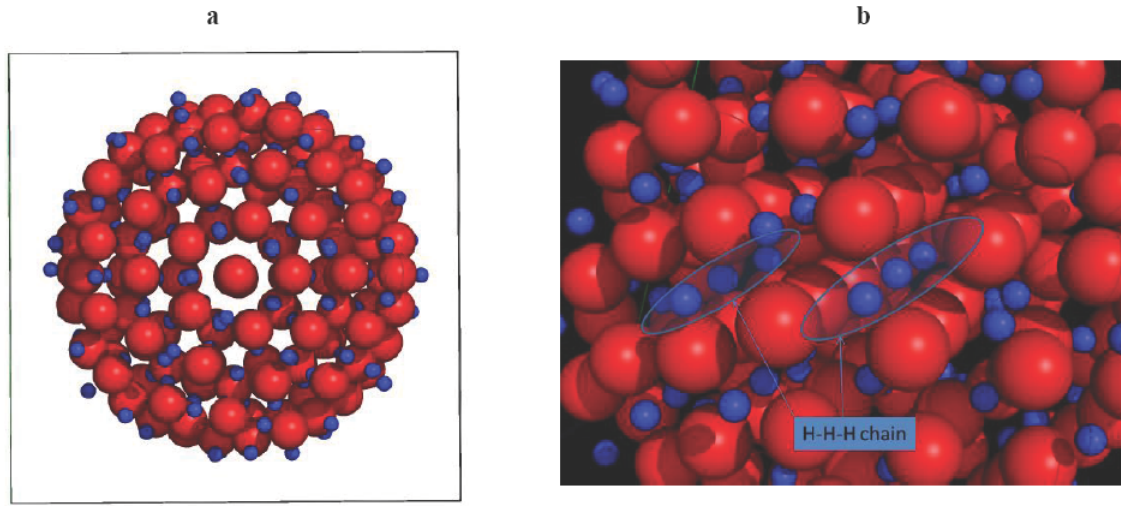


Figure 8. (a) Structure of PdH cluster containing 147 Pd and 138 H atoms having minimum free energy configuration, replicated in [33] using the method and parameters by Calvo et al. [32]; (b) H–H–H chains in the nanocluster, which are viable sites for LAV excitation [34].

Section 4, we will consider the ways of excitation of LAVs based on the present concept.

4. Ways of LAV-LENR Triggering

The main message of this paper is that the excitation of LAVs present an efficient way to produce CCS due to time-periodic modulation of the potential well width (or the Coulomb barrier width) and hence to trigger LENR in solids. As has been mentioned above, heating helps to excite LAVs but it decreases their tunneling efficiency. Therefore, we need ways to excite LAVs at sufficiently low temperatures, which is not a trivial problem technically.

One of the methods is based on time-periodic shaking of the surface atoms at frequencies near the optic phonon edge resulting in the LAV excitation in the sub-surface layers. Medvedev et al. [35] has demonstrated by means of MD simulations that gap DBs can be excited in the Al sub-lattice of Pt_3Al under the action of *time-periodic external driving*. Time-periodic shaking of the surface atoms at frequencies near the optic phonon edge resulted in the DB excitation in the sub-surface layers. These findings point out at the possibility of LENR stimulation by external time-periodic excitation of surface atoms. This method has been actually realized in terahertz laser experiments [36] on the stimulation of LENR by a joint action of two low-power laser beams with variable beat frequency ranging from 3 to 24 THz on the cathode surface during the D_2O electrolysis in the PdD system.

Figure 9 shows the experimental frequency dependencies of the excess power in these experiments. Three main resonances of excess energy released at $\sim 8 \pm 1$ THz, 15 ± 1 THz and 21 ± 1 THz have been shown in [8] to correlate with the DB-induced harmonic frequency, $\omega_0(A_{\text{cr}}) \approx 7.5$ THz, DB parametric frequency $\Omega(A_{\text{cr}}) \approx 15$ THz and DB initial frequency, 21 THz, respectively. According to the model in Ref. [8], the highest resonance is the biggest, since it is caused by amplification of DB excitation at the edge of optic phonon band. The medium resonance is due to tuning action of external driving on the DB frequencies: it increases the fraction of DBs with parametric frequency. The lowest resonance is due to tuning of harmonic frequencies by external driving: it increases the fraction of D atoms subjected to the parametric action by DBs.

The atoms are shaken by laser beams via excitation of the surface electron plasmons as suggested in [36]. It

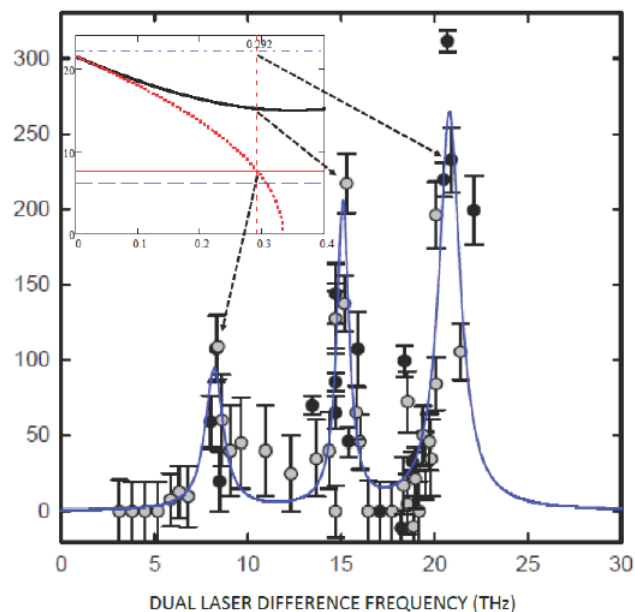


Figure 9. Excess power (mW) under joint action of two low-power laser beams with variable beat frequency on the surface of the Pd cathode during the electrolysis in heavy water [36]. The inset (from [8]) shows parity between critical DB-induced frequencies and the resonance frequencies [36] designated by dashed arrows.

explains the necessity of external magnetic field for producing resonance effects. However, the direct modulation of the frequency of the optical phonon modes by plasmons proposed in [11] as a driving force for the CCS formation is very questionable [8], and it does not explain LENR *observed in the absence of the laser driving* at slightly higher electric current or temperatures [36]. In the present view, the laser driving acts only as a tuning tool for the CCS formation by DBs induced in this case by joint action of temperature and electric current. Therefore, in order to stimulate LENR, one needs to apply some external triggering of LAVs similar to that provided by electric current under electrolysis conditions (below 100°C). Some phenomenological attempts to generate such triggering are currently underway [37,38], but the frequency range used in such attempts is far away from the LAV frequencies lying typically in THz diapason. These experiments did not show any evidence of excess heat within the accuracy of measurements. In the present view, this frequency mismatch may be responsible for the inefficiency of such triggering, which shows the need for a *physically based* frequency range and other methods of the LAV-LENR triggering.

From the experiments [36] on the resonant enhancement of excess heat generation by dual laser beams, one may conclude that the required frequency range lies in the terahertz diapason (8–20 THz in the Pd–D system). However, the exact value of the frequency required to trigger LAV-LENR in the Ni–H system *is not known* at present, and if the irradiation frequency does not match the LAV frequency, no effect is expected, in contrast to simple heating that excites all phonon modes. Therefore, the *first practical suggestion* of the LAV-concept is that one needs a laser with *variable frequency* in the THz range in order to fit the required frequency *in situ* experiments and trigger LENR.

The second suggestion is that instead of *heating*, which decreases the LAV efficiency, a *cooling* of the nuclear ‘fuel’ may result in the enhancement of the LENR output. This idea is illustrated in Fig. 10 which shows that the wave lengths corresponding to the desired frequency range (e.g. 6–30 THz) lie in the deep infrared diapason (10–50 μm),

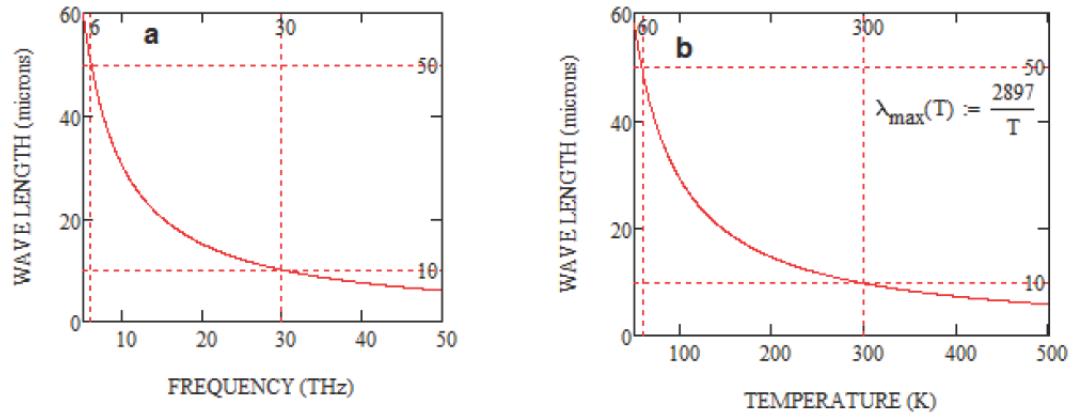


Figure 10. Wave length vs. frequency (a) and the maximum wave length vs. temperature of black body (b) according to Wien's law (1893).

which is emitted by a black body having temperature ranging from the room temperature down to liquid nitrogen temperature (Fig. 10b).

Thus, a combination of appropriate triggering with cooling may result in the extremely cold fusion and other

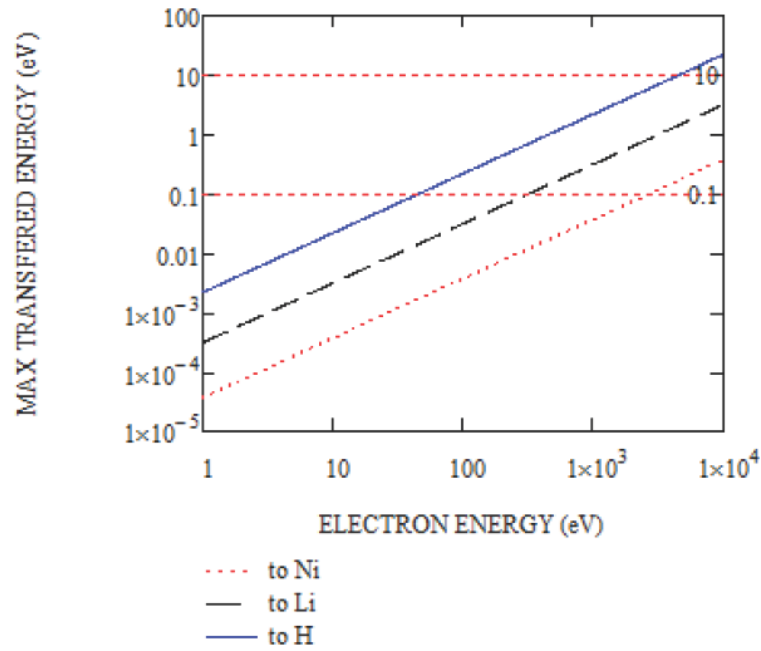


Figure 11. Maximum transferred energy of electrons to the target atoms (Ni_{58} , Li_7 and H_1) vs. the electron energy.

nuclear reactions in a nuclear active environment enriched with potential LAV sites.

5. Experimental Verification

As mentioned above [37,38], *a majority of attempts to replicate the Ni–H LENR failed*, which has led J.P. Biberian to the following conclusion [37]: “Reproducing Rossi’s experiment following Parkhomov’s process is not as easy as it seemed. After more than 20 experiments with nickel and LiAlH_4 in different configurations, within the precision of the calorimeter of ± 2 W, no excess heat was measured.”

However, there have been several successful LENR replications reviewed by Parkhomov [39,40], where the excess energy production in Ni–H has been observed in amounts exceeding those expected from chemical reactions. This controversy of different experimental results points out to the necessity of careful *examination and comparison of microstructures* of successful and unsuccessful fuels, and to the need to search the *new ways of triggering LENR*, which could result in a higher success rate.

One of the perspective ways of triggering LENR is to use *electron beams*. The point is that electrons hitting the target atoms displace them from equilibrium positions by a distance depending on the electron energy and the atomic mass. The displaced atoms start vibrating with frequencies inversely proportional to the initial displacements. If the frequency (i.e. initial displacement) matches the LAV frequency, a LAV is generated.

Figure 11 shows the dependence of the maximum transferred energy of electrons to the target atoms on the beam energy. It can be seen that in order to transfer energy between 0.1 and 10 eV to the light atoms H_1 or Li_7 (required to excite LAV) one needs electrons of keV energy range. It means that one needs a technology allowing electrons with keV energy range to interact with atoms inside the Ni–Li–H ‘fuel’ in order to catalyze LENR. However, *the problem* is that electrons of keV energies can penetrate only a few sub-surface atomic layers due to a strong scattering by the lattice, and hence, an *external electron beam* can excite only a thin surface layer. Dubinko [41] proposed a solution to this problem by using *Bremsstrahlung* gamma and *Characteristic* X-rays produced by accelerated electrons hitting a metallic converter and atoms of the fuel mixture.

For example, a tantalum converter has a characteristic tantalum peak at ~ 60 keV and another peak at ~ 150 keV. These gammas can penetrate up to a range centimeters deep, and they are absorbed by the Compton mechanism, which transforms them into electrons and gammas of lower energy *inside the fuel mixture*. Gammas with energies below 100 keV are converted *inside the fuel mixture* into electrons of the same energies due to the photoelectric effect. A part of resulting electrons will scatter at the fuel atoms elastically resulting in the energy transfer to them and hence to their displacement from equilibrium positions. Another part of electrons will produce characteristic X-rays inside the fuel mixture with energies determined by the fuel elements. For example nickel and aluminum will produce X-rays of ~ 8 and ~ 1.5 keV, respectively, which will be again converted to electrons of the same energies *inside the fuel mixture* by photoelectric effect. In this way, atoms entering the fuel mixture will be ‘kicked’ away from their equilibrium positions by electrons of different energies with local *Characteristic peaks* determined by the elements of the fuel. Adding various elements into the fuel mixture, it may be possible to change the energy spectrum of the ‘kicks’ and fit the required composition for the most effective *homogeneous* excitation of LAV in the fuel bulk, resulting in the LENR catalysis.

6. Conclusions and Outlook

In the present paper we argue that the excitation of LAVs presents an efficient way to produce CCS due to time-periodic modulation of the potential well width (or the Coulomb barrier width) and hence to trigger LENR in solids. This *LAV concept* is a natural extension of the breather nano-collider (BNC) concept proposed in [8]. In its initial form [8], it did not take into account quantum correlation effects, and hence, unrealistically small separation between atoms

($\sim 0.01 \text{ \AA}$) would have to be attained in order to enhance the LENR rate up to a noticeable level. Accounting for the correlation effects (Dubinko 2015) has shown that the *oscillation amplitude of several fractions of an angstrom* may be sufficient to produce the required effect, if CCS parametric conditions are met. Recent results obtained by a direct numerical solution of the time-dependent Schrödinger equation for a single nuclear particle in a harmonic [28] and double well potential [42] confirmed this view. It has been shown that these oscillations of the well width will periodically delocalize the nucleus and facilitate the tunneling of adjacent nuclei into the Strong Force attractive nuclear potential well, giving rise to nuclear fusion at rates that are *several tens of orders of magnitude* larger than what one calculates with the usual Gamow Factor integral relationship.

One of the important practical considerations following from the breather-induced correlation effects is that the breather *lifetime* plays more important role than the minimum distance between the oscillating nuclei.

Another critical parameter is the *mean concentration* of the CCS produced by the oscillations. In the present paper we extended the concept of *DBs* arising in perfect crystals homogeneously, to the *LAVs* that showed a striking *site selectiveness* of energy localization in the presence of spatial disorder, which has been demonstrated by means of atomistic simulations in biopolymers [5], metal nanoparticles [29] and, *experimentally*, in some quasicrystals [9]. The experimentally measured concentration of LAVs in the latter amounts to $\sim 10^{20}$ per cm^3 , which is many orders of magnitude higher than one could expect to find in periodic crystals [8].

Analysis of the LAV frequency range suggests that instead of the currently explored *heating*, which decreases the LAV tunneling efficiency, a *cooling* of the nuclear ‘fuel’ may result in the enhancement of the LENR output, provided that it is combined with an appropriate *triggering* of the LAV formation by a special *electro-magnetic or electron* irradiation.

In conclusion, we note that the present concept is based only on the *known physical principles* and on independent atomistic simulations of LAVs in crystals using realistic many-body interatomic potentials and on the *ab initio* simulations of the structure of Me–H clusters. Atomistic modeling of LAVs of various types in metal hydrides/deuterides is an important outstanding problem since it may offer ways of *engineering the nuclear active environment* and help to discover the frequency/amplitude range of LAVs required for LENR triggering.

Acknowledgements

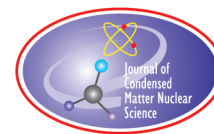
The author would like to thank Denis Laptev for designing Figs. 1,2 and 6; Sergey Dmitriev for Fig. 4; Dmitry Terentyev for Fig. 8, and Dan Woolridge for the LAV animation [34]. I thank Klee Irvin for attracting my attention to the new and promising field of quasicrystal research. Financial support from Quantum Gravity Research is gratefully acknowledged.

References

- [1] G. Ertl, H. Knozinger, F. Schuth, F., J. Weitkamp (Eds.), *Handbook of Heterogeneous Catalysis*, 2nd edn, Wiley-VCH, 2008.
- [2] R.S. Swathi and K.L. Sebastian, Molecular mechanism of heterogeneous catalysis, *Resonance* **13**(6) (2008) 548–560.
- [3] M. Yoshimura and A.P. Tsai, Quasicrystal application on catalyst, *J. Alloys and Compounds* **342** (2002) 451–454.
- [4] V.I. Dubinko, P.A. Selyshev and J.F.R. Archilla, Reaction-rate theory with account of the crystal anharmonicity, *Phys. Rev. E* **83**(4) (2011) 041124.
- [5] F. Piazza and Y.H. Sanejouand, Discrete breathers in protein structures, *Phys. Biol.* **5** (2008) 026001; V.I. Dubinko and F. Piazza, On the role of disorder in catalysis driven by discrete breathers, *Lett. Materials* **4** (2014) 273. <http://lettersonmaterials.com/en/Readers/Article.aspx?aid=712>.
- [6] S. Flach and A.V. Gorbach, Discrete breathers, *Phys. Rep.* **295** (1998) 181–264.
- [7] V. Hizhnyakov, M. Haas, A. Shelkan and M. Klopov, Theory and molecular dynamics simulations of intrinsic localized modes and defect formation in solids, *Phys. Scr.* **89** (2014) 044003-1-5.

- [8] V.I. Dubinko, Low-energy Nuclear reactions driven by discrete breathers, *J. Condensed Matter Nucl. Sci.* **14** (2014) 87–107, V.I. Dubinko, Quantum tunneling in gap discrete breathers, *Lett. Materials* **5** (2015) 97–104. <http://lettersonmaterials.com/en/Readers/Article.aspx?aid=810>; Vladimir Dubinko, Quantum Tunneling in Breather ‘Nano-colliders’, <http://www.lenr-forum.com/forum/index.php/Thread/1014-Breather-Nano-Collider-for-LENR-explanation/?postID=4300#post4300>.
- [9] E. Abe, S.J. Pennycook and A.P. Tsai, Direct observation of a local thermal vibration anomaly in a quasicrystal, *Nature* (London) **421** (2003) 347–350.
- [10] V.V. Dodonov and V.I. Man’ko, *Phys. Lett. A* **79**(2/3) (1980) 150.
- [11] V.I. Vysotskii and M.V. Vysotskyy, *Euro. Phys. J. A* **49** (2013) 99, DOI 10.1140/epja/i2013-13099-2.
- [12] M. McKubre, F. Tanzella, P. Hagelstein, K. Mullican and M. Trevithick, The need for triggering in cold fusion reactions, in *Tenth Int. Conf. on Cold Fusion*, MA, LENR-CANR.org., Cambridge, 2003.
- [13] E.K. Storms, *The Science of Low Energy Nuclear Reaction*, World Scientific, Singapore, 2007.
- [14] A.G. Parkhomov, *Int. J. Unconventional Sci.* **7**(3) (2015) 68.
- [15] H.J. Assenbaum, K. Langanke and C. Rolfs, *Z. Phys. A* **327** (1987) 461.
- [16] J. Kasagi, Screening potential for nuclear reactions in condensed matter, in *ICCF-14, Int. Conf. on Condensed Matter Nucl. Sci.*, 2008.
- [17] E. Schrödinger, *Ber. Kgl. Akad. Wiss., Berlin, S.* **24** (1930) 296.
- [18] H.P. Robertson, *Phys. Rev.* **34** (1930) 163.
- [19] V.V. Dodonov and V.I. Man’ko, Invariants and evolution of nonstationary quantum systems, *Proc. Lebedev Physics Institute*, Vol. 183, M.A. Markov (Ed.), Commack, Nova Science, New York, 1989.
- [20] V.I. Dubinko and D.V. Laptev, Chemical and nuclear catalysis driven by localized anharmonic vibrations, *Lett. Materials* **6** (2016) 16–21.
- [21] I. Errea, M. Calandra and F. Mauri, First-principles theory of anharmonicity and the inverse isotope effect in superconducting palladium-hydride compounds, *Phys. Rev. Lett.* **111** (2013) 177002.
- [22] S. Kanagaprabha, A. Meenaatci, R. Rajeswarapalanichamy and K. Iyakutti, First principles study of electronic structure, structural properties and superconductivity of nickel hydride, *Walailak J. Sci. Technol.* **9**(2) (2012) 115.
- [23] L.Z. Khadeeva and S.V. Dmitriev, Discrete breathers in crystals with NaCl structure, *Phys. Rev. B* **81** (2010) 214306 (8 pp).
- [24] L.Z. Khadeeva and S.V. Dmitriev, Lifetime of gap discrete breathers in diatomic crystals at thermal equilibrium, *Phys. Rev. B* **84** (2011) 144304 (8 pp).
- [25] S.V. Dmitriev, *Private communication*.
- [26] V.I. Vysotskii, S.V. Adamenko and M.V. Vysotskyy, Formation of correlated states and increase of the barrier transparency for low energy particles in nonstationary systems with damping and fluctuations, *J. Exp. Theoret. Phys.* **142** (2012) 627–643.
- [27] A.A. Ovchinnikov, Localized long-lived vibrational states in molecular crystals, *Zh. Eksp. Teoret. Fiz.* **57** (1969) 2137, *Sov. Phys. JETP*, **30** (1970) 116.
- [28] Louis DeChiaro, <http://www.e-catworld.com/2015/10/06/louis-dechario-of-us-naval-sea-systems-command-navsea-on-replicating-pons-and-fleischmann/>.
- [29] H. Zhang and J.F. Douglas, Glassy interfacial dynamics of Ni nanoparticles: Part II Discrete breathers as an explanation of two-level energy fluctuations, *Soft Matter* **9** (2013) 1266–1280.
- [30] *Metal Nanoclusters in Catalysis and Materials Science: The Issue of Size Control* (Eds.) B. Corain, G. Schmid, N. Toshima, 2008.
- [31] A. Pundt, A. Dornheim, M. Guerdane, H. Teichler, H. Ehrenberg, M.T. Reetz and N.M. Jisrawi, Evidence for a cubic-to-icosahedral transition of quasi-free Pd–H-clusters controlled by the hydrogen content, *Euro. Phys. J. D* **19** (2002) 333. (doi:10.1140/epjd/e20020080).
- [32] F. Calvo and A. Carré, Structural transitions and stabilization of palladium nanoparticles upon hydrogenation, *Nanotechnology* **17** (2006) 1292–1299.
- [33] V. Dubinko and D. Terentyev, Molecular dynamic simulation of localized anharmonic vibrations in metal-hydrogen nanocrystals, to be published.
- [34] D. Woolridge, *Quantum Gravity Research*, Los Angeles, CA 90290, USA, <https://www.dropbox.com/s/557akac5zoynqs/LAV%20animation%20in%20PdH%20cluster.mp4?dl=0>

- [35] N.N. Medvedev, M.D. Starostenkov, P.V. Zakharov and O.V. Pozhydaeva, *J. Tech. Phys. Lett.* **37** (2011) 7.
- [36] D. Letts and P.L. Hagelstein, Stimulation of optical phonons in deuterated palladium, in ICCF-14, *Int. Conf. on Condensed Matter Nucl. Sci.*, Washington, DC, 2008; P.L. Hagelstein, D. Letts and D. Cravens, Terahertz difference frequency response of PDD in two-laser experiments, *J. Condensed Matter Nucl. Sci.* **3** (2010) 59–76.
- [37] Jean-Paul Biberian, Replication attempts of the Parkhomov experiment, *Proc. 11th Int. Workshop on Hydrogen Loaded Metals*, October 15–16, 2015.
- [38] K.P. Budko and A.I. Korshunov, Calorimetric investigation of anomalous heat production in Ni–H systems, *Proc. 11th Int. Workshop on Hydrogen Loaded Metals*, October 15–16, 2015.
- [39] A.G. Parkhomov, Ni–H reactors created after the Lugano Report, *Int. J. of Unconventional Sci.* **11**(4) (2016) 58. <http://www.unconv-science.org/n11/parkhomov/>.
- [40] A.G. Parkhomov, Long-term tests of Ni–H thermal generators in flow calorimeter, *Int. J. Unconventional Sci.* **12,13**(4) (2016) 74. <http://www.unconv-science.org/n12/parkhomov/>.
- [41] V.I. Dubinko, Radiation-induced catalysis of low energy nuclear reactions in solids, *J. Micromechanics and Mol. Phys.* **1** (2016) 165006-1-12.
- [42] V. Dubinko, D. Laptev and K. Irwin, Catalytic mechanism of LENR in quasicrystals based on localized anharmonic vibrations and phasons, presented at *ICCF20*, Sendai, October 2016, to be published in JCMNS.



Research Article

Electron Deep Orbits of the Hydrogen Atom

J.L. Paillet*

Aix-Marseille University, France

A. Meulenberg†

Science for Humanity Trust Inc., USA

Abstract

This work continues our previous works, on electron deep orbits of the hydrogen atom. An introduction shows the importance of the deep orbits of hydrogen (H or D) for research in the LENR domain, and gives some general considerations on the Electron Deep Orbits (EDO) and on other works about deep orbits. A first part recalls the known criticism against the EDO and how we face it. At this occasion we highlight the difference of resolution of these problems between the relativistic Schrödinger equation and the Dirac equation, which leads for this latter, to consider a modified Coulomb potential with finite value inside the nucleus. In the second part, we consider the specific work of Maly and Va'vra on deep orbits as solutions of the Dirac equation, the so-called Deep Dirac Levels (DDLs). As a result of some criticism about the matching conditions at the boundary, we verified their computation, but by using a more complete ansatz for the “inside” solution. We can confirm the approximate size of the mean radii $\langle r \rangle$ of DDL orbits and that $\langle r \rangle$ decreases when the Dirac angular quantum number k increases. This latter finding is a self-consistent result since (as distinct from the atomic-electron orbitals) the binding energy of the DDL electron increases (in absolute value) with k . We observe that the essential element for obtaining deep orbits solutions is special relativity.

© 2017 ISCMNS. All rights reserved. ISSN 2227-3123

Keywords: Deep electron levels, LENR, Relativistic quantum physics, Singular solutions

1. Introduction

For many decades, the question of the existence of electron deep levels or electron deep orbits (EDOs) for the hydrogen atom led to numerous works and debates. Why once more a study on this subject? For several reasons:

- EDOs are predicted by relativistic quantum equations, with mean radius of the orbitals of order femto-meter.
- So, hydrogen atoms (including deuterium) with electron deep orbits (femto-atoms) can facilitate processes of LENR inside condensed matter, the avoidance of nuclear fragmentation in $D-D \Rightarrow {}^4\text{He}$ fusion reactions, and a means of increasing the rate of energy transfer between an excited nucleus and the surrounding lattice.

*Corresponding author. E-mail: jean-luc.paillet@club-internet.fr.

†E-mail: mules333@gmail.com.

- Moreover, femto-atoms could create femto-molecules and combine with lattice nuclei for transmutation without energetic radiations.
- By accepting the reality of a non-singular central potential within a nuclear region, many mathematical arguments against anomalous solutions of the relativistic equations no longer pertain.
- Numerical methods now allow prediction of properties and features of the EDOs.

The statements above for the importance of deep-electron orbits to LENR are factual. However, they convey neither the true criticality of the concept to cold fusion (CF) theory nor the evidence (and publications) to support these statements. The first part of this introduction will attempt to do both for the statements pertaining to CF. The second part of the introduction will be specific to the theme of the paper “validating the relativistic models for the deep orbits”.

It was recognized early in the CF development that the best (perhaps the only) means of fusion at low temperatures and energies was to increase the time that negative charge spends between fusing nuclei. This means of overcoming the Coulomb barrier between nuclei is a continuing theme and is addressed in most models of LENR (see, e.g., “Extensions to physics: what cold fusion teaches,” [1]). The other side of the problem was emphasized in 2013 (by Akito Takahashi at ICCF-15): “even if the Coulomb barrier were to be lowered to zero, D+D fusion would still lead to ^4He -fragmentation products, not to the observed atomic ^4He and heat of CF” This problem is perhaps best addressed by the means and consequences of electron decay to the deep orbits (“Tunneling Beneath the $^4\text{He}^*$ Fragmentation Energy,” [2] and “From the Naught Orbit to ^4He Ground State” [3]).

With the recognition that deep-orbit electrons can explain some of the fundamental problems of cold fusion, a more complete study of the nature and effects of these relativistic electrons was begun (“Deep-electron orbits in Cold Fusion” [4]). An important side issue of this study was the nature of electromagnetic radiation from the deep-orbit electrons and the ability of deep-orbit electrons to transfer energy between an excited nucleus and the lattice (“Deep-Orbit-Electron Radiation Emission in Decay from $^4\text{He}^{*#}$ to ^4He ,” [5]). As confidence grew in the CF results for transmutation in both the PdD and NiH systems, the concept of longer-lived “femto-atoms”, their nature and their consequences, became the subject of analysis (“Femto-atoms and Transmutation” [6] and “Femto-Helium and PdD Transmutation” [7]). These studies led to an understanding of 3-body fusion processes (femto-atom + nucleus) to explain both transmutation without hard radiation and selective radio-isotope remediation.

The least-resolved portion of the deep-orbit electron scenario is why the deep levels are not immediately filled from atomic orbitals and why are they not readily observed? If they are not able to be populated in the natural environment, then how are we to populate these levels. This latter question has been addressed in part by (“Lochon Catalyzed D–D Fusion in Deuterated Palladium in the Solid State” [8], “Composite model for LENR in linear defects of a lattice” [9], and “Pictorial description for LENR in linear defects of a lattice,” [10]).

Since the deep-orbit model can explain all of the observed CF results that have been addressed in the above references (and more, e.g., [11]) and is based on the fundamental equations of relativistic quantum mechanics, it should be readily accepted. However, it has been rejected for over 50 years (perhaps 75 years) for primarily mathematical reasons. It is hoped that, with the cooperation of a mathematician and a physicist in the present authors, the non-physical reasons for rejecting the concept can be eliminated and a firm mathematical base can be laid that would lead to acceptance of both the deep orbits and a theory for cold fusion.

There are, in the literature, various and numerous theoretical methods to define a state of the hydrogen atom with electron deep orbits (EDO). Some authors use the term *hydrino* for denoting the special deep-orbit hydrogen states owing to the work of Mills [12] on the hypothetical existence of H atoms with orbit levels under the Bohr ground level and where the values of orbit radii are fractional values of the Bohr radius. Here we do not use this term, a physical concept specifically attached to the cited work, because it is not deduced from (standard) relativistic quantum equations and does not coincide with the deep level model that we are addressing [13].

With the quantum equations habitually used in the literature for computing the bound states of the H atom, we can note that there is in general a crossroad with a choice of value or a choice of sign for a square root in a parameter. According to which path is chosen, the resolution process leads either to the usual “regular” solution or to an unusual one called an “anomalous” solution; this latter is rejected in the Quantum Mechanics textbooks. Nevertheless, we can note that *every anomalous solution is not necessarily one with EDO*.

Why do we emphasize here the use of *relativistic* quantum equations?

For (at least) two reasons:

- (1) Only the relativistic equations can predict EDOs with mean radius of order femto-meter.

We can even give a simple mathematical reason for this fact. So, for example, one can see that with a non-relativistic Schrödinger equation, one can obtain “anomalous” solutions, but they are not EDOs.

- (2) With an EDO having a mean radius of order femto-meter, the Coulomb potential energy is so high that the electron is necessarily relativistic [14].

Nevertheless, we can note the works of Vigier [15] and Barut [16], then Samsonenko et al. [17], Dragic et al. [18], on possible electron tight orbits under the Bohr level for atom H (or D), and even “tight molecules” with energy of several keV. Most are treated in a non-relativistic framework. These works take into account magnetic interactions such as spin–orbit and spin–spin (electron–nucleus), which at the scale of classical atomic orbitals, have a very weak impact, but will remove level degeneracies. Nevertheless, at distances closer to nucleus, these magnetic interactions can modify the Coulomb potential into a series of inverse-power potentials of the following form, as indicated also in the work of Ozcelik et al. [19]:

$$V(r) = A/r + B/r^2 + C/r^3 + D/r^4. \quad (1)$$

Of course $A < 0$ since the first term corresponds to the Coulomb potential, but if $D > 0$ and $C < 0$, one has a “repulsive core” and a possible deep potential well. The methods of solutions are “semi-numerical” approximations and the authors indicate little information about energy values for atom H: we noted the value 40 keV in [17] as a maximum. The corresponding orbitals are in fact much less deep than the EDOs obtained by the relativistic quantum equations. On the other hand, the considered magnetic interactions should be obviously much stronger for EDOs and could eliminate the question of the singular point of the Coulomb potential and the problems associated with this singular point.

In Figs. 1 and 2, we represent a potential like in Eq. (1) having three zeros, with $B > 0$, $C < 0$, $D > 0$. Of course, the values on the axis have no physical meaning: it is only a simulation.

Finally, concerning the magnetic effects on the Coulomb potential, we can note a very subtle effect due to the “Anomalous Magnetic Moment” of the electron. It can be taken into account in the Dirac equation, under the form of an additional term in inverse-power: $-\mu_a\alpha/r^2$. In fact, it does not directly act on the central potential, but it is added to the non-diagonal terms of the 2×2 matrix representing the radial Dirac operator, Eq. (2). As indicated by Thaller [20,21], it acts as a repulsive interaction that “forces the wavefunction away from the singularity.” So, it also eliminates the problems related to this singularity.

$$D_r = \begin{pmatrix} mc^2 + V(r) & \hbar c \left(-\frac{d}{dr} + \frac{k}{r} \right) - \mu_a \mathbf{V}'(\mathbf{r}) \\ \hbar c \left(\frac{d}{dr} + \frac{k}{r} \right) - \mu_a \mathbf{V}'(\mathbf{r}) & -mc^2 + V(r) \end{pmatrix}. \quad (2)$$

Note the works based on strong magnetic interactions near the nucleus with potential of type (1), presented above in a very superficial way, implicitly suppose a *point-like nucleus*. If small radius electron orbits are expected, special relativity should to be taken into account. Then, a study of this type certainly falls into a relativistic two-body problem

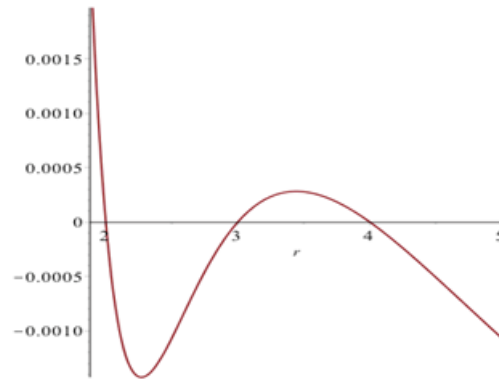


Figure 1. $V(r)$ for $r \leq 5$.

where one faces the “no-interaction theorem of Currie–Jordan–Sudershan” [22]. This should require to use a field-theory interaction for Lorentz-invariant behavior, or, e.g. the two-body Dirac equations of constraint dynamics [23]. Of course, all these would require a specific and deeper analysis, which is not the topic of the present paper. This paper is essentially devoted to the analysis, verification, and extension of the results of Maly & Va’vra [24] on singular solutions of the Dirac equation by considering a potential associated with a *nucleus of finite size*.

2. Arguments against the EDO States

The arguments against the EDO states (assuming a singular $1/r$ Coulomb potential) have been already exposed in detail in [13,14], as well as the possible solutions to resolve these questions. They concern only the radial solutions of the quantum equations and they are the following ones:

- The wavefunction has a singular point at the origin.
- The wavefunction is not “square integrable”.

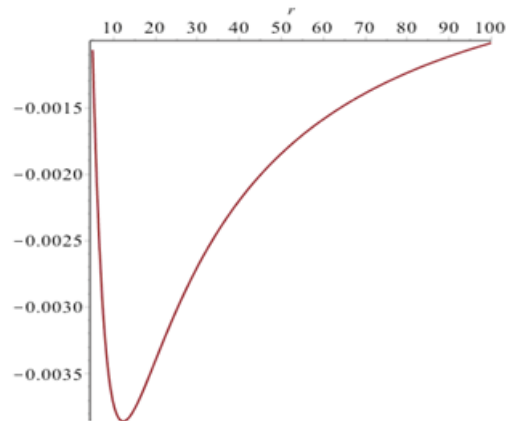


Figure 2. $V(r)$ for $0 \leq r \leq 100$.

- The “orthogonality criterion” cannot be satisfied.

We can note all three problems are related to the singularity of the Coulomb potential at $r = 0$.

- We noted also a fourth question: the strength of the binding seems to increase when the coupling strength decreases.

First, we cope with this fourth question, as it is not related to the singularity of the potential.

2.1. The behavior of the binding energy while the coupling strength decreases

One can consider variations of the coupling strength $\gamma = Z\alpha$, where α is the coupling constant, and to examine the consequence of such variations on atomic orbitals. We can cite, for example, the work of Thaller [21], where properties of the Dirac operator are analyzed, in particular, for heavy atoms ($Z \gg 1$).

It can also be very instructive to make the following “thought experiment”: to imagine variations of the coupling constant α and observe consequences on eigenfunctions of quantum equation. Doing this in [25], Dombey points to a very strange phenomenon concerning the EDO solutions of the Klein–Gordon (K–G) equation: when α decreases and tends towards 0, the binding energy of the electron increases in absolute value and tends towards its maximum. He observes the same phenomenon with the 2-D Dirac equation. To simplify, as in the cited paper, we consider only the “anomalous” solutions of the K–G equation with angular momentum $l = 0$. The expression of the total energy of the electron is the following:

$$E_N = mc^2 \left[1 + \frac{\alpha^2}{\left[N + \frac{1}{2} - \sqrt{\left(\frac{1}{4} - \alpha^2 \right)} \right]^2} \right]^{-1/2}. \quad (3)$$

The deep orbits are obtained only if the radial quantum number $N = 0$. We recall further the general conditions for deep orbits. With $N = 0$, the sub-expression

$$\Delta = N + \frac{1}{2} - \left(\frac{1}{4} - \alpha^2 \right)^{1/2}$$

can be reduced to α^2 and then $E_0 \sim mc^2\alpha$. So, if $\alpha \rightarrow 0$, we have the total energy $E_0 \rightarrow 0$, and this implies that the absolute value of binding energy $|\text{BE}| = mc^2 - E_0 \rightarrow mc^2$, its maximum possible value. In fact, we think this result is obtained in the context of an ill-defined system, uniquely on a pure mathematical basis.

From a physical point of view, we can see the coupling constant α is actually entangled with several fundamental constants, in particular the Planck constant, the velocity of the light, and the elementary electric charge. So, modifying α without caution can certainly lead to paradoxical physical results (e.g., letting α go to zero means that the charge does also; thus, there are no bound states and no BE).

There is another well-known example of changing a physical constant to obtain results: the non-relativistic limit of a relativistic theory can be obtained if one lets c tend to infinity, and thus the relativistic coefficient γ becomes 1 for any speed. However, as noted in [21] if doing this on the Dirac operator in an electro-magnetic field, one has to proceed carefully because of terms as such as mc^2 , which would tend to infinity, and as the term $(e/c) \mathbf{A}$ that would turn off the vector potential \mathbf{A} if c tends to infinity. Then the author is led to develop specific techniques and to define some concepts needed to account for the nature of the so-called *c-dependence* of the Dirac operators.

2.2. The wavefunction can have a singular point at the origin

This argument is rising in all known cases of EDO states with a $1/r$ Coulomb potential. The spatial part of solutions of the radial equation, in the most general form, has several factors:

- One factor is a decreasing exponential such that the wavefunction vanishes when $r \rightarrow +\infty$.
- Another one is $\propto r^s$ with s a real number, due to the Coulomb potential.
- A further one has polynomial form, possibly derived from confluent hyper-geometrical series.

For the solutions called “anomalous”, the exponent s of the factor in r^s is negative, then the radial function $R(r) \rightarrow +\infty$ when $r \rightarrow 0$ and the wavefunction $\psi(r, \theta, \varphi)$ does not obey a boundary condition.

Some authors of EDO solutions remove this trouble by saying that the classical expression of the central potential is a good approximation for the bound state of a single electron atom, but considering the nucleus as a mathematical point is an unphysical abstraction. In fact, the Coulomb approximation in $1/r$ of the central potential generated by the nucleus is suitable only if the electron is not too near the nucleus.

At this point, many authors do not consider a non-singular potential and stop without further development of the anomalous solution. Others work on this subject by expressing corrected potentials in the close vicinity of the nucleus, as e.g. in [24]. We analyze this work in Section 3.

Moreover, we can see below that for the K–G case, the question of singularity can be resolved without modifying the potential.

2.3. The wavefunction can be “not square integrable”

If the wavefunction is not integrable, it cannot be normalized in the entire space. This case results essentially from the behavior of the wavefunction ψ at the origin and not for $r \rightarrow \infty$, thanks to the decreasing exponential. According to the spherical coordinates and the corresponding Jacobian, the norm of ψ is defined by

$$\|\psi(r, \theta, \phi)\| = \int |\psi|^2 \sin \theta r^2 d\theta d\phi dr = \int |Y(\theta, \phi)|^2 d\Omega \int |R(r)|^2 r^2 dr,$$

where Ω is the solid angle. Since the spherical harmonics are normalized, one has only to verify that $\int |R(r)|^2 r^2 dr$ is finite, and this depends only on the behavior of $\int |R(r)|^2 r^2$ at the origin.

Here we can cite the work of Naudts [27], where an EDO state is found by using the K–G equation and the corresponding solution is square integrable. In his paper, the K–G equation has the following form:

$$(i\hbar\partial_t - V)^2 \psi(r, t) + \hbar^2 c^2 \Delta \psi(r, t) = m^2 c^4 \psi(r, t). \quad (4)$$

Historically this equation was called *relativistic Schrödinger equation*.

We can note a time-dependence, because the author derived this equation from the time-dependent Schrödinger equation by introducing the relativistic formulation of the energy. This transformation was described in detail in [14]. We can note also, that the author considers only the case where the angular momentum is null: while expressing the Laplacian Δ in spherical coordinates, he eliminates the term involving the angular momentum operator, $L^2(1/r^2 \hbar^2)$, and so the classical term in $l(l+1)$, representing the eigenvalues of L^2/\hbar^2 , does not occur in his computation. By means of a suitable ansatz, the author finds a regular solution and an “anomalous” one. For this latter one, he obtains an electron total energy $E \sim mc^2 \alpha \sim 3.73$ keV. So the binding energy is $BE \sim mc^2(\alpha - 1) \sim -507.3$ keV. He uses the following ansatz:

$$\psi(t, r) = e^{(i/\hbar)Et} r^{-l} e^{-r/r_0}. \quad (5)$$

Here the parameter denoted as l is not to be confused with angular momentum. As the author looks for solutions satisfying the hypothesis $l < 3/2$ and $r_0 > 0$, the behavior of $|\psi(r, t)|^2 r^2$ at the origin ensures the square integrability of the wavefunction.

On another hand, as the deep orbit state corresponds to the plus sign in the solution

$$l = \frac{1}{2} \left(1 \pm \sqrt{1 - 4\alpha^2} \right),$$

we can see that the origin is a singular point for the wavefunction. Naudts argues against this problem by saying that the nucleus is not a point, but its charge is “smeared” over a distance of about 1fm. Solving the equation with a smeared out Coulomb potential would produce a solution not diverging at the origin, but with certain minor changes on the deep orbit state. We can add that, in the case of heavy nuclei, the regular solutions of the relativistic Schrödinger equation have also a singular point at the origin, because the coupling parameter $\gamma = Z\alpha$ is not “small” (e.g., for atom U, it is equal to ~ 0.45).

Another more subtle criticism concerns the well-known problem of the conservation equation: for the K–G equation, the density ρ is proportional to

$$\frac{\hbar}{2imc^2} (\psi^* \partial_t \psi - \psi \partial_t \psi^*)$$

and cannot be considered as a probability density, because it can be negative [27], but it is interpreted as a charge density if taking into account the electromagnetic field in the conservation equation. Regardless, this question does not remove the interest in the EDO solution found by Naudts, and its square-integrability.

Finally we note two things:

- If the singular point at the origin (in the “Coulomb” potential or the solutions) is suppressed, the wavefunction is automatically square-integrable.
- The square-integrability cannot be obtained for the Dirac equation in a pure Coulomb potential.

This point is quickly proven by Naudts on a simplified form of radial Dirac equations.

2.4. The orthogonality criterion cannot be satisfied

The Hamiltonian, representing the total energy, has to be a Hermitian operator in order for its eigenvalues to be real. This implies the following condition: eigenfunctions corresponding to distinct values have to be orthogonal. In [28], de Castro examines the asymptotical behavior of the solutions of the non-relativistic Schrödinger, of the K–G and of the Dirac equations, as functions of formal variations of the coupling constant α . We note that, for doing this, one could as well consider variations of $Z\alpha$, to cope with heavy nuclei.

He indicates the following conditions to obtain orthogonality:

- For the K–G equation: $(u_k^* (du_{k1}/dr) - u_{k1} (du_k^*/dr)) \rightarrow 0$ when $r \rightarrow 0$, where $u_k(r) = rR(r)$.
- For the Dirac equation, a condition on the components f, g : $(f_k^* g_{k1} - g_k^* f_{k1}) \rightarrow 0$, when $r \rightarrow 0$.

Then he obtains the following result:

Square-integrable solutions of the K–G equation satisfying the orthogonality criterion are such that for $\alpha \leq 1/2$, all the values of l (the angular momentum) are allowed. So, one can say that for the light atoms (including atom H and their isotopes), the orthogonality criterion is satisfied for $l = 0$. On the other hand, for the Dirac case, the author indicates that only the regular solutions for the component functions f, g can satisfy the orthogonality. We can also note several works [29,30] on self-adjoint extension of operators for potentials with singularity. In particular, the first cited work explicitly shows that, for the K–G equation in the case of the pure Coulomb potential, the “singular” solutions satisfy the orthogonality condition and also satisfy the boundary condition: when $r \rightarrow 0$, $\lim u(r) = u(0) = 0$.

2.5. Consequences and recall on the first work of Maly and Va'vra on “DDLs”

With regards to the question above, we can see the Dirac equation has to be distinguished from the K–G equation. So, as all the problems mentioned are related to the singular point of the Coulomb potential, the anomalous solutions of Dirac equation require eliminating the singularity of this potential while considering a nucleus with finite dimension. Moreover, this is a more realistic hypothesis from a physical point of view. This is explained in Section 3.

First, we consider the specific works of Maly and Va'vra in [31] on deep orbits as solutions of the Dirac equation, named Deep Dirac Levels (DDLs), because they present the most complete solution and development available and include an infinite family of DDL solutions. In fact, they define DDL solutions for the electronic orbits of the hydrogen-like atoms, by means of the relativistic Schrödinger equation, and by the Dirac equation. Here we consider only hydrogen atoms. As this work has been already described in detail in [13] and yet more in [14], we focus on the Dirac equation and we recall only the results and the principal points of our analysis.

The Dirac equation was obtained by linearizing the classical relativistic energy–momentum relation $E^2 = \mathbf{p}^2 c^2 + m^2 c^4$ before translating the physical quantities into quantum operators.

So, the “free” Dirac equation has the standard following form:

$$(i\hbar \partial_t + i\hbar c \boldsymbol{\alpha} \cdot \nabla - \beta mc^2) \Psi(t, \mathbf{x}) = 0, \quad (6)$$

where the momentum \mathbf{p} was represented by means of the gradient differential operator and $\boldsymbol{\alpha}$ is the 3-vector of Dirac matrices. The Dirac equation is applied to the atom H and we consider only the bound states of the electron. In these conditions, the electron is subjected to an external electromagnetic field, in the form of the static Coulomb potential generated by a proton, and the potential energy is represented by

$$V = -\frac{e^2}{r} = -\alpha \frac{c\hbar}{r}.$$

Then, the Dirac equation in central Coulomb potential reads:

$$(i\hbar \partial_t + i\hbar c \boldsymbol{\alpha} \cdot \nabla - \beta mc^2 - V) \Psi(t, \mathbf{x}) = 0. \quad (7)$$

2.5.1. Method used by the authors and results

The authors refer to and use the method developed by Schiff [27].

Here is the expression of the total energy of the anomalous solutions for atom H, very similar to the classical one for the regular solutions. The difference is the sign “minus” instead of “plus” between n' and the square root, at the denominator of the internal fraction:

$$E = mc^2 \left[1 + \frac{\alpha^2}{\left[n' - \sqrt{k^2 - \alpha^2} \right]^2} \right]^{-1/2}. \quad (8)$$

In this expression, n' is the radial quantum number and k the specific angular Dirac quantum number.

In fact, the sign “minus” before the square root originates from the parameter $s = \pm (k^2 - \alpha^2)^{1/2}$ which appears during the process of solution of Dirac radial equation system. If $s > 0$, the obtained solutions are the “regular” ones; while, if $s < 0$, one obtains the “anomalous” ones.

The number n' can take any positive integer values 0, 1, 2, ... while k can take any integer value $\neq 0$. But hereafter, as k comes from k^2 occurring in the square root and so is involved everywhere in absolute value, we consider k to be > 0 in the following equations.

We can observe the following facts:

- The deep Dirac orbits levels (DDL) correspond only to the situation $n' = k$.
- Among the other cases, if $k > n'$, the authors indicate that the values correspond to “negative energy” states.
- While if $k < n'$, the values correspond to energy levels similar to the “regular states”.

The authors yield computation results for values of the binding energy $|BE|$ as a function of quantum numbers n' , k and the total quantum number n (denoted by conventional letters corresponding to regular orbitals). We can see that, for $n' = k$, the values of $|BE|$ are greater than 509 keV and, unexpectedly, they increase when $n' = k$ increases.

2.5.2. Analysis of the results

First, we can see there is infinity of DDL states: one for each value of $n' = k$.

The same result is obtained by means of the relativistic Schrödinger equation, where the angular number is l .

- The relation $n' = k$ is very important, since it determines the DDL states.

In fact, it has a simple mathematical explanation. Indeed, we can see that if $n' = k$, the sub-expression D of the total energy E , $D = n' - (k^2 - \alpha^2)^{1/2}$ reads $D = k - (k^2 - \alpha^2)^{1/2}$, D becomes very small since $D \sim \alpha^2/2k$ and $Emc^2\alpha/2k$. Then $|BE| \sim mc^2(1 - \alpha/2k)$ and $|BE|$ is close to the rest mass energy of the electron, 511 keV.

We note a similar relation for the anomalous solutions of the relativistic Schrödinger equation, with an analogous mathematical explanation: the deep orbits appear only if $n' = l$.

Indeed, one has only to look at the concerned expression of the total energy:

$$E = mc^2 \left[1 + \frac{\alpha^2}{\left(n' + \frac{1}{2} - \left[\left(l + \frac{1}{2} \right)^2 - \alpha^2 \right]^{1/2} \right)^2} \right]^{-1/2}. \quad (9)$$

One can see that $n' = l$ implies a drastic reduction of the denominator. This implies $E \sim mc^2\alpha/(2l + 1)$, and thus $|BE| \sim mc^2[1 - \alpha/(2l + 1)]$.

- Moreover, one can see also that *Special Relativity is determining for the existence of EDOs*.

Indeed, the sub-term

$$s = -\frac{1}{2} - \left[\left(l + \frac{1}{2} \right)^2 - \alpha^2 \right]^{1/2}$$

that occurs at the denominator, is in fact a parameter essential for choosing between the anomalous solutions and the regular solutions. It is one root of a quadratic equation, $s(s + 1) - l(l + 1) - \alpha^2 = 0$, which appears when solving the relativistic Schrödinger equation. The other root,

$$s = -\frac{1}{2} + \left[\left(l + \frac{1}{2} \right)^2 - \alpha^2 \right]^{1/2},$$

leads to regular solutions.

Nevertheless, we must emphasize that, in the *non-relativistic case*, a similar quadratic equation, very close to the previous, appears: $s(s + 1) - l(l + 1)$. We can see that in this last case, the solutions no longer contain α^2 and are simple integer numbers: $s = l$ gives the regular case, and $s = -(l + 1)$ the anomalous one. In this latter case, it is no

longer possible to apply the “recipe” that discriminates the EDO from the anomalous solutions, because $n' = l$ would lead to a null denominator in the expression of the energy of anomalous solutions, similar to the expression written above, but without the term α^2 . So, we can say that it is not possible to find EDO in this case.

Now we return to the Dirac solutions, the DDLs, and we consider the relation $|BE| \sim mc^2 (1 - \alpha/2k)$ written above. We can see that $|BE|$ increases when k increases, as observed on the tables of Maly and Va'vra. Of course, it is the same thing in the Schrödinger case. We note that *this progression is opposite to that of the one of the regular states*. By seeing this, one can suppose that the electron orbitals are progressively closer to the nucleus when k increases. This fact is not explicitly mentioned in [31] or in their next work [24], but it can be deduced from a sentence in the latter paper.

Here we prove it by direct computation of the mean radius of the DDL orbital, as explained in Section 3, devoted to our work on [24].

- To understand why the case $k > n'$ corresponds to negative energy states (compatible with Dirac equation), it is necessary to know the process of solving the radial equation. In fact, this can be deduced from the following relation (23) in [3], or [28], p. 486: $2\alpha(s + n') = 2E\gamma/\hbar c$. So E has the sign of $(s + n')$, and as $s < 0$, we have $s + n' \sim n' - k + (\alpha^2/2k) \leq -1 + (\alpha^2/2k) \sim -1$, since $k > n'$ and $\alpha^2/2k$ is very small.
- When $k < n'$, one can observe from the algebraic expression of E above, that for any couple (n', k) satisfying this inequality, E is very close to the energy of a *regular level* corresponding to a value of the principal quantum number N taken equal to $n' - k$.

We called these states, “pseudo-regular” states, because the levels correspond to regular levels, while the wavefunctions have the form of anomalous solutions, since they are determined by a negative parameter s .

3. The Deep Orbits (DDL) Obtained as Solutions of the Dirac Equation with a Corrected Potential Near the Nucleus

After their first paper [31] on the computation of the DDL levels, the authors continued their study with a second paper [24] on the solutions of Dirac equation for hydrogen-like atoms, where they consider that the nucleus is not point-like and the Coulomb potential inside the nucleus is finite at $r = 0$.

For doing this, they start with another method ([32], p.195) for the Dirac equation solution, than the one of Schiff [27] used in the first paper. As usual, the solution of Dirac equation can be represented, in central field, by a 4-D vector with two 2-D components, and each component is the product of one radial function with a 2-D spherical spinor.

Then the process of separating the variables leads in general to a system of coupled first order differential equations on both radial functions $f(r)$ and $g(r)$. The exact form of this equation system is dependent on some choices made in the variable separation process, but these different forms are very similar. Here is the system used in [32], where j is the angular quantum number corresponding to the total angular momentum \mathbf{J} operator, sum of the orbital momentum and the spin:

$$\begin{aligned} g' + \frac{j + \frac{3}{2}}{r}g - i\frac{E - V(r) - mc^2}{\hbar c}f &= 0, \\ f' - \frac{j - \frac{1}{2}}{r}f - i\frac{E - V(r) + mc^2}{\hbar c}g &= 0. \end{aligned} \quad (10)$$

One can replace j by putting $k = j + 1/2$.

In the method of solution of Fluegge (p.195), the equation system is transformed into a 2-D order differential equation, a Kummer's equation. The general solutions of this equation take the following form, with confluent hyper-

geometrical series requiring suitable convergence conditions:

$$\begin{aligned} g &= \frac{1}{2} C r^{s-1} e^{-r/a} \left\{ {}_1F_1 \left(s+p, 2s+1; 2\frac{r}{a} \right) - \frac{s+p}{k+q} {}_1F_1 \left(s+p+1, 2s+1; 2\frac{r}{a} \right) \right\}, \\ f &= -\frac{i}{2\mu} C r^{s-1} e^{-r/a} \left\{ {}_1F_1 \left(s+p, 2s+1; 2\frac{r}{a} \right) + \frac{s+p}{k+q} {}_1F_1 \left(s+p+1, 2s+1; 2\frac{r}{a} \right) \right\}. \end{aligned} \quad (11)$$

Here, ${}_1F_1$ is a classical notation for a precise class of hypergeometric series [33].

The parameters a , μ are usual parameters including the energy E , p and q are defined by means of μ . These parameter are used to simplify the writing and to have equations with pure numerical variables. It is unnecessary to write out their expression, because our discussion will focus on the solutions “inside” the nucleus. The parameter s is determined by means of the equation system, for $r \rightarrow 0$, that gives $s = \pm(k^2 - \beta^2)^{1/2}$ where $\beta = Z\alpha$ and α is the coupling constant. Note that the expressions of f and g depend on k and s . We know that DDL solutions result when a negative s is chosen.

3.1. Determining the solutions inside the nucleus

3.1.1. The matching radius and the continuity condition

While considering the nucleus has finite dimension, the authors choose a finite specific potential inside the nucleus and then look for the wavefunctions inside the nucleus. The chosen potential is derived (by adding a constant β_0) from the Smith–Johnson potential, corresponding to a uniformly distributed spherical charge, whose expression is the following:

$$V(r) = - \left[\frac{3}{2} - \frac{1}{2} \left(\frac{r^2}{R_0^2} \right) \right] \frac{Ze^2}{R_0} + \beta_0. \quad (12)$$

In fact, we consider β_0 has to be null since, in the case $\beta_0 \neq 0$ the total potential from 0 to $+\infty$, built by connecting it with the Coulomb potential, would be discontinuous at $r = R_0$. R_0 is the “matching” radius, i.e. a radius near the nucleus such that the following rules are applied:

- For $r < R_0$, the potential is $V(r)$ and the wave-functions solutions are the “inside” ones, noted f_i and g_i . Here we consider $Z = 1$ (for hydrogen atom).
- For $r > R_0$, the potential is the standard Coulomb potential and the wavefunctions solutions are the “outside” ones, f_o and g_o , as noted.
- The inside and outside solutions have to verify the continuity condition, i.e. $g_i(R_0) = g_o(R_0)$ and $f_i(R_0) = f_o(R_0)$. This condition is sufficient, because the Dirac equation is first order differential in the space coordinates.

As a result of some criticism about the matching conditions at the boundary, we thought that it was necessary to verify the method and the results of the computation indicated in [24].

First, there is the question of the choice of R_0 . As this value is not explicitly given in their paper, we chose the value $R_0 = 1.2$ fm as in the work of Deck et al. [34], where the authors use the formula $R_0 = 1.2 A^{1/3}$, A being the mass number. In Fig. 2 in [24], representing the curve of the Electron Density of a DDL atom H for $k = 1$, one can estimate that the peak is at a value of the radius slightly >1 F but <1.2 F. The authors say that this peak corresponds to the nucleus radius. One will observe that it corresponds to the value of the matching radius (see results in Section 3.2.1). In fact, one has to choose a value of R_0 close of the charge radius R_c of the nucleus but slightly greater than R_c : one supposes that in the close neighborhood of the nucleus, the strength of the electric field no longer

increases. So, for atom H, as the proton has $R_c \sim 0.875$ F in CODATA 2014 [35] or in [36], one can reasonably choose $1\text{F} < R_0 < 1.25$ F.

We have performed the computation particularly for atomic H, but if we consider atomic D, the previous empirical formula would give $R_c \sim 1.51$ F. Nevertheless, in modern tables cited above, we can see that $R_c \sim 2.14$ F, so we could choose $2.26\text{F} < R_0 < 2.5$ F. We will see further how the results change when we modify the matching radius R_0 .

3.1.2. Ansatz used for finding the “inside” solutions

The choice of an ansatz is a very important element for finding the solutions f_i and g_i of the initial system of radial equations. Moreover, its expression is determined to satisfy the continuity condition.

In their paper [4], the authors put solutions in the following form:

$$\begin{aligned} g_i &= Ar^{S_i-1}G_2(r), \\ f_i &= iBr^{S_i-1}F_2(r), \end{aligned} \quad (13)$$

where $G_2(r)$ and $F_2(r)$ are power series, i.e.

$$G_2(r) = a_1r + a_2r^2 + a_3r^3 + \dots \quad \text{and} \quad F_2(r) = b_1r + b_2r^2 + b_3r^3 + \dots \quad (14)$$

We note that one can eliminate the imaginary number “ i ” coefficient from the definition of the inside function f_i as from the outside function f_o , by posing $f_{o1} = -if_o$ and $f_{i1} = -if_i$ in the equation system.

We consider from here, that f_i and f_o no longer contain “ i ” in their respective coefficients. Next the equation system leads to couples of interdependent recurrent formulas for computing the coefficients of both power series $G_2(r)$ and $F_2(r)$. As usual, one has to annul the coefficients of the successive powers of r in the unfolded polynomials. But it seems that the information given in the paper is incomplete, because when unfolding both recurrence relations ([24], p. 61), the coefficient A automatically disappears and the polynomials $G_2(r)$, $F_2(r)$, take the following forms $G_2(r) = Bb_1 G(r,k)$, $F_2(r) = Bb_1 F(r,k)$, where $G(r,k)$ and $F(r,k)$ are expressions depending only on the radius r and the quantum number k . Then, when trying to satisfy the continuity condition with the couple of equations $\{g_i(R_0) = g_o(R_0), f_i(R_0) = f_o(R_0)\}$, and taking into account that these equations have to be satisfied for any *fixed* value of k , one gets a couple of linear equations in the form $\{G_i = KG_o, F_i = K F_o\}$ where $K = C/Bb_1$ is the only unknown and G_i, G_o, F_i, F_o are four constants $\neq 0$ and such that $G_i/G_o \neq F_i/F_o$. Of course, this system has no solution.

We think that useful information was in another paper of the same authors, referenced as “to be published” but which unfortunately was not published. In fact, the disappearance of A is due to the starting couple of recurrent relations:

$$\{(k + s_i + 1)a_1A = 0, (-k + s_i + 1)b_1B = 0\}. \quad (15)$$

This leads to two possible choices for having convergence at $r = 0$:

for $k < 0$, $s_i = -k - 1$, $b_1 = 0$ and $a_1 \neq 0$, which leads to the disappearance of B
or for $k > 0$, $s_i = k - 1$, $a_1 = 0$ and $b_1 \neq 0$, which leads to the disappearance of A .

To resolve this problem, the only solution is to add a further parameter in the power series, in such a way that it could not be merged with the multiplicative coefficient B (choice $k > 0$). For doing this, we consider the following more complex power series for $G_2(r)$ and $F_2(r)$:

$$G_2(r) = a_1(\lambda r) + a_2(\lambda r)^2 + a_3(\lambda r)^3 + \dots \quad \text{and} \quad F_2(r) = b_1(\lambda r) + b_2(\lambda r)^2 + b_3(\lambda r)^3 + \dots$$

Of course, one must not confuse this change with a scale change for r , because r remains the only variable for derivative in the differential Dirac equations, and the recurrence relations are rather similar to the ones of [24] but including the parameter λ in a simple way. They have the following form:

$$\begin{aligned} a_n(\lambda(s_i + k + n)) &= (B/A)(K_1 b_{n-1} + (\beta_2 b_{n-3})/\lambda), \\ b_n(\lambda(s_i - k + n)) &= (A/B)(K_2 a_{n-1} - (\beta_2 a_{n-3})/\lambda), \end{aligned} \quad (16)$$

where K_1 and K_2 are parameters depending on the (total) energy E and on constant parameters β_1, β_2 used to write the expression of the potential inside the nucleus:

$$V = \hbar c (-\beta_1 + \beta_2 r^2). \quad (17)$$

We unfold the recurrent relations with the choice $k > 0$, and we obtain the expressions of g_i and f_i in the form of two polynomials in λ and r . As indicated by the authors, we can limit the maximum powers to 6 (5 in their paper) in the initial polynomials $G_2(r)$ and $F_2(r)$, since $r < R_0$ is very small and one can neglect higher order terms. The progression of powers with k is the following:

- For $k = 1$, the polynomial f_i has degree 4 in r and includes only even power terms while g_i has degree 5 in r and includes only odd power terms.
- When k changes into $k + 1$, the degrees in r increase by 1 and the parities of the power terms occurring in the respective polynomials alternate.
- But, for any k , the maximal degree of λ remains constant and equal to 2.

More precisely, for any fixed $r > 0$, g_i and f_i can always be factorized into the form $(a\lambda + b)\lambda$. This form is very useful because it always ensures a solution of the matching problem for the inside and outside wavefunctions at $r = R_0$. Indeed, the equations of continuity condition $\{g_i(R_0) = g_o(R_0), f_i(R_0) = f_o(R_0)\}$ lead to a couple of pseudo-quadratic equations with two unknowns λ and C (the multiplicative coefficient common to both outside wave-functions) in the following form, where the coefficients a, b, a', b', c, c' (depending on k and on R_0) are always $\neq 0$ and are taken > 0 :

$$\begin{aligned} (a\lambda - b)\lambda - cC &= 0 \\ (a'\lambda + b')\lambda + c'C &= 0. \end{aligned} \quad (18)$$

This system is reducible into two linear equations. A plus sign occurs before c' because f_o is always a negative function while g_o is a positive one. Moreover, a minus sign occurs before b , and we have $c \gg c'$ and $b' \gg b$: this can be showed by recurrence on k . In these conditions, we have $ac' + a'c \neq 0$ and $bc' - b'c \neq 0$, what allows to obtain $\lambda \neq 0$, then $C \neq 0$ by a similar reasoning. So, the system has a non-trivial solution which can be used (apart from the trivial solution $\lambda = C = 0$).

3.1.3. The question of orthogonality and the boundary condition

If we consider a couple of “inside” functions (g_i, f_i) , the term of minimal degree of the polynomial g_i is k and for f_i it is $k - 1$. So, in the formula used to verify the *orthogonality criterion* (Section 2.4), when $(f_k^* g_{k+1} - f_{k+1} g_k^*) \rightarrow 0$ when $r \rightarrow 0$, the expression to be considered is a polynomial P having a term of minimal degree $k + k_1 - 1$ and thus, for any $k > 0$, P does not contain any constant term. We can deduce that *the corresponding global solution satisfies the orthogonality condition*.

Next, if we look at the boundary conditions, expressed by $g_i \rightarrow 0$ and $f_i \rightarrow 0$ when $r \rightarrow 0$, we can see this property is verified for any $k > 1$.

3.2. Results obtained by computing the wavefunctions and consequences

While having the expressions of the couple of whole wave-functions from $r = 0$ to $+\infty$, built by connecting g_i to g_o and f_i to f_o , one can obtain important information on the electron orbital.

As in the cited work, we use the Electron Density (EID) expression, which is the *radial probability density* defined by the wavefunctions, for computing the normalization constant and next to compute the mean radius $\langle r \rangle$ of the orbital for different values of the quantum number k . We would like obtain a formal expression of $\langle r \rangle$ as function of k . Unfortunately the expressions of the wavefunctions are very cumbersome, especially the expression for the outside functions including hyper-geometrical series. Furthermore, the last step is an integral. Nevertheless, while numerically computing $\langle r \rangle$ for several progressive values of k , one can observe the corresponding progression of $\langle r \rangle$ and even estimate the limit for very great k . Moreover, by modifying different parameters, such as the value of the matching radius, the degree of the initial polynomial of the ansatz, or the form of the nuclear potential, one can observe if and how changes in these parameters affect the orbitals, and thereby deduce a kind of “mathematical stability” of the orbitals.

3.2.1. Values of the mean radius, with matching radius $R_0 = 1.2 F$ and for different values of k

The value of the mean radius is an essential parameter for the LENR, since the range of the strong nuclear force is order of femto-meters (fm or F) and quickly decreases at distances $> \sim 3-5 F$. The mean radius of electron orbital determines the “size” of the atom and the value of the repulsive radius of an atom. This radius can be estimated approximately [4] to the value of r where EID drops to 1/10 of its peak value.

The computation process is the following:

- For given k , to compute the functions g_i, g_o, f_i, f_o .
- Next to compute the parameters, λ and C for satisfying the continuity condition, as described above.
- To insert the value of λ into the previous expressions of g_i, f_i and replace the parameter C by its value into the expressions of g_o, f_o .
- To consider the Electron Density of the “outside” functions $\text{ElDo} = 4\pi r^2(|f_o|^2 + |g_o|^2)$ and the EID of the “inside” functions $\text{ElDi} = 4\pi r^2(|f_i|^2 + |g_i|^2)$, and to compute the normalization constant N with the following formula:

$$1/N = \left[\int_0^{R_0} \text{ElDi} \, dr + \int_{R_0}^{+\infty} \text{ElDo} \, dr \right]. \quad (19)$$

- Finally, to compute the mean radius with the following formula:

$$\langle r \rangle = N \left[\int_0^{R_0} r \, \text{ElDi} \, dr + \int_{R_0}^{+\infty} r \, \text{ElDo} \, dr \right]. \quad (20)$$

Doing this, we obtained the following values:

- $k = 1$, $\langle r \rangle \sim 6.62 F$,
- $k = 2$, $\langle r \rangle \sim 1.65 F$,
- $k = 3$, $\langle r \rangle \sim 1.39 F$,
- $k = 10$, $\langle r \rangle \sim 1.226 F$,

- $k = 20$, $\langle r \rangle \sim 1.207$ F.

- (1) As a first consequence of this result, we observe that we obtain values of *the same size order* as those in [24], while we used *a method which is likely different* (for computing the inside functions). So, we have a good confirmation of the prior results. Those authors indicate explicitly the value 5.2 F for the DDL atom H for $k = 1$ and their matching radius seems to be slightly >1 F but <1.2 F. They say further, “The main point of this section is that the size of atoms with all electrons on the DDL levels can be very small. Under some conditions ($l > 10$) such atoms (H) with all electrons on the DDLs might participate in the secondary nuclear reactions,” to be related to a previous phrase: “it is well known that the short-range nuclear forces are acting at a distance of 3–5 F.”
- (2) With our computation results, we can see *the mean radius decreases when k increases*. This was suggested by those authors (by the cited phrase above) and it is consistent with the fact that the binding energy in absolute value $|BE|$ increases when k increases [13].
- (3) Finally, we can see also that, after an abrupt fall at the beginning of the progression, the value of the radius asymptotically tends to the value of the matching radius 1.2 F. In Fig. 3, we plot the curves of the normalized EID for $k = 1, 2$, and 3.

3.2.2. Values of the mean radius, obtained when increasing the precision of the inside functions

Now we give results obtained when starting from polynomials $G_2(r)$ and $F_2(r)$ until degree 8. Of course, the method of computation is the same, but this time the polynomials g_i, f_i have degree 3 in λ . But for any fixed $r > 0$, they can always be factorized into the form $(a\lambda^2 + b\lambda + c)\lambda$.

The verification of the continuity condition leads to a couple of equations of the following form, where the coefficients $a, b, c, d, a', b', c', d'$ are $\neq 0$ and are taken > 0 :

$$\begin{aligned} (a\lambda^2 + b\lambda - c)\lambda - dC &= 0, \\ (a'\lambda^2 + b'\lambda + c')\lambda + d'C &= 0. \end{aligned} \quad (21)$$

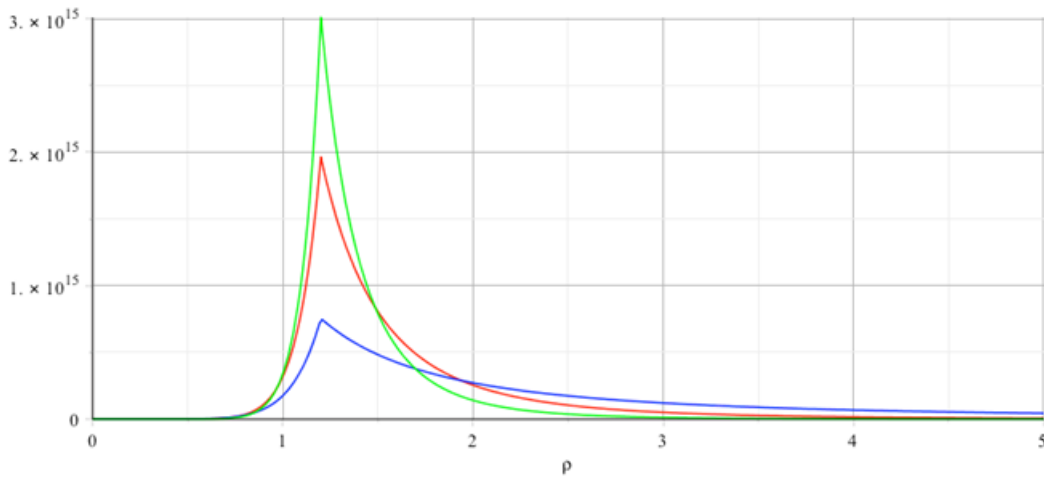


Figure 3. Normalized EID, for $k = 1$ (blue), $k = 2$ (red) and $k = 3$ (green). The radius ρ is in F.

This system can be reduced into a quadratic equation and a linear equation. To rigorously prove it has always a (non-trivial) solution is rather tedious. In fact one has to choose between two solutions very near in absolute value, but with roots λ of opposed signs.

In any case, the values computed for the mean radius are:

- $k = 1$, $\langle r \rangle \sim 5.91 \text{ F}$,
- $k = 2$, $\langle r \rangle \sim 1.51 \text{ F}$,
- $k = 3$, $\langle r \rangle \sim 1.305 \text{ F}$,
- $k = 10$, $\langle r \rangle \sim 1.204 \text{ F}$.

One can observe that the values are slightly smaller than the ones obtained with polynomials of degree 6, but the absolute and relative shifts are monotonically smaller with k increasing

- $k = 1$, $\Delta \langle r \rangle \sim -0.7 \text{ F}$, $\Delta \langle r \rangle / r \sim -0.10$,
- $k = 2$, $\Delta \langle r \rangle \sim -0.14 \text{ F}$, $\Delta \langle r \rangle / r \sim -0.08$,
- $k = 3$, $\Delta \langle r \rangle \sim -0.085 \text{ F}$, $\Delta \langle r \rangle / r \sim -0.06$,
- $k = 10$, $\Delta \langle r \rangle \sim -0.022 \text{ F}$, $\Delta \langle r \rangle / r \sim -0.017$.

Thus, the new series of values converges to the previous one, and one can reasonably assume that both series of values converge to the same limit, the matching radius $\sim 1.2 \text{ F}$

3.2.3. Values of the mean radius obtained when modifying the value of the matching radius

To see what happens if we change the value of matching radius, we recalculate the mean radius for a value distinctly smaller than 1.2 F , by letting $R_0 = 0.78 \text{ F}$. As above, the values of the mean radius become smaller (with increasing k) and tend to 0.78 F . So we obtain the following values:

- $k = 1$, $\langle r \rangle \sim 4.6 \text{ F}$,
- $k = 2$, $\langle r \rangle \sim 1.07 \text{ F}$,
- $k = 3$, $\langle r \rangle \sim 0.9 \text{ F}$,
- $k = 10$, $\langle r \rangle \sim 0.797 \text{ F}$.

Of course, this was only an abstract exercise since this value of $R_0 = 0.78 \text{ F}$ is unrealistic, from a physical point of view, for atomic H (but it is perhaps not unrealistic if a DDL electron is present). On the other hand, if we consider a nucleus heavier than of H, as e.g. ${}^6\text{Li}$, the mean radius will be greater. So, as for ${}^6\text{Li}$ we have $R_c \sim 2.59$, we can reasonably choose, e.g. $R_0 = 2.8 \text{ F}$. With this value for R_0 , the computation yields the following results confirming our model:

- $k = 1$, $\langle r \rangle \sim 13.4 \text{ F}$,
- $k = 2$, $\langle r \rangle \sim 3.84 \text{ F}$,
- $k = 3$, $\langle r \rangle \sim 3.25 \text{ F}$,
- $k = 4$, $\langle r \rangle \sim 3.06 \text{ F}$,
- $k = 10$, $\langle r \rangle \sim 2.85 \text{ F}$.

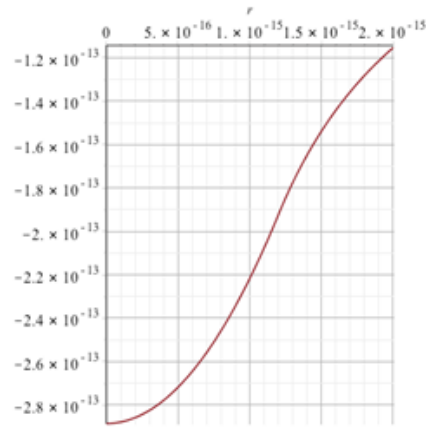


Figure 4. Pot(r) on interval $[0 F, 2 F]$.

3.2.4. Values obtained by changing the nuclear potential

Until now, we performed our computations while considering that the potential corresponds to a uniformly distributed spherical charge. Its expression is the following:

$$V(r) = - \left[\frac{3}{2} - \frac{1}{2} \left(\frac{r^2}{R_0^2} \right) \right] \frac{Ze^2}{R_0} \quad \text{with } Z=1. \quad (22)$$

This potential was introduced into the “inside” functions f_i, g_i by means of the following formula:

$$V(r) = \hbar c (-\beta_1 + \beta_2 r^2), \quad \text{where } \beta_1 = \left(\frac{3}{2} \right) \alpha / R_0 \quad \text{and} \quad \beta_2 = \left(\frac{1}{2} \right) \alpha / R_0^3. \quad (23)$$

Now we consider a further parameter $\varepsilon \geq 0$ and we put $\beta'_1 = ((2+\varepsilon)/2) \alpha / R_0$ and $\beta'_2 = (\varepsilon/2) \alpha / R_0^3$.

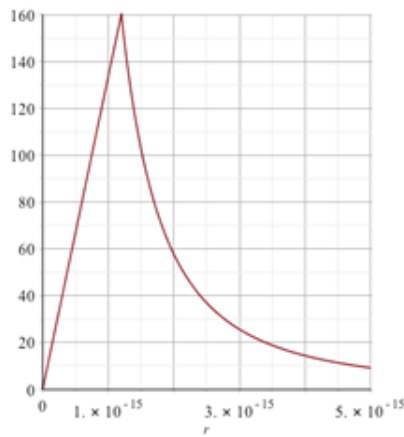


Figure 5. Derivative of Pot(r).

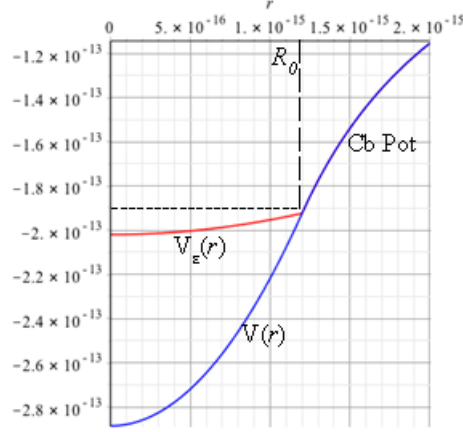


Figure 6. $\text{Pot}(r)$ and $\text{Pot}_\varepsilon(r)$ with $\varepsilon = 10^{-1}$.

We can see that

- If $\varepsilon = 1$, we obtain the previous potential $V(r)$.
- If $\varepsilon = 0$, we obtain a constant potential, equal to the value of the Coulomb potential at $r = R_0$.
- If ε has a very small value, the potential is almost constant, but it is more realistic from a physical point of view than a strictly constant potential.

We plot (Fig. 4) the previous form of potential defined from 0 to $+\infty$ by the following expression:

$$\text{Pot}(r): \{\text{if } r < R_0 \text{ then } \text{Pot}(r) = V(r), \text{ if } r \geq R_0 \text{ then } \text{Pot}(r) = \alpha c \hbar / r\}.$$

Also we plot (Fig. 5) the curve of the derivative $dP(r)/dr$.

In Fig. 4, we can observe the inflection point at $r = 1.2$ F (the matching radius). The derivative (Fig. 5) is continuous, but the second order derivative is discontinuous at the inflection point

Now, we consider the modified nuclear potential

$$V_\varepsilon(r) = \hbar c (-\beta'_1 + \beta'_2 r^2)$$

and the potential Pot defined by the following expression:

$$\text{Pot}_\varepsilon(r) = \{\text{if } r < R_0 \text{ then } \text{Pot}_\varepsilon(r) = V_\varepsilon(r) \text{ if } r \geq R_0 \text{ then } \text{Pot}_\varepsilon(r) = \alpha c \hbar / r\}.$$

We plot this potential in Fig. 6, by taking $\varepsilon = 10^{-1}$ to better see its slight curvature and the previous potential $\text{Pot}(r)$. In Fig. 7, we plot only $\text{Pot}_\varepsilon(r)$ with $\varepsilon = 10^{-5}$

Of course, in Fig. 6, both curves are merged for $r > R_0$. In Fig. 7, we can see that, with very small $\varepsilon = 10^{-5}$, the curve is practically flat for $r < R_0$ and the potential is almost constant. Using the flexible potential Pot_ε , instead of directly using a constant potential, has two advantages: we can easily try intermediate forms of potential and, with a very small ε , we obtain an almost constant potential.

The results with Pot_ε are the following:

- $k = 1$, $\langle r \rangle \sim 6.62$ F,
- $k = 2$, $\langle r \rangle \sim 1.65$ F,

- $k = 3$, $\langle r \rangle \sim 1.39$ F,
- $k = 10$, $\langle r \rangle \sim 1.226$ F,
- $k = 20$, $\langle r \rangle \sim 1.207$ F.

We observe the same results as with the initial potential $\text{Pot}(r)$. Thus, the mean radius is insensitive to the internal potential, but strongly dependent on the choice for matching radius. While this choice appears arbitrary, it may be uniquely determined by the Dirac equations solutions. This is future work.

4. Trying a Process for Increasing the Dependence of the Inside Solutions on the Nuclear Potential

Finally, on account of a subtle criticism [34] about some lack of dependence of the solutions on the nuclear potential, we began to try a special resolution process.

In fact the outside functions are fully dependent on the Coulomb potential. But the inside functions are not very dependent on the nuclear potential $V(r)$, because they involve DDL energy value E included in the energy parameters K_1 and K_2 in the recurrent relations (16) used to define the inside functions.

Indeed, we have $K_1 = [(mc^2 - E)/\hbar c] - \beta_1$ and $K_2 = [(mc^2 + E)/\hbar c] + \beta_1$, where β_1 is a coefficient included in the definition of the nuclear potential $V(r) = \hbar c (-\beta_1 + \beta_2 r^2)$, while the second coefficient β_2 is included in the recurrent relations (16). The general expression of the inside functions depends on $V(r)$, but it depends also on E and thus on the Coulomb potential. So, it depends both on $V(r)$ and on the Coulomb potential.

In these conditions, we first do the following computation:

For fixed k and for a given value of the mean radius $\langle r \rangle$ computed as previously, we compute an approximate mean value of the binding energy, by using the relativistic formulas of the potential energy (in absolute value) $E_{\text{pot}} = -\gamma m v^2$, the one of the kinetic energy $\text{KE} = (\gamma - 1)mc^2$, and by supposing that E_{pot} is equal to the Coulomb potential energy, since the electron is outside the nucleus; next we compute the total energy $E' = mc^2 + \text{KE} - |E_{\text{pot}}|$. Doing this, we find that $E' \neq E$.

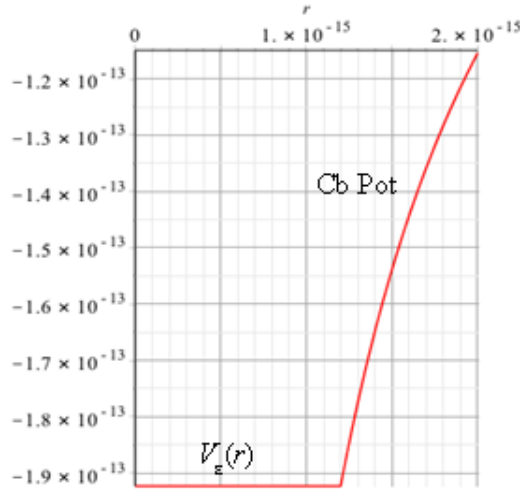


Figure 7. $\text{Pot}_\varepsilon(r)$ with $\varepsilon = 10^{-5}$.

Then we try the following computation process, for “injecting more dependence” on the nuclear potential into the computation of the solutions:

- to “inject” E' in the global solution $(g_i U f_i, g_o U f_o)$ by replacing E by E' in all the energy parameters of the radial equations,
- to compute the new mean radius $\langle r' \rangle$, by using the process described in Section 3.2.1.
- if $\langle r' \rangle \sim \langle r \rangle$ to three digits, then we stop the process, else we iterate it.

Doing this, we obtain a surprising result: for any fixed $k > 1$, the process can stop after a single cycle.

We list the following values of the binding energy (in absolute value) as function of k , corresponding to the values of the mean radius $\langle r \rangle$ and computed as indicated above:

- $k = 2, 275 \text{ keV}$, for $\langle r \rangle = 1.65 \text{ F}$,
- $k = 3, 301 \text{ keV}$, for $\langle r \rangle = 1.39 \text{ F}$,
- $k = 10, 320 \text{ keV}$, for $\langle r \rangle = 1.22 \text{ F}$.

As $\langle r \rangle$ tends to 1.2 F when k tends to $+\infty$, we can suppose that $|\text{BE}|$ tends to a value $\sim 323 \text{ keV}$.

On account of these results, we *conjecture that these values are the actual values of the DDL binding energy for the corrected potential*, instead of the values given by formula (8), which are greater than 509 keV .

For the case of $k = 1$, as $\langle r \rangle = 6.62 \text{ F}$, we have an important gap, in comparison with the values for $k > 1$.

So, the computation process does not converge at the first cycle, but the values of the radius computed at the successive cycles seem to approximately have the behavior of geometrical series, and to converge to a value $\sim 12 \text{ F}$, that would give $|\text{BE}| \sim 56.5 \text{ keV}$.

5. Conclusion about the New Results, Open Questions, Future Paths

The direct computations of the mean radii of the DDL orbitals yield the following results:

- First, we have an important result about the behavior of the orbitals as function of the angular quantum number k , which for the DDLs is equal to the radial number usually denoted by n' :

When k (and thus n') increases, the mean radius $\langle r \rangle$ decreases, which behavior is inverse of the classical orbitals. But this result is totally consistent with the fact that the binding energy $|\text{BE}|$ increases in absolute value when k increases, or equivalently that the total energy E decreases when k increases: this result was already noted in [13] and can be deduced from the tables of [31]. We can also observe it by noting that the $E \sim mc^2(\alpha/2k)$. A possible reason for this “inversion” is that only the deep orbits “see” the repulsive barrier, imposed by centrifugal forces at small r , as significant.

- Next, we can see that the value of $\langle r \rangle$ asymptotically tends to a finite value $\neq 0$, and more precisely it tends to the value of the matching radius R_0 . So, the orbitals converge when k increases and they accumulate in a spherical shell of radius $r_{\text{limit}} \sim R_0$ and $r_{\text{limit}} > R_0$. We can deduce that, for large values of k , the orbitals are no longer distinguishable. On the other hand, as this limit depends on the chosen matching radius, one could say that the determination of the orbitals depends on arbitrary elements. Nevertheless we can argue that the matching radius cannot be arbitrary, as highlighted in Section 3.1.1: one has to choose a value of R_0 close of the charge radius R_c of the nucleus, but slightly greater than R_c . As we do not yet know a more precise criterion for this choice, there remains some degree of incertitude as is usual in Quantum Mechanics.

- Finally, apart from the dependence on the matching radius, which is expected from a physical point of view, the values of the mean radius and especially their asymptotic behavior, seem rather independent of the precision of the functions inside the nucleus and of the chosen nuclear potential.

Open questions about the DDL orbitals include, in particular, the following ones:

- Is there really coherence between the energies of the DDL levels and the values of mean radius as herein computed for the orbitals? For resolving this question, we are presently working on a convergence method, starting from the value of DDL levels energies and inputting some dependence on R_0 and the nuclear potential into the computation, in order to reach energy values consistent with the corrected potential.
- What are the shapes of these orbitals?
- In principle, their angular part should correspond to the classical spherical harmonics, as solution for the 2-D spherical spinors. The condition $k = n'$ could also give an indication for this question. Nevertheless, we can note that the radial wavefunctions of the DDLs have a behavior completely different from the classical atomic orbitals. For example, these latter ones have a number of zeros (radial nodes) equal to n' , while the former ones have no radial node. So the question is: have the angular solutions associated with the DDLs a number of nodal planes corresponding to k ?
- In the same vein, we can ask if the angular momentum is actually increasing with k , as it is the case in the regular solutions. But, as the progression of the DDL mean radii is the reverse of the one of the regular solution, has this reverse progression an influence on the progression of the angular momentum? According to the fact the DDL radii approach a limit, where they accumulate in a very small volume, and on account of the Heisenberg uncertainty relation, can we suppose that the angular momentum vector fluctuates in all directions for large k , so that the time-integrated orbitals could be spherical.
- Concerning the condition $k = n'$, which mathematically determines the DDL states among the anomalous solutions, the question remains to confirm the physical reason this relation yields the DDL states.
- How can we interpret the theoretical existence of pseudo-regular solutions deduced from the relation $k < n'$ (see Section 2.5.2.), i.e. wavefunctions corresponding to a negative s , but with energy values close to “regular” ones?
- Special relativity seems decisive for finding DDLs solutions. Why?
- DDLs are in an extreme EM field. Can we expect a strengthening of special known effects?

Concerning the determination of the Dirac wavefunctions in a modified Coulomb potential without singularity, the best method could be a direct numerical computation of eigenfunctions of the Dirac operator with this potential. Because of the very great difficulty of such a computation method, we can rather envisage various semi-numerical and perturbation methods taking into account some magnetic properties like the ones indicated at the end of the introduction, which also suppose a repulsive core near the origin.

Acknowledgements

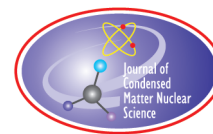
This work is supported in part by HiPi Consulting, New Market, MD, USA; by the Science for Humanity Trust, Bangalore, India; and by the Science for Humanity Trust Inc., Tucker, GA, USA. The authors would like to thank the reviewer for his judicious advices allowing us to improve the comprehension of our work.

References

- [1] A. Meulenberg, Extensions to physics: what cold fusion teaches, *Special Section: Low Energy Nuclear Reactions*, Sect., M. Srinivasan and A. Meulenberg (Eds.), *Current Sci.* **108**(4) 25 Feb. 2015;

- <http://www.currentscience.ac.in/cs/php/feat.php?feature=Special%20Section:%20Low%20Energy%20Nuclear%20Reactions&featid=10094>
- [2] A. Meulenberg and K.P. Sinha, Tunneling beneath the $^4\text{He}^*$ fragmentation energy, *J Condensed Matter Nucl. Sci.* **4** (2011) 241–255.
 - [3] A. Meulenberg, From the Naught orbit to He^4 ground state, *16th Int Conf on Condensed Matter Nuclear Science*, Chennai, February 6–11, 2011, *J Condensed Matter Nucl. Sci.* **10** (2013) 15–29.
 - [4] A. Meulenberg and K.P. Sinha, Deep-electron orbits in cold fusion, *17th Int. Conf. on Condensed Matter Nuclear Science*, Daejeon, South Korea, 12–17 August, 2012, *J. Condensed Matter Nucl. Sci.* **13** (2014) 368–377.
 - [5] A. Meulenberg and K.P. Sinha, Deep-orbit-electron radiation emission in decay from $^4\text{H}^{*}\#$ to ^4He , *17th Int. Conf. on Condensed Matter Nuclear Science*, Daejeon, South Korea, 12–17 August, 2012, *J. Condensed Matter Nucl. Sci.* **13** (2014) 357–368.
 - [6] A. Meulenberg, Femto-atoms and transmutation, *17th Int. Conf. on Condensed Matter Nuclear Science*, Daejeon, South Korea, 12–17 August, 2012, *J. Condensed Matter Nucl. Sci.* **13** (2014) 346–357.
 - [7] A. Meulenberg, Femto-helium and PdD transmutation, *18th Int. Conf. on Condensed Matter Nuclear Science*, Columbia, Missouri, 25/07/2013, *J. Condensed Matter Nucl. Sci.* **15** (2015) 117–124.
 - [8] K.P. Sinha and A. Meulenberg, Lochon catalyzed D–D fusion in deuterated palladium in the solid state, *Nat. Academy Sci. (India) Lett.* **30**(7,8) (2007) arXiv:0705.0595v1.
 - [9] A. Meulenberg and K.P. Sinha, Composite model for LENR in linear defects of a lattice, *18th Int. Conf. on Condensed Matter Nuclear Science*, Columbia, Missouri, 25/07/2013, Proceedings at <http://hdl.handle.net/10355/36818>.
 - [10] A. Meulenberg, Pictorial description for LENR in linear defects of a lattice, *17th Int. Conf. on Condensed Matter Nuclear Science*, Columbia, Missouri, 25/07/2013, *J. Condensed Matter Nucl. Sci.* **15** (2015) 106–116.
 - [11] A. Meulenberg and J.-L. Paillet, Implications of the electron deep orbits for cold fusion and physics, *20th Int. Conf. on Condensed Matter Nuclear Science*, Sendai, Japan, October 2016.
 - [12] R.L. Mills, *The Grand Unified Theory of Classical Physics*, 2011, ed. Black Light Power.
 - [13] J.-L. Paillet and A. Meulenberg, Basis for electron deep orbits of the hydrogen atom, *Proc. of ICCF19, 19th Int. Conf. on Cond. Matter Nuclear Science*, Padua, Italy, 13–17 April 2015, *J. Condensed Matter Nucl. Sci.* **19** (2016) 230–243.
 - [14] J.-L. Paillet and A. Meulenberg, Arguments for the anomalous solutions of the Dirac equations, *J. Condensed Matter Nucl. Sci.* **18** (2016) 50–75.
 - [15] J.P. Vigier New hydrogen (deuterium) Bohr orbits in quantum chemistry and cold fusion processes *Proc. ICCF4*, 1994 Hawaii, p.7-1.
 - [16] A.O. Barut *Surv High Energy Phys.* **1**(1980) 113.
 - [17] N.V. Samsonenko, D.V. Tahti and F. Ndahayo *Phys. Lett. A* **220** (1996) 297–301.
 - [18] A. Dragic, Z. Maric and J.P. Vigier, *Phys. Lett. A* **237** (1998) 349–353.
 - [19] S. Ozcelik and M. Simsek, *Phys. Lett. A* **152** (1991) 145–149.
 - [20] B. Thaller, *The Dirac Equation*, Springer, Berlin, 1992.
 - [21] B. Thaller, *The Dirac Operator*, in *Relativistic Electronic Structure Theory: Part 1*, (Theoretical and Computational Chemistry #11), Chapter 2, P. Schwerdtfeger (Ed.), Elsevier, Oxford, 2002, pp. 23–105.
 - [22] D.G. Currie, T.F. Jordan and E.C.G. Sudarshan, Relativistic invariance and hamiltonian theories of interacting particles, *Rev. Mod. Phys.* **34** (1963) 350–375.
 - [23] H.W. Crater, R.L. Becker, C.Y. Wong and P. Van Alstine, A detailed study of “Nonperturbative Solutions of Two-Body Dirac Equations”, Oak Ridge National Laboratory (ORNL), Central Research Lib., Martin Marietta, D.O.E, Dec. 1992.
 - [24] J.A. Maly and J. Va’vra, Electron transitions on deep Dirac levels II, *Fusion Technol.* **27**(1) (1995) 59–70.
 - [25] N. Dombey, The hydrino and other unlikely states, arXiv:physics/0608095v1, 2006.
 - [26] J. Naudts, On the hydrino state of the relativistic hydrogen atom, arXiv:physics/0507193v2.5, 2005.
 - [27] L.I. Schiff, *Quantum Mechanics*, 3rd Edition, McGraw-Hill, New York, 1968.
 - [28] A. de Castro, Orthogonality criterion for banishing hydrino states from standard quantum mechanics, *Phys Lett A* **369**(5) (2007) 380–383.
 - [29] T. Nadareishvili and A. Khelashvili, Some problems of self-adjoint extension in the Schrödinger equation, <http://arxiv.org/pdf/0903.0234.pdf>.

- [30] G. Bonneau, J. Faraut and G. Valent, Self-adjoint extensions of operators and the teaching of quantum mechanics, arXiv:quant-ph/0103153v1.
- [31] J.A. Maly and J. Va'vra, Electron transitions on deep Dirac levels I, *Fusion Technol.* **24**(3) (1993) 307–318.
- [32] S. Fluegge, *Practical Quantum Mechanics*, Vol. 2, Springer, Berlin, 1974.
- [33] John W. Pearson, *Computation of Hypergeometric Functions*, School of Mathematics, The University of Edinburgh, 2009/9/4. Link= ox.ac.uk.
- [34] R.T. Deck, J.G. Amar and G. Fralick, Nuclear size corrections to the energy levels of single-electron and -muon atoms, *J. Phys. B: At. Mol. Opt. Phys.* **38** (2005) 2173–2186.
- [35] CODATA-2014, <http://physics.nist.gov/cuu/Constants/>
- [36] *Atomic Data and Nuclear Data Tables*, 2012, Elsevier, Amsterdam.



Research Article

Calorimetric Investigation of Anomalous Heat Production in Ni–H Systems

K.P. Budko*

Moscow Institute of Physics and Technology, Moscow, Russia

A.I. Korshunov†

Institute for Problems in Mechanics, Russian Academy of Sciences, Moscow, Russia

Abstract

It has been claimed that Ni–H systems produce excess heat for long periods of time. We have performed experimental calorimetric investigations of this phenomenon. The experimental setup consisted of a ceramic reactor with nickel powder inside it, a heater, hydrogen loading system and calorimeter. Nickel powders with different grain size were used because of their large surface area. Hydrogen pressure varied from 0.5 to 2.5 atm. Temperature varied from 25 to 800°C. Different methods of input power were used in order to investigate possible effects of high amplitude magnetic pulses. The experimental runs lasted from 4 to 50 h. Experiments did not show any evidence of excess heat within the accuracy of measurement.

© 2017 ISCMNS. All rights reserved. ISSN 2227-3123

Keywords: Calorimeter, Cold fusion, Hydrogen, LENR, LiAlH_4 , Nickel

1. Introduction

Since Fleischmann and Pons in 1989 claimed that it is possible to produce low energy nuclear reactions (LENR) in palladium during heavy water electrolysis practically at room temperature [1] researchers all over the world have been searching for evidence of that phenomenon in different metal–hydrogen systems. Nowadays, the most promising systems for LENR are palladium–hydrogen (deuterium) and nickel–hydrogen (deuterium) [2–15]. In the majority of experimental work of recent years, the metal is usually in solid bulk phase and hydrogen is in the gaseous phase. The process of gas loading/unloading is used to trigger the reaction. Some people suppose that nuclear reactions mainly take place on the surface of the metal [16], which is why metal powders with micro- and nanometer grain size are commonly used in experiments. Almost every LENR researcher agrees that some sort of catalyst is required for

*E-mail: kpb@lcard.ru

†Corresponding author. E-mail: fallex@inbox.ru

reaction to start. Recent investigations showed that lithium aluminum hydride (LiAlH_4) could be used as a catalyst [17,18]. It is assumed that one of the possible sources of excess energy is the fusion of lithium and hydrogen.

The main goal of our work was an experimental investigation of possible anomalous thermal effects in nickel–hydrogen systems. To obtain reliable results we used a calorimetric system. We also investigated possible catalytic effects of LAH and high amplitude magnetic pulses using different methods of input power.

2. Experimental Setup

The calorimetric system is shown in Fig. 1. It is a reactor capsule (6) made of stainless steel with plugs at both ends which are fixed by a super kanthal wire. The inner diameter of capsule is 11 mm and length (without plugs) is 50 mm. The working volume is 4.75 cm^3 . The reactor is placed into a cylindrical gas chamber (5) made of duralumin with an outer diameter of 20 mm and length of 120 mm. A heater coil of super kanthal wire is wound on the ceramic tube which is tightly placed inside the duralumin chamber. With coil resistance of 15Ω and currents up to 4.5 A it is possible to vary input power from 0 to 300 W. The outer shell of the calorimeter is covered with thermal insulation (4) made of mineral wool and cement. There are three thermosensors, one of them (7) is a K-type thermocouple and it measures the temperature of the reactor, and the other two (11) and (2) are integral temperature sensors (Analog Devices, ADT7310), that measure the input and output temperature of flowing water. The water pump has an adjustable flow rate. Since the total hydraulic resistance of the system is unknown, the flow value was obtained during simple calibration tests by measuring the total mass of water pumped over a certain period of time. All wires were routed through the holes which were then filled with epoxy glue. To measure pressure in the reactor zone, an integrated silicon sensor (NPX, MPX5700AP) (14) is used. In practically all experimental runs the maximum pressure was no more than 2.5 atm. The input power is calculated by direct multiplication of current by voltage in run-time mode. For this purpose, a device (8) based on an STM32 controller and high-speed 14-bit ADCs (10 MHz) was constructed and used. The output power

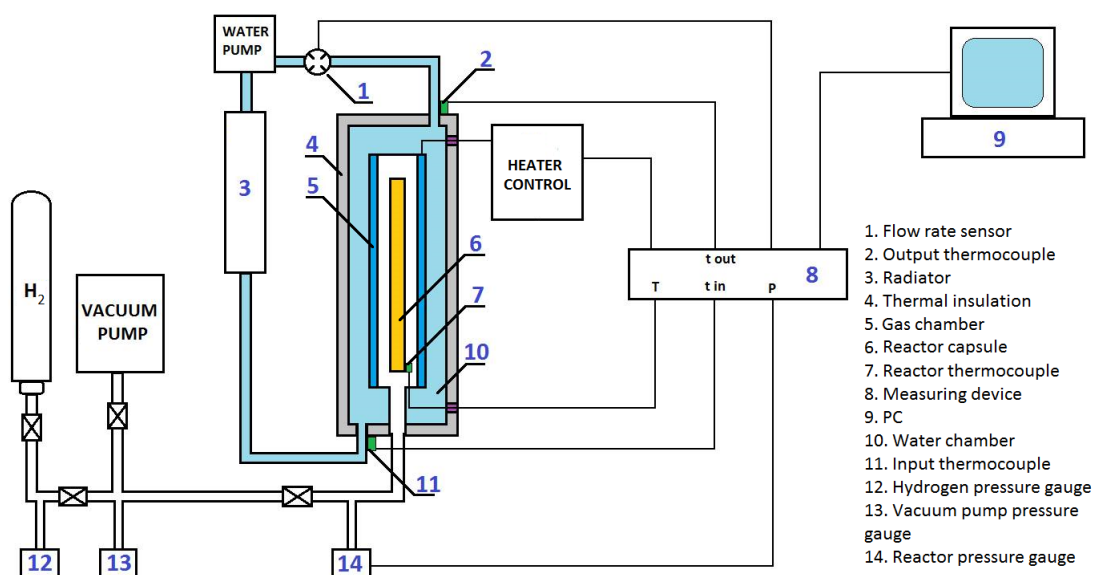


Figure 1. Schematic of calorimetric system.

data were obtained from thermocouples readings and values of water flow in the pump.

Two different types of nickel powders were used as fuel: micro-nickel with a grain size of about 10–20 μm , and nano-nickel with a grain size of about 60–80 nm. Usually we used different mixtures of these nickel powders and alumina powder (Al_2O_3 , grain size about 5 μm). The latter was mainly used as a spacer and allowed us to vary the surface area of the fuel and to prevent nickel powder from sintering at high temperatures. The typical amount of fuel was about 10 g. All fuel mixtures were prepared in a normal atmosphere without annealing. Also, in some experiments small amounts of LiAlH_4 in powder form were added to the fuel in order to investigate its catalytic effect.

The experimental run was usually comprised of periods of heating (1–120 min) and pauses between them (1–60 min) when the heater was turned off. In order to investigate possible effects of alternating magnetic field several types of input power were used: DC, DC pulses and AC. In the second case, the duration and of pulses pauses between them varied from 100 μs to 1 s. In the case of AC, the frequency varied from 10 to 20 000 Hz. Schematic diagrams of input power modes are shown in Fig. 2. The number of turns of the heater coil was $N = 100$, and its inductance is 27 μH . Since pulse rise time is about 10 μs , it is possible to obtain $dH/dt \approx 3.75 \times 10^8 \text{ A/ms}$.

To calibrate the calorimetric system and to determine radiation losses, we loaded an empty reactor capsule with hydrogen to a given pressure and then turned on constant power for a rather long period of time until all measured parameters reached equilibrium. Performing this procedure for different pressures and different modes and values of input power, we obtained equilibrium temperature levels and values of energy losses, which were no more than 6%.

3. Results

The experimental runs lasted from 4 to 50 h. Initial hydrogen pressure varied from 0.5 to 1.5 atm. With fuel mixtures containing only nickel and Al_2O_3 , the maximum pressure usually did not exceed 2.5 atm., but when mixtures with LiAlH_4 were used, maximum pressure often exceeded 3 atm. and we had to open a gas valve at the beginning of the first cycle to reduce the pressure to an acceptable value. During heating cycles the temperature of reactor reached 800°C. An example of typical run with DC-mode and 10 g of nanoNi + 1g of LiAlH_4 as a fuel is shown in Fig. 3. As can be seen, pressure follows the temperature with some delay. The whole system is rather inert. The COP was calculated using equilibrium values of input and output power taken from the end of each pulse. Using calorimetric

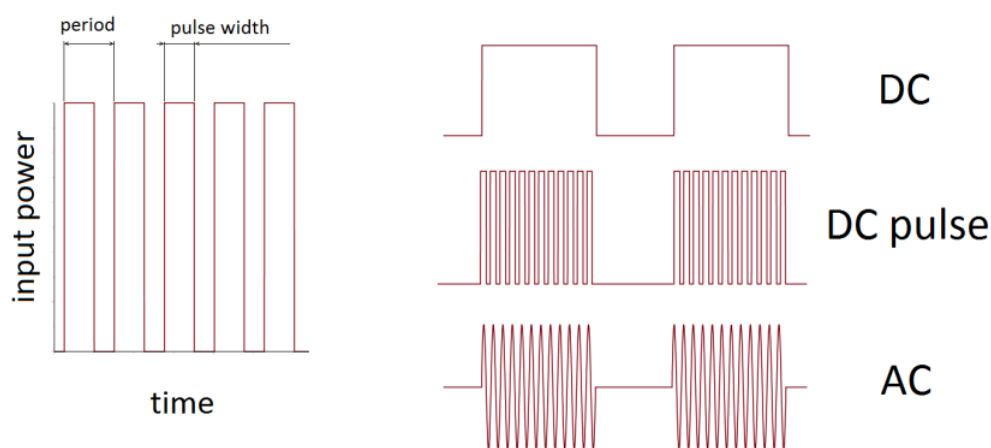


Figure 2. Schematic diagrams of different input power modes.

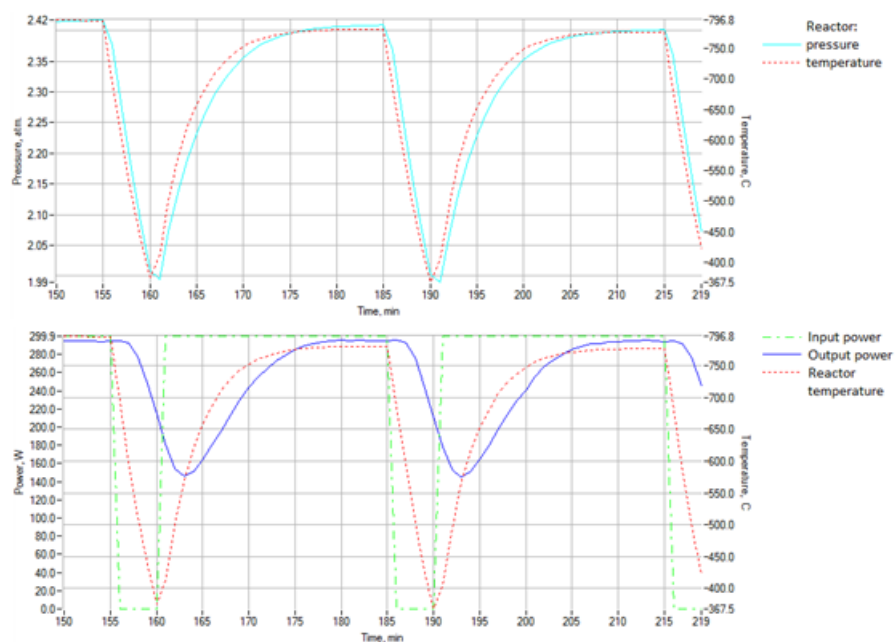


Figure 3. Segment of typical experimental run (DC mode, 10 g of nanoNi and 1 g of LiAlH₄).

data with this method, we did not observe any fast single events of excess heat generation. It was possible to detect such events only from temperature data, but accurate analyzing of all experimental data did not reveal any excess heat.

Table 1. Results of calorimetric experiments

Experiment No.	Fuel type	Ni mass (g)	Al ₂ O ₃ mass (g)	LiAlH ₄ mass (g)	Period/ Pulse width (min/min)	Experiment time (h)	Average COP
1	Nano-Ni	10	—	—	35/30	12	0.956
2	Nano-Ni	5	5	—	35/30	12	0.958
3	Nano-Ni	2	8	—	35/30	12	0.953
4	Nano-Ni	5	5	1	60/40	24	0.959
5	Nano-Ni	10	—	1	60/40	24	0.941
6	Nano-Ni	5	—	5	45/40	24	0.954
7	Micro-Ni	10	—	—	60/40	50	0.951
8	Micro-Ni	7.5	2.5	—	60/40	50	0.953
9	Micro-Ni	5	5	—	60/40	50	0.958
10	Micro-Ni	2.5	7.5	—	60/40	50	0.944
11	Micro-Ni	5	5	1	45/40	12	0.948
12	Micro-Ni	10	—	1	45/40	12	0.946
13	Micro-Ni	7	—	3	45/40	12	0.951
14	Nano-Ni	8	2	—	40/30	8	0.935
15	Nano-Ni	8	2	2	40/30	8	0.928
16	Micro-Ni	8	2	—	40/30	8	0.931
17	Micro-Ni	8	2	2	40/30	8	0.934

The main results for different fuel mixtures are presented in Table 1. Every experiment presented in this table except of final four (14–17) was conducted three times with different power profiles: DC, DC pulses with period of 200 μ s and duration of 100 μ s and AC with frequency 20 kHz. The last four (14–17) were conducted for seven different power modes: DC, DC pulses with duration of 100 μ s, 1 ms, 1 s and period of 200 μ s, 1 ms and 1 s, AC with frequencies 50, 1000 and 20 000 Hz. Average COP for every single experiment was calculated on the basis of all runs. It can be seen that the COP in all experiments does not exceed 1. Also, there is no obvious relation between COP and fuel type. The only notable consequence of using LiAlH_4 as a catalyst was the generation of large amounts of hydrogen, especially in those experiments where more than 1 g of LiAlH_4 was used. No influence of an alternating magnetic field on output power was found: no matter what kind of power supply was used, the final results depended only on total value of input electric power.

4. Conclusion

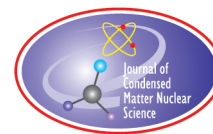
The calorimetric experiments with two types of nickel powders and hydrogen did not show any evidence of excess heat within the accuracy of measurement. A possible catalytic effect of LiAlH_4 was not found. Possible influence of an alternating magnetic field was not observed: total output power depended only on total input power.

Many researchers agree that low energy nuclear reactions can occur in the range of high temperatures ($>1200^\circ\text{C}$) and high pressures (up to 100 kPa). Also, using deuterium instead of hydrogen could be more fruitful to attain extra heat generation. We did not investigate these possibilities, but we are going to in future experiments.

References

- [1] M. Fleischman, S. Pons and M. Hawkins, Electrochemically induced nuclear fusion of deuterium, *J. Electroanal. Chem.* **261** (2) (1989) 301.
- [2] S. Focardi, R. Habel and F. Piantelli, Anomalous heat production in Ni–H systems, *Nuovo Cimento A* **107** (1994) 163.
- [3] S. Focardi, V. Gabbani, V. Montalbano, F. Piantelli and S. Veronesi, Large excess heat production in Ni–H systems, *Nuovo Cimento* **111A** (11) (1998) 1233.
- [4] A. Rossi, Method and apparatus for carrying out nickel and hydrogen exothermal reaction, U.S. Patent 20110005506 A1, January 13, 2011.
- [5] A. Rossi, Fluid heater, U.S. Patent 9115913 B1, August 25, 2015.
- [6] Y. Sasaki, A. Kitamura, Y. Miyoshi and Y. Fujita, Anomalous heat generation in charging of Pd powders with high density hydrogen isotopes (I) results of absorption experiments using Pd powders, *15th Int. Conf. on Condensed Matter Nuclear Science*, Rome, Italy, 2009.
- [7] Y. Sasaki, A. Kitamura, T. Nohmi, Y. Miyoshi, A. Taniike, A. Takahashi, R. Seto and Y. Fujita, deuterium gas charging experiments with Pd powders for excess heat evolution (I) results of absorption experiments using Pd powders, *9th Meeting of Japan CF-Research Society*, Shizuoka, Japan, 2009.
- [8] A. Takahashi, A. Kitamura, T. Nohmi, Y. Sasaki, Y. Miyoshi, A. Taniike, R. Seto and Y. Fujita, Deuterium gas charging experiments with Pd powders for excess heat evolution (II) discussions on experimental results and underlying physics, *9th Meeting of Japan CF-Research Society*, Shizuoka, Japan, 2009.
- [9] A. Kitamura, T. Nohmi, Y. Sasaki, Y. Taniike, A. Takahashi, R. Seto and Y. Fujita, Anomalous effects in charging of Pd powders with high density hydrogen isotopes, *Phys. Lett. A*. 2009. V. **373**(35), pp. 3109–3112.
- [10] D. Kidwell, A. Rogers, K. Grabowski and D. Knies, Does gas loading produce anomalous heat? *15th Int. Conf. on Condensed Matter Nuclear Science*, Rome, Italy, 2009.
- [11] F. Celani, P. Marini, V. di Stefano, A. Spallone, M. Nakamura, E. Purchi, O.M. Calamai, V. Andreassi, E. Righi, G. Trenta, A. Marmigi, G. Capuccio, D. Hampai, F. Todarello, U. Mastromatteo, A. Mancini, F. Falcioni, M. Marchesini, P. di Biagio, U. Martini, P.G. Sona, F. Fontana, L. Gamberale and D. Garbelli, Deuteron electromigration in thin Pd wires coated with nano-particles: evidence for ultra-fast deuterium loading and anomalous, large thermal effects, *Int. Conf. on Condensed Matter Nuclear Science*, Washington, DC, 2008.

- [12] F. Celani, P. Marini, V. di Stefano, M. Nakamura, O.M. Calamai, A. Spallone, E. Purchi, V. Andreassi, B. Ortenzi, E. Righi, G. Trenta, G. Capuccio, D. Hampai, F. Piastra and A. Nuvoli, Towards a high temperature CMNS reactor: nano-coated Pd wires with D₂ at high pressures, *15th Int. Conf. on Condensed Matter Nuclear Science*, Rome, Italy, 2009.
- [13] X.Z. Li, B. Liu, N.N. Cai, Q.M. Wei, J. Tian and D.X. Cao, Progress in gas-loading D/Pd system—the feasibility of a self-sustaining heat generator, *10th Int. Conf. on Cold Fusion*, 2003.
- [14] F. Celani, G. Vassallo, E. Purchi, F. Santandrea, S. Fiorilla, A. Nuvoli, M. Nakamura, P. Cirilli, A. Spallone, B. Ortenzi, S. Pella, P. Boccanera and L. Notargiacomo, Observation of macroscopic current and thermal anomalies, at high temperature, by hetero-structures on thin and long constantan wires under H₂ gas, *19th Int. Conf. on Condensed Matter Nuclear Science*, Padua, Italy, 2015.
- [15] G.H. Miley, K.-J. Kim, E. Ziehm, T. Patel and B. Stunkard, Progress in development of an LENR power cell for space, *Proc. of Nuclear and Emerging Technologies for Space (NETS)*, 2015, Albuquerque, NM, February 23–26, 5134, pp. 325–335.
- [16] E. Storms, An *Explanation of Low-energy Nuclear Reactions (Cold Fusion)*, *J. Condensed Matter Nucl. Sci.* **9** (2012) 1–22.
- [17] A. Parkhomov and E. Belousova, Researches of the heat generators similar to high temperature Rossi reactor, *19th Int. Conf. on Condensed Matter Nuclear Science*, Padua, Italy, 2015.
- [18] G. Levi, E. Foschi and H. Essen, Observation of abundant heat production from a reactor device and of isotopic changes in the fuel, 2014, <http://www.infinite-energ>



Research Article

Perspective on Low Energy Bethe Nuclear Fusion Reactor with Quantum Electronic Atomic Rearrangement of Carbon

Stephane Neuville*

TCE Consulting, F-77165, Cuisy, France

Abstract

The relatively low/medium proton/carbon collision threshold energy (1–8 keV) of the Bethe–Weizsäcker nuclear reaction cycle C, N, and O observed in low temperature carbon rich stars suggests the eventual technical feasibility of a solid-state carbon fusion reactor. H^+ used as a precursor nuclear material can be implanted in solid-state carbon material. We must then consider all effects that can affect nuclear collision efficiency, including solid-state structure specificity, proton channeling and the reduction of the original proton energy with electronic interactions, before looking at the possible nuclear reactions themselves. We then have to consider the different effects and types of atomic rearrangement favoring either sp^2 or sp^3 sites or which influence the carbon material structure. For this purpose, we review first a recently developed theoretical approach, which might explain important aspects of this phenomenon with still high confidence up to now. These aspects include quantum electronic activation especially with H_2 recombination energy release, which is different from usual chemical and metallurgical thermal atomic rearrangement with which an optimized ta-C sp^3 carbon structure can be controlled. It should also be considered that carbon structure determination methodology – including the recently revised Raman theory – provide more correct and accurate results. To be falsified a study of this type of proton–carbon nuclear reactor must also take into account effects which modify the carbon nucleus structure in favor of nuclear fusion. It is suggested that anharmonic synchronic phonon–nuclear resonance may be a contributing factor. However, present failures and the limits of abstract Quantum Mechanical formalism bring little clarification on this last point, which we suggest is owing to insufficient physical description of particle wave character. In order to improve these aspects of the theory, we suggest revisiting aether theory which with further investigation and development of 3D fluid mechanics is expected to account for all QM acquired, and to be able to provide clearer physical insight into the subatomic particle wave aspects and corresponding nuclear reaction mechanism.

© 2017 ISCMNS. All rights reserved. ISSN 2227-3123

Keywords: Anharmonic phonon–nuclear resonance, Bethe–Weizsäcker proton CNO fusion reactor, Carbon material characterization, Synchronic phonon/proton–nucleus collision, Quantum electronic atomic rearrangement

*E-mail: stephane.neuville709@orange.fr; Tel.: +33 (0)6 4147 1922.

1. Introduction

Nuclear fusion reactions involving hydrogen isotopes have been the subject of many investigations with magnetic and inertial hot plasma fusion devices [1,2], in particular with compact high voltage (~ 100 keV) electric discharge D–D fusion neutron generators [3–5]. Such studies have also been made with nuclear fusion in solid state material. This technique may avoid the production of long lived radioactive waste, and it is expected to have higher energy production capability than nuclear fission [6,7].

Considering the relatively low threshold collision energy (1 keV range) of a nuclear fusion reaction of the Bethe–Weizsäcker H+/C, N, and O fusion cycle (Table 1), and the relatively reduced amount of energetic secondary emission [8], we focus on the study of eventual technical feasibility of a hybrid plasma/solid state H⁺/carbon fusion reactor.

Cold plasma devices are used for sputtering and Plasma Assisted Chemical Vapor Deposition (PACVD) and Arc deposition. Some of the common ones have ion energy in the 1 keV range and plasma density in pulsed mode up to 10^{12} ion/cm³ and which can produce substrate ion current density up to about 100 mA/cm² [9–19]. Dense cold plasma hydrogen in the 1 kW discharge power range (for instance with a plasma reactor of ~ 50 cm size) can produce $\sim 10^{19}$ p+/s in a 1 keV range which can interact with a carbon target material surface with 10^{15} a/cm² and with ion implantation depth of ~ 1000 atomic layers. This corresponds to solid state volume containing $\sim 10^{21}$ carbon atoms which can interact with impinging protons (considering for instance 100 μ s DC pulsed mode with 10 ms duty cycle) [20–22].

The reported proton nuclear reaction rate is about 10^{-3} [7] achieved with a picosecond high energy proton source [23]. This produces a laser shot generated proton bunch, containing $\sim 10^7$ protons of energy above the nuclear collision fusion threshold. This collides with a dense boron plasma estimated in the 10^{16} ion/cm³ range (produced by a 1 ns laser shot after 1 ns expansion [7]). Considering the size of the roughly described cold plasma/carbon solid state reactor described above, and the proton nuclear reaction rates analogous to the previously mentioned proton/boron plasma experiment, this would correspond to a theoretical delivered nuclear power of ~ 100 kW.

No fusion energy has been reported with diamond-like carbon (DLC) cladded hot plasma reactor wall. These reactor walls are used in order to avoid erosion of refractory heavy metal wall material [24,25]. We suggest this can be explained to some extent by the much lower p+ flux on the reactor wall. The same explanation may also apply to a thermal shield solar wind erosion study [26,27].

However, with an experiment using simulated solar wind 2 keV/4 keV proton irradiation (in the 10^{-8} A/cm² range) of a carbonaceous target [26,27], the following was observed: with recently revisited Raman spectroscopy fundamentals [28] and detailed analysis of Raman spectrum, it appears that the carbon material is subject to partial sp³ atomic rearrangement (an endothermic process) [29], which is enhanced with additional hard UV irradiation. This effect is normally not observed when a graphitic material for which the graphite crystallite are growing in size [30,31] is only heated, without hard UV irradiation.

From fusion experiments involving the collision of energetic H⁺ flux on a dense boron plasma, it is known that fusion efficiency is much higher than for the same H⁺ flux impinging on a solid-state boron target, which has paradoxically at least about $10^2/10^3$ much higher density of nuclei [7]. We suggest this should be interpreted with reference to

Table 1. Bethe CNO fusion cycle.

$^{12}\text{C} + ^1\text{H}$	\rightarrow	$^{13}\text{N} + \gamma + 1.95 \text{ MeV}$
^{13}N	\rightarrow	$^{13}\text{C} + e^+ + \nu e + 2.22 \text{ MeV}$
$^{13}\text{C} + ^1\text{H}$	\rightarrow	$^{14}\text{N} + \gamma + 7.54 \text{ MeV}$
$^{14}\text{N} + ^1\text{H}$	\rightarrow	$^{15}\text{O} + \gamma + 7.35 \text{ MeV}$
^{15}O	\rightarrow	$^{15}\text{N} + e^+ + \nu e + 2.75 \text{ MeV}$
$^{15}\text{N} + ^1\text{H}$	\rightarrow	$^{12}\text{C} + ^4\text{He} + 4.96 \text{ MeV}$

the fact that H^+ loses in a solid-state material ($\sim 10^{22}$ atom/cm³) about 90% of its energy with electronic interaction [25]. Only a reduced amount of implanted H^+ will have energy above nuclear reaction threshold and can collide with carbon nuclei. Meanwhile, the optimized nuclear collision probability is achieved with much lower electron density ($< 10^{16}$ /cm³) in an expanding plasma, according to an experiment produced with high energy proton interacting with such expanding plasma [7, 21,22]. Thus, showing the importance of (a) electronic shielding which has to be kept as low as possible and (b) reduced H^+ channeling with which H^+ can lose much of its energy before colliding with a carbon nucleus. This is a particularly important effect in crystalline carbon material and especially in diamond [32–40]. These results suggest that the carbon material should be as dense as possible, and amorphous.

The question is then whether the resulting distribution of collision density and energy in carbon materials might be sufficient to cause a significant amount of nuclear reactions producing more energy than consumed. Therefore, the first thing to consider is whether different physicochemical effects which affect the atomic distribution of atomic nuclei and the resulting atomic structure which determines the electronic spatial distribution of each nucleus.

Beside evaporation/sputtering of the carbon target, it is especially important to consider the role of atomic rearrangement induced by quantum electronic activation (QEA) (reviewed in Section 3) [29]. Evidence for this effect was first seen in carbon materials, considering the important differences of carbon material properties linked to its structure [41] and based on different electronic orbital hybridization (mainly sp^2 and sp^3), different atomic packing density and different interatomic bond energy [9]. However, it is only possible to conveniently observe this with detailed and accurate characterization of carbon material structure for which updated Raman spectrometry fundamentals appears necessary [28]. This is the reason we include a brief review in Section 4.

Although no Mossbauer effect can be observed with carbon atoms (essentially a question of the misfit between available γ source wave length and nuclear energy levels) [42,43] some modification – however small – of its nuclear structure under the influence of the electronic environment is to be expected, which might affect the fusion collision energy threshold with some synchronic mechanisms. We will discuss this in Section 5.

It appears that conventional quantum mechanical formalism at the present stage cannot explain all aspects of electron/nucleus interaction which might enhance nuclear reaction efficiency. In order to get clearer insight on how nuclei can be fused after collision we suggest revisiting some aspects of quantum mechanics (discussed in Section 6).

2. Hydrogen in Materials

Hydrogen being monovalent, bonding chain discontinuities can appear. If chemically bonded on one side ($M-H \dots$, then the H atom will generally be only weakly bonded on the other side. Instead of strong $M-M-M$ chains, it will be possible to have weak $M \dots H-H \dots M$ chains able to enhance some of the brittleness of metals [44]. This explains the lower hardness and plasticity of polymers [9,45]. Hydrogen is more easily introduced in substrate material which has lower atomic density and especially after being dissociated to H^* and/or ionized to H^+ . And this effect is clearly shown with results of ion implantation and H^+ channeling experiments [20,34–40,46]. The H^* and H^+ hydrogen can be absorbed in higher amounts in more porous and less dense metals [47,48].

The reverse effect is likely to be achieved when the material is heated up with H_2 exodiffusion, when $M-H$ binding energy is lower than $H-H$ (~ 5 eV and a similar level for $O-H$) in comparison for instance to $C-H$ (~ 4 eV up to 4.5 eV) and to $H \dots H$ physical hydrogen bonds (~ 0.1 eV). This explains, for instance, the relatively reduced thermal and chemical stability of polymeric carbon material and their reduced hardness, whenever they contain a high number of sp^3 sites such as in diamond [9,29]. Frozen methane containing 100% sp^3 has nothing to do with diamond and has, like frozen water, only relatively low hardness compared to harder steel, chromium, Al_2O_3 , CW, TiN, etc. (hardness density of cohesion energy [29,48]). H can also be more tightly trapped in denser and harder materials corresponding to good diffusion barrier properties for H_2 , such as ta-C and defect-free graphene and also glassy carbon, the latter despite being porous (with isolated pores) [49,50], in contrast to H^+ for which even graphene is porous [51]. Therefore,

trapped atomic hydrogen released with the higher temperature can recombine to H_2 with Chemical Recombination Energy Release (CRER). This energy can be partly absorbed with anomalous atomic rearrangement, before being released in the form of heat [52].

This has been observed especially with Nickel alloys [53], and miscellaneous other alloys [54,55] for which hydrogen is introduced in the bulk through the surface by different means (for instance with H^+ in a polarized salty solution, or when H_2 is dissociated on the surface by catalytic effects, or with plasma surface interaction producing ion implantation, etc.). In such cases, after the exodiffusion of recombined H_2 , tensile stress and cracks can appear favoring brittleness whenever no hydrides have been formed [56]. Therefore, atomic rearrangement to a structure with higher atomic packing density where the endothermic intrinsic atomic rearrangement effect can be in competition with the exothermic effect of the chemical recombination energy release, as we briefly review in Section 3.

3. Brief Review of Quantum Electronic Atomic Rearrangement

Many experiments in the chemical synthesis and formation of metastable material have shown that quantum electronic activation effects obtained, for instance with various photonic excitations, can play a decisive role for the achievement of some desired specific molecular configuration, and that it is not possible to replace photon activation by equivalent heat introduced from outside [57].

Quantum electronic atomic rearrangement (QEAR) for which higher activation energy (1–10 eV range) is involved, is different from Thermal Solid-State Atomic Rearrangement (TAR) where much lower thermal energy is generally involved (0.01–0.3 eV range) corresponding to temperature lower than 3000 K. The QEAR can be caused by many different kinds of physical electronic activation (before being transformed into heat) and therefore often produces metastable structures, whenever the effect is also able to enhance transformation kinetic towards ground state (for instance Si recrystallization either with H_2 recombination or by laser processing) [58–60]. Meanwhile TAR is ruled by Arrhenius thermal statistics which generally transforms the material towards its groundstate and which can be in competition with the first effect. Higher activation energy levels and rates can produce atomic rearrangement of merely graphitic material towards a harder and denser diamond-like carbon structure, meanwhile temperature will convert glassy carbon, diamond-like carbon and diamond to graphite [29,31,61,62].

Many other materials, including different metals, are known to have different oxidation states corresponding to different stoichiometric possibilities and atomic structures of different atomic packing density, such as C, Cr, Fe, Ni, Cu, Pd, Ta, etc. [44,48,63], and for which different hybridization states can exist, generally corresponding to hexagonal and cubic structure of different packing density [64]. For instance, cubic Si corresponds to its ground state, while silicene corresponds to a metastable structure [65], in contrast to carbon and to nickel.

Given the numerous compounds associated with different carbon solid state configurations between monocrystalline diamond and monocrystalline graphite [41,66] (Fig. 1), different kinds of atomic rearrangement exist [29], which can be detected by the modification of the carbon solid state optoelectronic gap (which is much higher in diamond and diamond like material than in graphitic material), and with accurate characterization of the different carbon types [9,67]. Raman spectrometry is considered one of the best carbon characterization tools. However, many incoherent aspects of this technique could be found in literature. This is why the latest updated method has to be used in this study [28], as we briefly explain in Section 4.

3.1. Graphitic thermal degradation and metastable diamond-like material reforming

Graphitic degradation is generally observed during longer thermal annealing of diamond [31,61,68]. This produces different kinds of diamond-like carbon (DLC) [41,61], including the so-called amorphous hydrogenated carbon (a-C:H) [52] and carbon material such as filled carbon wires and fibers containing both sp^2 and sp^3 sites [69,70]. Some

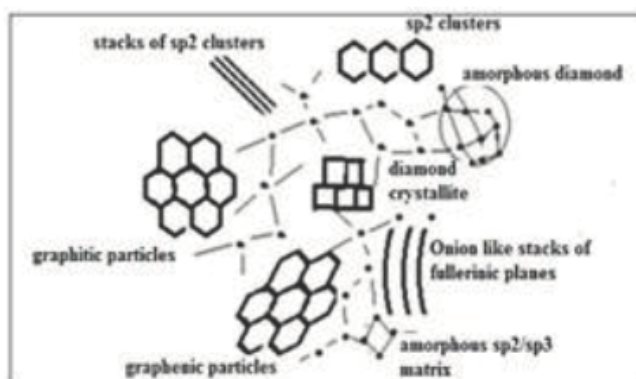


Figure 1. Scheme of composite DLC carbon material.

materials such as hollow carbon nano-tubes (CNT) or graphene, which are materials close to graphitic ground state (containing hexagonal cyclic rings similar to graphite), will not be degraded and can have some defects eliminated at higher temperatures when the temperatures stay below sublimation temperature (~ 3500 K) [71,72].

It is known that diamond, a metastable material, is formed when higher temperatures along with pressure, and that its thermal graphitic degradation starts at about 800°C [31,61,62], when no other physical effects hamper or go against this process [52,57,73,74]. This is the reason why some DLC material has been produced with thermal spikes during plasma and ionic processes [62]. However, many other effects other than pressure and thermal spikes have also been identified as favoring diamond-like materials and diamond growth, such as hot filament diamond deposition, low bias plasma deposition [68], energetic UV (>5 eV) [73], X-ray irradiation [75], chemical and catalytic reactions and especially those associated to H_2 and N_2 chemical recombination [29,52,67,76,77]. External input of heat alone will not produce diamond-like atomic rearrangement [57]. The Ion Beam Assisted Depositing (IBAD) process and Filtered Cathodic Vacuum Arc (FCVA) devices can produce ta-C when the density of the ion bombardment is high enough and when the temperature is low enough [10,11,78,79]. This is achieved with quantum electronic activation with released ion neutralization energy and ion implantation compressive stress which favor DLC with higher sp^3 content and with the combination/addition of all these different effects [10,29].

With updated Raman spectroscopy [28] (reviewed in Section 3.2) many published works show that carbon material processing that is supposed to produce graphitic material, often in fact contains some DLC and sometimes also some nanocrystalline diamond [52,67]. This is shown, for instance, with graphitic material simultaneously heated up to 3000 K and irradiated with intense hard UV and 8 keV H^+ [26,27], and with a glassy carbon corresponding to graphenic and fullerene material containing sp^3 with somewhat diamond-like (hardness ~ 15 GPa) [49], for which a D diamond peak is observed at $\sim 1325\text{ cm}^{-1}$ [49,69] indicating the existence of H6 hexagonal chair diamond structure [31,79,80]. Meanwhile in this case, only a weak (~ 10 times lower intensity than H6 peak) the so-called D-disorder band at $\sim 1350\text{ cm}^{-1}$ is observed corresponding to GeA-edge phonon modes (in accordance to its overmode at $\sim 2700\text{ cm}^{-1}$ [28,29] of similar intensity).

3.2. Role of an electric field on diamond-like rearrangement of graphitic materials

An electric field is known to produce molecule distortion and polarization, which can initiate atomic rearrangements, when the polarizing energy E_p is higher than some threshold energy [29].

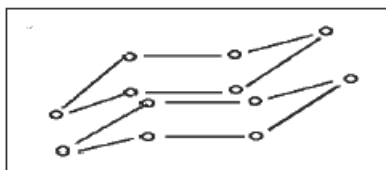


Figure 2. Stack of chair shape hexagonal cyclic rings corresponding to H6 diamond structure with sp³ sites (one carbon atom bonded equivalently to four others). Raman frequency at $\sim 1325\text{ cm}^{-1}$ according to Spear et al. [81] and Huang et al. [31].

Especially hexagonal cyclic sp² ring can be transformed into hexagonal sp³ chair structure [28,29], an observed effect when applying an electric field on aromatic compounds [82] and which can transform graphitic materials into diamond-like materials containing sp³ [83].

Consider a stack of graphene hexagonal sp² rings, in graphite and in a multiwall carbon nanotube. These can be transformed into stack of chair shape sp³ hexagonal ring [29,31,81] (Fig. 2) corresponding to H6 diamond. This is an intermediary structure between graphite and diamond, which can be observed, for instance, on the external surface of carbon fibers and wires containing both sp² and sp³, when produced with plasma activation [69,70]. A H6 structure can also be obtained by thermal graphenic degradation of carbon deposited on a cubic Si substrate, or with the epitaxial growth of Si on a graphene substrate forming a non-planar buckled silicene layer [65]. Then consider how a transient electric field can be produced in a growing carbon material film, with the different reported activation mechanisms favoring DLC material growth. Adsorption of molecules on some semiconducting materials can produce a transient transverse electric field, similar to what is achieved with the Dember effect [84]. This occurs when pairs of electron/hole (with different diffusion mobility) are activated on a semiconductor surface, before producing heat and therefore, it is not of thermal origin. This happens instead via a direct transfer of adsorption energy to valence band electrons [29]. Investigation on CO adsorption on a Ni substrate confirm this effect by showing IR photon emission corresponding to the same adsorption energy release (no substrate heating) [85]

3.3. Role of released chemical recombination energy on valence band electron excitation

Energy released by electric neutralization ($\sim 10\text{ eV}$), chemical recombination (CRER) (~ 1 up to $\sim 20\text{ eV}$) and chemisorption ($\sim 7\text{ eV}$ in the case of C–C bond formation on appropriate surface sites) produces quite high activation energy, before it produces heat. H–H ($\sim 5\text{ eV}$) recombination should mainly be considered, besides other types of high CRER such as O–H, F–H, etc. These are reviewed in [29]. Dissociation energy has to be subtracted from these.

Table 2 gives a list of recombination energy releases involving C and H during the growth of diamond and a-C:H with hydrocarbon precursors. Figure 3 shows how CRER is particularly important with chemical recombination of $\text{N}\equiv\text{N}$ ($\sim 12\text{ eV}$) and corresponding to many observable diamond crystallites which have been formed by atomic rearrangement during annealing of CN_x materials and depending on N distribution [29,66]. A similar effect occurs with N^+ ion bombardment where N can recombine to N_2 with which glassy carbon can be transformed into N doped ta-C [87].

3.4. Criterion of quantum electronic sp³ activation

Carbon material has to be considered as semiconducting material (Fig. 4.), whenever the species are semimetals such as graphite and metallic nanotubes and with overlapping electronic valence σ/π and conduction σ^*/π^* bands [88].

Considering that during atomic rearrangement, the outer electron orbital activated electrons should always occupy

Table 2. H₂ and C–C chemical recombination energy release during hard carbon film growth with HC precursors.

a-C:H H* + H*	→	H ₂ + (~5 eV)	(F1)
Csp ³ -H + Csp ³ -H	→	Csp ³ - Csp ³ + H ₂ + (~3 eV)	(F2)
Csp ³ -H + H*	→	Csp ³ - Csp ² + H ₂ + (~0.5 eV)	(F3)
Csp ³ <+ 2 H*	→	Csp ² + 2H ₂ + (~1.5 eV)	(F4)
Csp ³ <+ 2 H*	→	Csp ² + 2H ₂ + (~1.5 eV)	(F5)
Csp ² <+ Csp ² <	→	Csp ² - Csp ² + 2H ₂ + (~1 eV)	(F6)
Csp ² <+ Csp ³ <	→	Csp ² - Csp ³ + 2H ₂ + (~1 eV)	(F7)
Csp ³ <+ Csp ³ <	→	Csp ³ - Csp ³ + 2H ₂ + (~1 eV)	(F8)

(with C<representing CH₂)

authorized energy levels, we postulate that they should be always activated to energy levels higher than both the original and final state (Fig. 5).

However, other conditions also have to be fulfilled. The number of activated electrons should be higher than the number of atoms which can be rearranged. This is a five-dimensional phenomenon involving local space, energy and time and for which simultaneity, activation energy level, activation intensity and the decay of several valence band electron activation events must be compatible with steric aspects. Some equations of atomic rearrangement have been established illustrating all aspects to consider [29], but we will not reproduce these equations in this review.

Carbon material can have an optoelectronic gap from a very low value (<0.1 eV in graphenic materials) up to (~2.5/3.5 eV) for DLC/ta-C and ~5.2 eV for diamond. The rearrangement criterion applies also to carbon materials with a lower final gap for which lower activation energy will be sufficient (subject to enough electrons that are locally activated).

Diamond can be produced at higher temperature ($T > 1200$ K), for which only graphitic soot would be expected if only considering usual thermal atomic rearrangement (which is governed by the Arrhenius law). Intense hydrogen CRER that favors sp³ activation can compensate for thermal graphitic degradation [29]. Longer high temperature thermal annealing of a-C:H, a-C, ta-C and diamond induces growth of sp² clusters [31,52,73,74, 89]. However, shorter thermal treatment of a-C:H, can maintain or improve their diamond-like character for a while before being degraded with longer annealing time [58,63,77]. Heating up some polymers can produce a harder glassy carbon [49].

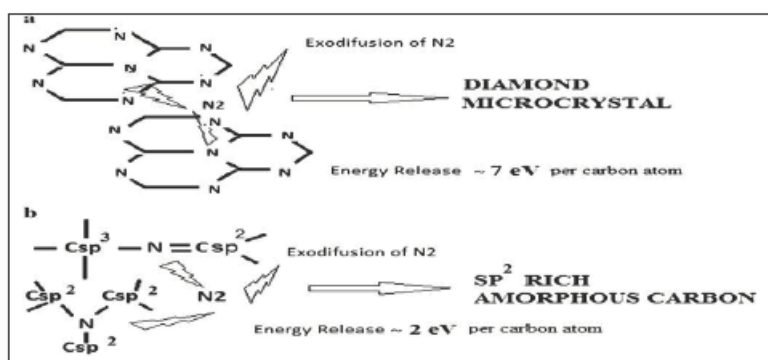


Figure 3. Formation of diamond crystallites with annealing (~700° C) of CN_x containing no molecular N₂ and ordered densely packed hexagonal planes containing substitutional H [29,66]. This is a controversial result considering that CN_x annealing usually produces graphitic carbon when containing merely molecular N₂ content (few CRER) [9,86].

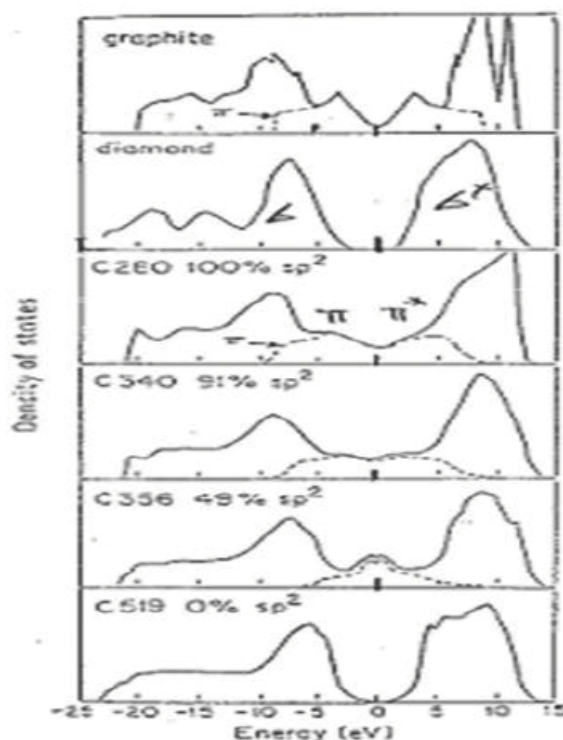


Figure 4. Density of electronic states in diamond, graphite, GLC, DLC and ta-C by Beeman et al. [76]. (1) Valence band electrons in graphite, GLC and DLC can be activated by thermal activation because of the reduced optoelectronic gap and low energy transition $\pi \rightarrow \pi^*$. (2) Whereas, for diamond and ta-C no significant $\pi\pi^*$ band exists (more or less only $\sigma\sigma^*$ bands) and gap >3 eV has to be considered for which electron excitation needs a higher quantum electronic activation. (3) A continuous band allows reduced thermal activation in favor of graphitic degradation (with which Raman effect appears with laser excitation at 514 nm (2.41 eV) $<$ gap).

3.5. Influence of atomic rearrangements on disorder and stress

Stress reduction is of particular importance because stress affects carbon film adherence [9,90,91]. Ordinary thermal annealing, while also relaxing stress, generally produces graphitic degradation. Therefore, another way to reduce stress without graphitic degradation has to be sought. Stress in carbon material can be determined by measuring mechanical bending of a thin substrate coated with the stressed material (reviewed in [9]), or by measuring the Raman shift [28,90]. Most ionic depositing processes generate internal compressive stress [91], while exodiffusion of hydrocarbon and H_2 can relax them and can sometimes produce tensile stress, when more important denser atomic rearrangement is to be considered [9,52].

Atomic rearrangements generally lead to internal stress reduction by reducing the number of defects (vacancies and interstitials) with which higher final atomic packing density and better ordered material can be achieved [28,29,76,77,86,92]. Stress can be reduced with carbon material sp^3 restructuration by using electric field [83] or with thermal annealing when combined to high energy (>5 eV) such as with UV laser irradiation or X-ray irradiation [73,75].

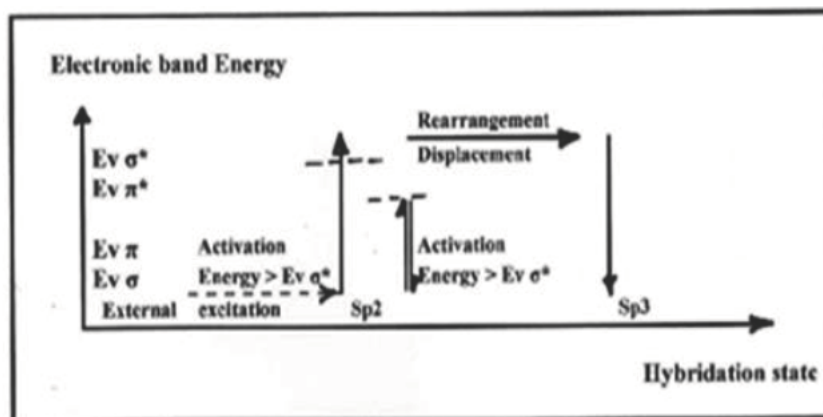


Figure 5. sp^3 rearrangement activation criteria [29]. During atomic rearrangement, electrons of the outer atomic shells must always occupy authorized energy levels. \Rightarrow valence electrons have to be excited up to conduction band levels of *initial and final* state before decay into the final valence band level.

3.6. Examples of application of sp^3 rearrangement effects

3.6.1. Catalytic effects

sp^3 atomic rearrangements can be enhanced with catalytic effects which produce higher hardness and lower hydrogen content (exodiffusion). Considering that boron has similar bonding energy with H and C, reducing the original C–H bond energy and enhancing C–C and H–H recombination higher deposition rates and higher hardness and diamond-like quality of growing a-C:H and diamond can be achieved [9,29,76,77,92]. During the growth of an ordered diamond, only thermal stress is generally produced in consequence of a different thermal dilatation coefficient between the substrate material and coating [68].

3.6.2. Transformation of graphene into the so-called graphane and related materials, when either atomic H^* or N^* or O^* is adsorbed on a multilayer graphene surface

This process transforms a highly electrical conducting graphene into a non-conducting diamond-like dielectric (gap ~ 5 eV) [93,94]. We suggest this interpretation is questionable, and it is more likely explained by the transformation of graphene into an H6 material, which like silicene is not a planar structure (hexagonal buckled sp^3 chair structure). A sharp Raman peak appears in a Raman frequency range of $\sim 1330\text{ cm}^{-1}$ which cannot correspond to any atomic disorder (otherwise the Raman signal would be broadband) and which corresponds to a compressive stress up-shifted H6 peak appearing normally at $\sim 1325\text{ cm}^{-1}$. This interpretation is in agreement with the so-called Landau No-Go criteria [95–97] explaining why graphenic C–H material cannot exist and which is confirmed with a comparison of stronger chemical bonds and weaker adsorption energy of H_2 on graphene [98].

3.6.3. Gap increase of G-C₃N₄

This material is thought to combine high electric conductivity and an appropriate gap ($\sim 1.2/1.8$ eV) for water photocatalysis producing H_2 [99–101] is confronted to undesired gap increase with important electric conductivity decrease because of transformation of G-C₃N₄ into N doped H6 structure with N_2 exodiffusion and N_2 CRER sp^3 atomic

rearrangement considering weaker C–N bonds (~ 3.16 eV) than C–C (~ 7 eV) and $\text{N}\equiv\text{N}$ (~ 12 eV).

4. Brief Review on up-dated Carbon Raman Spectrometry

4.1. Carbon structures to be considered with Raman spectroscopy

Different types of carbon materials have been identified, including micro and nano-crystalline diamond, amorphous diamond, ta-C, degraded ta-C, ta-C:H, composite diamond-like carbon with the inclusion of sp^3 cluster, sp^2 cluster and stacks of sp^2 , a-C:H, a-C (amorphous sp^3/sp^2 homogeneous mixture), composite graphite-like carbon, glassy carbon (porous mix of fullerenic, DLC and GLC), amorphous graphite, carbon wire and fiber CNW, CNF, single/multiwall CNT, multilayer/single layer graphene, fullerenic and graphenic particles, micro/nano-polycrystalline graphite which have been reviewed in detail elsewhere [41]. Note that most non-crystalline carbon materials *do not fit the general description of “amorphous carbon”* (which by definition does not contain any ordered sp^3 and sp^2 cluster substructures) [28,29,66,67,102].

Therefore, it is difficult to correctly assign each Raman band and peak when insufficient consideration is brought to peak shift, broadening, and band overlapping. Notwithstanding that very often atomic rearrangement has not been considered, for instance when unexpected D diamond peak appears in a carbon Raman spectrum after annealing of a-C:H which cannot be explained without anomalous atomic rearrangement [29,52] or with some glassy carbon material for instance [31,49,79] when a H6 hexagonal sp^3 diamond peak at $\sim 1325\text{ cm}^{-1}$ is observed different from mislabeled the so-called D-disorder peak at $\sim 1350\text{ cm}^{-1}$ corresponding to A (armchair) edge graphenic material vibration mode [28].

This is the reason we briefly review the following updated carbon Raman spectrometry fundamentals which must be considered for a detailed description of atomic rearrangement phenomena. These phenomena are reviewed in section III and correspond to several revisited aspects which have been formerly defined [103]. Before looking at carbon Raman spectra assignment, other different characterizing features have to be checked [9]: the sp^2/sp^3 ratio (for instance with carbon Auger peaks), hardness (density of cohesion energy), stress (recall relation between stress and Raman shift with Pauleau formula [90]), hydrogen content, contamination, thermal stability and elaboration process conditions defining atomic rearrangement (all these depending on precursor material, temperature, impinging particles energy and flux, dissociation, ionization), which have been discussed in more detail in Refs. [9,28].

4.2. Comparison between Raman spectra of different carbon material types

Much of the confusion about Raman peak assignments probably comes from the misfit of quantum mechanics theory and general fundamentals, even though these formulations have contributed to significant scientific progress.

This concerns, for instance, the double resonance Raman scattering theory, the definition of atomic disorder and of the amorphous state, the origin of band broadening, Raman peak up-/downshift (compressive/tensile stress) and especially the so-called mislabeled D-disorder peak at $\sim 1350\text{ cm}^{-1}$ [28,103–105]. It is all the more confusing that this peak is close to the rhombohedral D diamond peak at $\sim 1330\text{ cm}^{-1}$ and hexagonal chair structure H6 diamond peak at $\sim 1325\text{ cm}^{-1}$ [31,80,81,93,94]. It is also confusing because carbon materials grown with different thin film deposition devices can correspond to composite material containing all sorts of substructures [66,67] (summarized in Fig. 1), with properties strongly dependent on their distribution and size.

Confusion also exists on the G-band assignment [62,78,103] originally said to correspond to the $\text{Csp}^2\text{--Csp}^2$ stretching mode, which in fact is the overlapping bands of different more or less stress shifted broader bands corresponding mainly to odd rings C5/C7 ($\sim 1520/1550\text{ cm}^{-1}$) [108], hexagonal sp^2 rings ($\sim 1580\text{ cm}^{-1}$) corresponding to the stationary phonon mode within such rings [28,109], $\text{Csp}^2\text{--Csp}^3$ ($\sim 1470/1510\text{ cm}^{-1}$) [61] and edge dangling

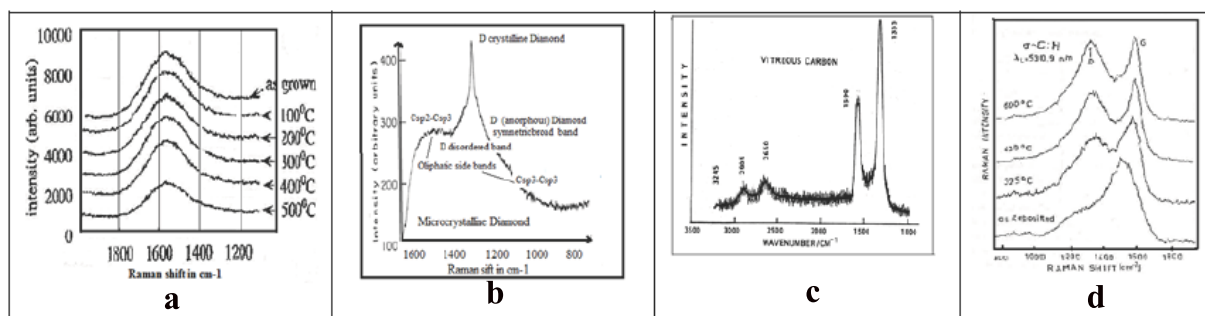


Figure 6. Raman spectra of (a) ta-C (Ta-C by Anders et al. [78] As grown (60 GPa, 80% sp³) ~ 50 cm⁻¹ stress upshift and disorder broadening of Csp²–Csp³, C5/C7 $\sim 1590/1610$ cm⁻¹. Csp²–Csp² ~ 1640 cm⁻¹. Few sp² clusters. Annealing 500°C less sp³ (40 GPa, 60% sp³), reduced stress), (b) Nano-diamond (nano-diamond by McNamara et al. [80]. Superimposed Diamond peak on amorphous diamond band (~ 1330 cm⁻¹), disordered T band (Csp³–Csp³ ~ 1100 cm⁻¹) and the so-called D-disorder band (~ 1350 cm⁻¹) (GeA-edge phonon being Raman active)), (c) Glassy carbon (Glassy carbon by Huang et al. [31]. Gpeak. 10 cm⁻¹ upshifted peak G and D diamond. Weak the so-called D-disorder (GA-edge ~ 1350 cm⁻¹) coherent with 2D peak ~ 2700 cm⁻¹. Stress shifted DG ~ 3000 cm⁻¹ Csp³–Csp²–Csp³ overtone of Csp³–Csp²)) and (d) a-C:H (a-C:H annealing by Wagner et al. [52] diamond appears ~ 1330 cm⁻¹, tensile stress reduced (H₂ exodiffusion) G peak getting sharp (sp² clusters in sp³ amorphous “diamond-like” matrix).

Csp²–Csp² (~ 1620 cm⁻¹) also IR active [110]. Therefore, the “true” G peak is only to be found for graphenic structure containing sp² cyclic rings.

Another point of confusion is that the same designation D is currently used for different structures: diamond (crystalline) and disordered (amorphous) diamond [68, 80, 111], D graphene (misabeled so-called D-disorder peak [103–105, 113]), DLC [30, 52, 62, 112] (an amorphous state which is a mix of sp² and sp³), crystalline defects, isotopes, impurities, interstitials, vacancies, dangling bonds, etc.). Raman spectra of different types of carbon material can show

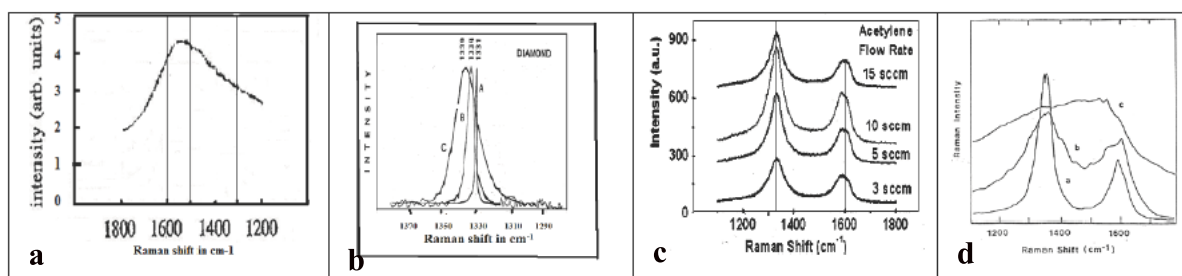


Figure 7. Raman spectra of (a) pseudo-amorphous graphite with few sp³ and amorphous graphite (GAC) (ion irradiated glassy carbon by Prawer et al. [112] ~ 15 cm⁻¹ stress upshift sp³ Diamond band and D-disorder (GeA cluster edge $\sim 1350/1360$ cm⁻¹. Max intensity GD band 1560 cm⁻¹ Csp²–Csp³. Weak G-band ~ 1600 cm⁻¹ (sp² clusters destroyed by irradiation). Similar to non-stressed amorphous graphite 100% sp² (Rouzaud [102]), (b) crystalline/amorphous diamond (D diamond by Huang et al. [111]. Results showing existence of amorphous diamond (symmetric band ~ 1330 cm⁻¹. Same frequency than ordered diamond peak. No G peak/band. No sp² cluster edge GeA band ~ 1350 cm⁻¹ \Rightarrow (no so-called D-disorder at 1350 cm⁻¹). No Csp³–Csp², no Csp²–Csp³), (c) carbon nanofiber (CNF by Lin et al. [69] G+ 1580 cm⁻¹, G⁻ (CNT intern walls 1560 cm⁻¹), main peak for H6 (hexagonal diamond 1325 cm⁻¹ (sp² transformed in sp³ on outer CNT wall during growth process (plasma). No Csp³–Csp² band (reduced amount only on interface between inner and outer part of CNW)), and (d) modified glassy carbon (Raman spectra glassy carbon N⁺ irradiated by Iwaki et al. [86] ~ 40 cm⁻¹ stress upshift G ~ 1610 cm⁻¹, GeA ~ 1390 cm⁻¹. Amorph. Diamond ~ 1370 cm⁻¹, sp³–sp² ~ 1510 cm⁻¹. Tensile stress downshift (~ 30 cm⁻¹ with N₂ exodiffusion). Similar to ta-C).

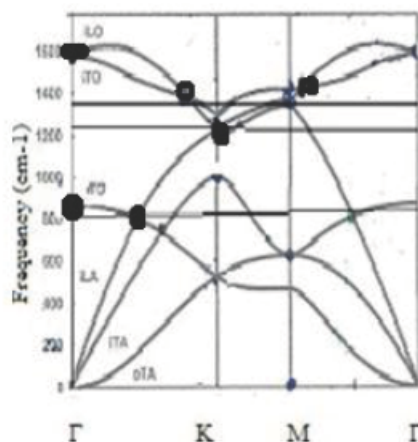


Figure 8. Phonon dispersion curves of graphene by Lazzeri et al. [109]. *G peak at 1580 cm^{-1} corresponds to double degeneracy in-plane phonon mode on Γ point (stationary vibration mode within hexagonal Csp²–Csp² cyclic ring). *The so-called D-disorder peak at $\sim 1350\text{ cm}^{-1}$ corresponds to a double degeneracy in-plane phonon mode on near K point (Coupled Double Resonance scattering on a symmetric A-edge Csp²–Csp² bond (external edge of graphene sheet or intern edge of voids in graphene)). *The so-called 2D peak at $\sim 2700\text{ cm}^{-1}$ corresponds to addition of D-disorder phonon (2K mode on A-edge), and in the bulk to 2 K and 2 M phonon modes Raman active (single M phonon mode at $\sim 1350\text{ cm}^{-1}$ is not Raman active).

paradoxically quite similar aspects, especially concerning “D” and “G” band, which, however, can be distinguished from their neighbors by looking at band broadening (disorder effect), stress shift and different kinds of atomic rearrangements. The Raman spectra in Fig. 6, corresponding to references [31,52,69,86] can be compared with those in Fig. 7 to some extent and corresponding to [102,112,69,111,86].

It was shown long ago that the D band cannot account for sp³ concentration in carbon material. For DLC material containing some significant amount of sp² it is shown that the ID/IG ratio (integrated intensity of D and G-band) is proportional to number and size of graphitic crystallites [30]. Those appear during annealing of crystalline diamond above $\sim 800/900^\circ\text{C}$ [31,61], the size of which depends on annealing temperature and time, because graphite is the thermodynamic carbon ground state. No the so-called “D-disorder” band is observed in large grain polycrystalline graphite and crystalline graphite particles [31,61], meanwhile it is observed for small graphite dust particles [114]. It is therefore necessary to know what the so-called D-disorder peak in reality is, in revisiting Raman spectrometry fundamentals.

4.3. General aspects of Raman fundamentals

4.3.1. Classical and quantum mechanical description of Raman scattering

Raman theory based on classical description are reviewed in many published works [115] and has been refined with quantum mechanical aspects involving photon/electron/phonon scattering and with which ordered crystalline structures such as diamond, graphene, CNT could be characterized [28,104,105].

Specific phonon modes diamond [81] and graphene [104] crystalline material can be determined with their wave vector direction, which has been defined with phonon dispersion curves in the reciprocal space. Figure 8 shows the dispersion curves for graphene (by Lazzeri et al. [109]) for many DLC materials where sp² clusters are nothing other than graphene.

4.3.2. Role of stress and atomic disorder on Raman shift and band broadening

In a more complex and disordered structure [116], the number of phonon modes is much higher. However, considering the duality between quantum mechanical representation and classical vibration mechanics, the atomic vibration modes which govern the Raman effect can be qualitatively described with some anharmonic oscillator composed by two atoms of the same mass with interatomic energy potential $U = \alpha x^6$ and force constant $K = 2\alpha x^{-4}$ [117]. Considering that Force constant K is shifted by ΔK by internal stress σ , and phonon frequency is shifted by: $\delta\omega/\omega_0 = \sigma(1 - \nu)/E_0$ (Pauleau formula) [90] (ν is the Poisson coefficient, E_0 is the mean elastic constant) this shows that:

*The Raman shift is proportional to internal stress.

In amorphous (disordered) material, the interatomic distance is $x_i = x_0 + \delta x_i$ (δx distortion) and interatomic energy potential $U = \alpha x^6$ [117] the strain δx_i distribution corresponds also to phonon frequency shift $\delta\omega_i$ distribution with $\delta\omega_i/\omega_0 = \eta\delta x/x_0$ [28]. Therefore:

*Band broadening is always associated to atomic disorder.

Frequency well-defined Raman peak \Rightarrow ordered material structure (constant interatomic bonds).

4.3.3. Locality of scattering event and confinement effect

Raman shift anomalies have been generally considered as the consequence of “confinement” of phonon and electrons on edges and smaller particles by modification of their electronic orbital environment [89,103,104,113,118].

However, experimental results are not always in accordance with such calculated and predicted effects. Furthermore, a local phonon vibration mode has been shown with micro Raman on graphene A-edges corresponding to the so-called D-disorder peak ($\sim 1350 \text{ cm}^{-1}$) [119,120]. This can also be deduced from the graphene phonon dispersion curves in the reciprocal space (Fig. 8) [28] for the G Raman peak corresponding to the Γ point at 1580 cm^{-1} , which corresponds to some stationary phonon vibration mode within the hexagonal cyclic sp² ring. Recall that the wave vector direction in the reciprocal space corresponds to a propagation wave direction in real space. On the Γ point of these curves phonon wave vector direction is perpendicular to the graphene plane for which no phonon wave propagation perpendicular to the plane can exist.

The confinement effect in smaller sp² clusters based on a Quantum Mechanical calculation appears to be overestimated, when predicted Raman shifts [118] can be also interpreted with other more likely effects [104,28]: as grown a-C:H can be differently stressed (compressive stress or tensile stress) depending on which depositing process has been used (temperature, ion peening, stress relaxation):

- (1) Tensile stress can appear during thermal treatment of a-C:H (denser sp³ rearrangement and exodiffusion of H₂) which can then be relaxed [52].
- (2) Compressive stress can appear in consequence of growth of sp² clusters which have lower atomic density (higher volume) than their surrounding amorphous diamond-like material.
- (3) Continuing the annealing process, compressive stress will be relaxed. The confinement effect is also overestimated as shown with sp² cluster optoelectronic gap calculation [89], which is much higher than experimentally measured.

4.3.4. Double resonance theory and phonon backscattering on edges and defects

According to the double resonance (DR) theory based on successive Raman scattering events in sp² clusters and graphene flakes, in addition to the law of energy conservation, the law of impulse conservation has to be fulfilled [113].

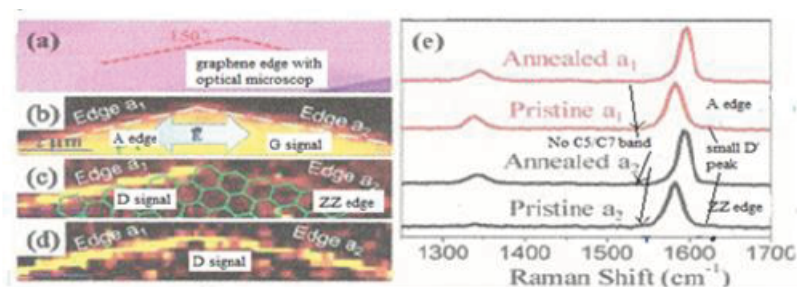


Figure 9. Micro Raman experimental results showing graphene ZZ edge transformation into A-edge with annealing at $\sim 300^\circ\text{C}$ adapted from Xu et al. [119]. No C5/C7 band at $\sim 1490/1530\text{ cm}^{-1}$. Tensile stress downshift $\sim 15\text{ cm}^{-1}$ on pristine material. The so-called D-disorder peak at 1350 cm^{-1} localized on external A-edge. D indicates spots in the bulk corresponding to internal A-edge of voids. D' peak (corresponding to edge dangling Csp²–Csp²) is reduced with annealing at $\sim 300^\circ\text{C}$.

In fact, only the latter is achieved in considering some phonon backscattering on edges and defects [104,28]. Looking at existing phonon modes at $\sim 1350\text{ cm}^{-1}$ it appears that the so-called D-disorder Raman E effect can be interpreted in terms of phonon backscattering on ordered A-type (symmetric Armchair) graphene edges, and is therefore mislabeled. This is in agreement with micro-Raman analysis [119,120] (Fig. 9), and also with the point that the corresponding GeA Raman signal is not observed for larger crystallites for which the edge Raman signal is smaller than the background noise of larger bulk material (where that volume/surface ratio is increasing) [28].

The usual quantum mechanic formalism is with delocalized phonons and interprets Double-Resonance backscattering in term of “intra-valley” and “inter-valley” scattering events [103–107] corresponding to adjacent Brillouin zones. However, looking more closely at the energy balance, it appears that this model violates the law of energy conservation. Therefore, a better coherent Couple Double Resonance (CDR) theory model has been developed [28] that obeys the energy conservation law and is based on locality and classical/quantum mechanics dual representation of electron and phonons.

With a short distance between paired electron/hole (Kohn effect) and the important difference of scattering time of the interacting photon, electron and phonon, a CDR backscattered phonon can be either absorbed by an activated electron or by a corresponding valence band hole. This effect is thought to account for Raman Effect coupling and resonance between different phonon modes and overtone modes explaining the dependence of Raman signal with different orientation of polarized laser light, and how the corresponding Raman signal can be local [28].

This model accounts for micro-Raman results of the so-called D-disorder Raman peak and its locality on symmetric A-edge (Armchair shape edge) graphenic materials (including sp² clusters in DLC). The equivalent CDR Raman peak is not observed on graphene materials such as hexagonal Boron Nitrogen material (hBN) [121] for which A-edge does not correspond to a symmetric oscillator. However, such A-edge can also exist internal to graphenic bulk material in vacancies and voids in agreement with experimental observations on CNT [122,123]. Therefore, such so-called “D-disorder” peak (corresponding to Raman CDR phonon back scattering) can also be observed in the middle of graphene and CNT surface containing vacancies (Fig. 10) corresponding to Raman spectra of Ar irradiated graphene (according to Dresselhaus et al. [105]).

This illustrates a point contrary to the abstract quantum mechanical interpretation with inter valley Raman transition, the sharp D peak at $\sim 1350\text{ cm}^{-1}$ has in fact nothing to do with disorder but corresponds to CDR of K phonon being backscattered on well-ordered symmetric A-edges. Ar⁺ ion bombardment of a graphene sheet first creates vacancies and voids (geometric holes in the graphene plane), for which the D and D' peaks stay sharp (ordered edge structure on which dangling Csp²–Csp² have been formed). Disorder only appears with high Ar ion irradiation with

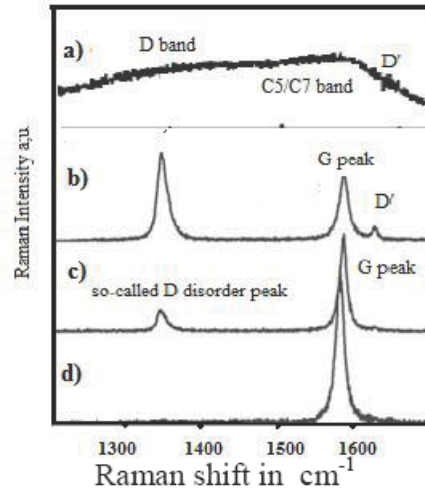


Figure 10. Argon ion irradiated graphene By M.S. Dresselhaus et al. [105]. Disorder band broadening appears only for high ion doses and mislabeled so-called D-disorder peak corresponds in fact to well-ordered GeA-edge. (a) Ion dose $>10^{15}$ producing disordered Graphene. Stress up shifted so-called D-disorder broad band, broad C5/C7 band and broad G-band. No stress shifted broad D' band (disordered edge Csp2–Csp2 dangling bonds). (b) Ion dose 10^{12} . Intense so-called D peak. No peak broadening on D and G peaks. No C5/C7 band. No stress up-shifted D-disorder band and G peak. No stress shifted D' band (edge Csp2–Csp2 dangling bonds). Holes produced by Ar+ impact with intern edge Csp2–Csp2 dangling bonds in ordered graphene material. (c) Ion dose 10^{11} . Sharp $G \sim 10\text{cm}^{-1}$ compressive stress upshift. Few holes (voids) produced by Ar+ impact and few Csp2–Csp2 dangling bonds on void internal edges. For ion dose $< 10^{11}$ no defect formed. Non-stress shifted intense G peak. Considering the strong interlinking carbon bonds ($\sim 7\text{ eV}$) higher incident ion energy and higher ion dose are necessary to produce atom removal in defect free graphene.

Table 3. Revised nomenclature for main carbon Raman peaks.

Raman (cm^{-1})	Peak/band	Type of structure	Energy in eV type of structure
~ 1330	D-peak	Ordered diamond cubic	Csp3–Csp3
~ 1325	DH6 peak	Ordered hexagonal diamond	~ 7.02
$\sim 1200/1400$	Dd band	Amorphous diamond, ta-C	~ 7.015
~ 1150	DD	Csp3–Csp3 edge bonds	Aliphatic Csp3–Csp3
~ 1470	DG	Csp3–sp2cluster edges	Aliphatic Csp3–Csp2
~ 1580	G-peak	Stationary sp2 hexagonal ring	Csp2Csp2 $\sim 7.03\text{ eV}$
$\sim 1560/1620$	G-band	Atomic disorder broadening	Superposed GG, DG GC5/GC7
~ 1620	GG	sp2 clusters edge bonds	Csp2–Csp2
~ 1470	DG	sp2 on sp3 cluster	Csp2–Csp3
~ 1520	GD	sp3 on sp2 cluster	Csp3–Csp2
~ 1530	GC5	C5 ring	Fullerene C5 mode 1550 cm^{-1}
~ 1550	GC7	C7 ring	(upshift by plane curvature)
~ 1350	Ge _A	Graphene A-edges edge	External /internal A-edge 0° CDR
$\sim 1300/1400$	Ge _A band	Broadening by edge disorder	$\sim 7.03 \pm 0.01\text{ eV}$
~ 2690	G2P	2 phonons GeA graphene CDR	In plane 2K/2M phonon modes
~ 150	RBM	CNT	Breathing mode (\sim radius)
~ 1600	G ⁺	CNT in plane longitudinal	G Stationary mode
~ 1560	G [−]	CNT in plane transversal	Curvature Csp2–Csp2

overlapping impact zones and it corresponds to important Raman band broadening.

Considering the confusion about the designation and assignments of Raman peaks and bands which have often appeared in papers published about carbon research, we have proposed some new Raman nomenclature to facilitate carbon material engineering [41] (Table 3).

5. Necessary Conditions for a Bethe Nuclear Reactor Concept

5.1. Temperature-dependent atomic rearrangement activated by H_2 recombination

When the solid state material temperature is sufficient ($T > 300^\circ\text{C}$ for carbon material) [74], trapped H atoms can diffuse and recombine to form H_2 with high energy release, and can contribute to phase transformation in favor of diamond and a diamond-like structure with quantum electronic activation. This is endothermic and thus, it forms a metastable structure. Meanwhile, when less quantum electronic activation is available, thermal atomic rearrangement in favor of graphite ground state will prevail (exothermic).

Therefore, temperature, material composition and structure dependent atomic rearrangement is to be considered which can be driven upon the structure of desired packing density and electronic distribution [29]. It should be mentioned here that this is also the case for other materials with higher 3D electronic orbitals, for instance, where a more complex electronic orbital distribution have been calculated [42,43,54,63,124] — such as for Cr, Fe, Co, Ni, Cu, Pd, and Ta, having different oxidation states and different s–p–d hybridization states. These can have (roughly described) either hexagonal or cubic structure (including PdH_x , NiH_x , Si, and BN, for instance) and the diffusion and ion penetration depth depend on the structure and relevant orientation [27,47,57,64,65,121,124].

Thermally induced graphitic sp^2 degradation of a diamond-like carbon target with heat produced by the p^+ ion flux/target discharge can be compensated with quantum electronic activated sp^3 rearrangement with H_2 chemical recombination and neutralization energy release (similar to diamond growth in H_2 /hydrocarbon gas mixture plasma at temperature $> 500^\circ\text{C}$), which can then maintain the original denser disordered/amorphous diamond structure (with some electric conduction properties obtained with B and/or N doping for instance).

Compressive stress with specific local geometric distribution can be produced by different means. These can be exerted particularly on interstitial atoms by their neighboring atoms getting closer to each other with sp^3 atomic rearrangement, for instance with ion implantation and ion peening effect (such as He^+ , C^+ and CH_x^+) [9,10] when they have sufficient energy (> 20 eV for C ions). The latter effect is not observed when the impinging ion has few eV of energy [20,46,68] and are much smaller (p^+ having $\times 1000$ lower size than atoms).

Heat favors the growth of larger stacks of sp^2 clusters and graphite micro crystallites of lower atomic packing density and therefore, can also produce compressive stress [29,52], because graphite has ~ 1.5 lower packing density than diamond, so this can produce volumetric expansion with such graphitic atomic rearrangement. Therefore, the incorporated H atoms with neutralization of implanted H^+ can be subject to compression with the neighboring atoms up to several 100 MPa, when the diamond is transformed into graphitic material [31,60] (before being thermally relaxed). Considering also ta-C:H produced with some biased plasma depositing [79] for instance and transformation of glassy carbon into harder and denser ta-C with high energy N^+ irradiation [87], H atoms will also be submitted to compressive stress (up to 1000 MPa especially when He^+ is implanted) [76].

However, this compressive stress will only correspond to compressive energy in the 1–10 eV range. That is quite small in comparison to compression energy of about 1–10 keV which is necessary for C/ p^+ nuclear fusion reaction.

5.2. Chemical properties of substrate material

Dissociation of the H_2 precursor gas has to be achieved either by dissociation with catalytic material (such as boron [9,76] and porous AlNi Raney Nickel [125]), or within arc and plasma discharge [11–13,17,21,22]. However, hydro-

gen can also form low energy chemical bond hydrides [47,63,124] which can be released with heat. From nuclear technology, it is known that materials should be of particular purity (graphite for instance) [126] to avoid any parasite nuclear radiation and absorption and contamination, which might affect the nuclear reaction efficiency.

It should be mentioned here that other non-nuclear chemical reactions releasing energy may be superposed on some nuclear reaction (a hypothesis considered by Fleishman and Pons when they proposed a cold fusion nuclear reaction for the first time [127]).

Nuclear reaction artifacts can be caused by contamination with same products other than those resulting from nuclear reactions. For instance Cu which is always naturally associated to Nickel and difficult to remove with usual Ni metallurgy [128] or Fe residual contamination which can result from high density plasma stainless steel reactor wall erosion like those used for large area depositing and parasite low concentration doping has to be avoided [14–16]. This may be neglected when considering etching (e.g. diamond processing) [17,18].

5.3. Solid state structure

Nuclei having a solid state nuclear fusion potential must have the possibility of being brought in close contact to each other. This is particularly true for low mass material which can more easily diffuse in a solid-state substrate, such as protons and dissociated H atoms [9,47,56]. Dense carbon materials with reduced defects (vacancies) such as graphene, H6 sp³ hexagonal chair diamond, crystalline rhombohedral (cubic) diamond, ta-C (amorphous diamond) and hard glassy carbon (whenever containing pores) have high diffusion barrier properties for H atoms and H₂ molecules [10,41,47,49], in contrast to protons which diffuse even through defect free graphene corresponding to densest diffusion barrier carbon material [51].

Proton diffusion lengths are particularly important for some diamond crystalline orientation offering the so-called “string” channeling capabilities [34–37], much higher than for graphite *c*-axis [38,46], meanwhile p⁺ planar channeling in interplane space between dense hexagonal graphenic planes (MWCNT) is paradoxically much lower because subject to spatial periodic oscillation induced by electron exchange depending on ion energy and initial ion trajectory orientation [39,40,51,129] (this is different from H neutral atoms which can easily diffuse in interplane space between dense sp² hexagonal graphenic planes) [64,40].

With long range channeling (μm range at room temperature), only a few collisions with carbon nuclei occur. However, channeled H⁺ can be scattered by phonon vibration transverse to the H⁺ channeling direction similar to what exists with electron channeling and the normal electron conduction mode in conducting solid states. This sort of ion scattering is phonon density (temperature) dependent [130,131] and can strongly reduce the channeling length and enhance the proton electron exchange, which reduces the arriving proton energy [32–38].

In disordered composite and amorphous graphitic carbon structures, where no diffusion channels exist (other's than proton energy losses with electron scattering) the implantation depth is much lower (although having lower atomic packing density) and nevertheless reaches the 1000 nm range for 5 keV H⁺ [26]. This explains a priori why dense tetrahedral amorphous carbon (ta-C) is expected to have the highest proton/carbon nucleus collision efficiency. However, in such cases ~80% of impinging proton energy is lost with electron scattering and only ~10% with atomic core scattering [20,32,33], in contrast to hot plasma conditions where colliding particles are mainly composed of the nucleus with no close electronic environment. Therefore, the Lawson criteria [132] that determines optimized conditions of nuclear collisions in hot plasma are not applicable to a nuclear collision in the solid state.

Considering that no nuclear reaction has been observed with p⁺/carbon solid state material (we have mentioned in Section 1 and what might have been also consequence of weak proton flux used and reduction of the proton energies with electron and phonon scattering), the first defined conditions may be not be sufficient for the achievement of a Bethe–Weizsäcker fusion reactor. It will be probably necessary to look at the nuclear collision process itself and at any

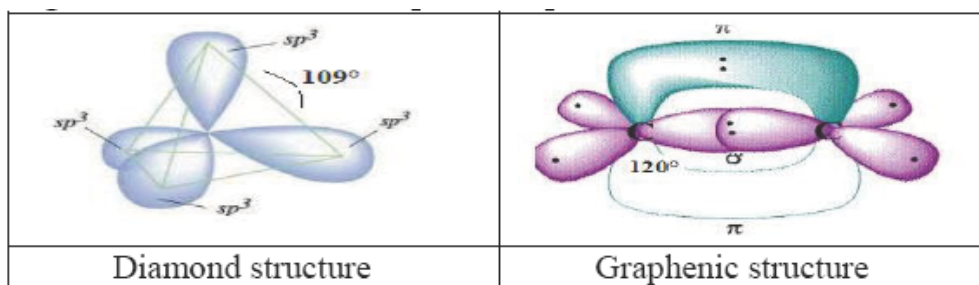


Figure 11. Electron free space for p^+ /carbon nucleus collision.

other effects which may facilitate or hamper the nuclear reaction and the overstepping of the nuclear electrostatic barrier.

6. Nuclear Reaction Efficiency

6.1. Electronic orbital screening

It has been shown with laser driven p^+ /boron nucleus collisions that the nuclear reaction efficiency is strongly increased when the solid-state boron target surface is transformed into a dense boron plasma, and a significant amount of electrons have left the plasma [7]. However, not all electrons have been stripped off from the boron ionic core. At least 1S electrons are left which apparently has little effect on the p^+ /boron nuclear reaction efficiency. It is suggested that a similar situation exists for solid state carbon.

Independent from the reduction of proton energy with electron and phonon scattering (described in Section 3), the anisotropic distribution of sp^2 and/or sp^3 electronic orbital for which some geometric open space will be left between zones where the electron probability presence is reduced (Fig. 11). Better nuclear reaction efficiency is expected with a dense structure which offers direct access to the atomic nucleus through the electron empty zones.

Amorphous sp^3 carbon belonging to a dense atomic structure with large 109° electron open space around the nucleus appears to be the best candidate. Minimum energy reduction of arriving p^+ is provided for a corresponding solid angle. Thus, H_2 chemical recombination energy release activating sp^3 atomic rearrangement in ta-C heat degraded (graphitic) is expected to restore the sp^3 carbon material structure which favors p^+ /carbon nucleus interaction (as long as no crystalline structure is formed and no channeling effect appears).

In addition to these electron depletion zones, some electron stripping of the target solid state carbon material occurs with the photo-electric effect. This is expected to be achievable with a dense luminescent cold plasma working in a pulsed mode, especially when adding some rare gas in the hydrogen plasma in favor of hydrogen gas activation and ionization.

6.2. Proton–carbon nucleus collision cross section

In contrast to longitudinal phonon vibration (stretching modes), transverse phonon C–C vibration (bending modes) which are nearly perpendicular to the arriving fast proton direction can accelerate the proton up to $\sim 2 \times 10^5$ eV (proton–electron collision energy when both particles have been accelerated with their electrostatic attraction [133]), before being slowed down in the space between 1S orbital and nucleus (Fig. 12).

This effect is only to be considered with a classical model for which the proton dimension is ~ 1000 times smaller than the 1S orbital dimension (Bohr radius) [134] and where no negative electric charge exists at the center of 1S

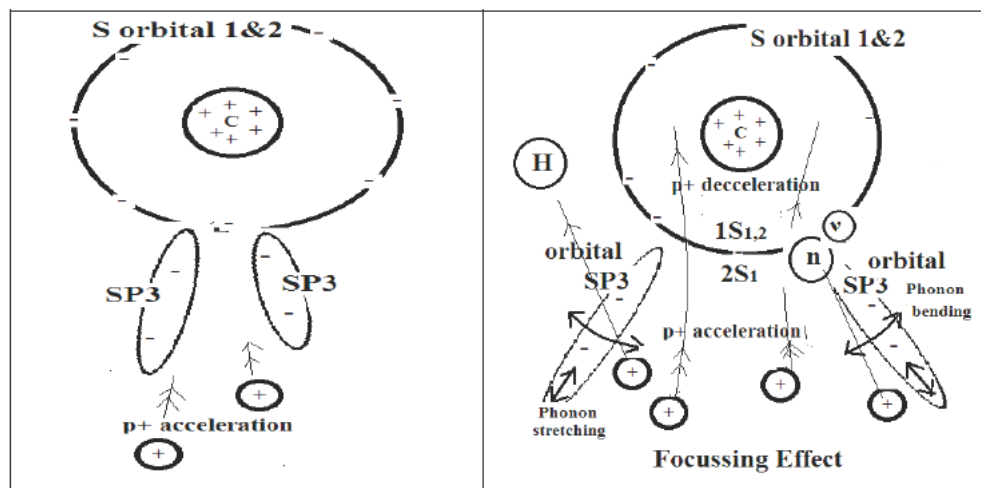


Figure 12. Scheme for p^+ defocussing when synchronic to bending phonon mode.

orbital.

An electrostatic lens defocusing effect of p^+ toward the carbon nucleus is expected, which is stronger than with the quantum mechanical model, because the S electronic orbitals are uniformly distributed over a sphere being superposed to the nucleus zone [42,43]. (It should be noted that the QM description of electron density in the S orbital center does not fit with atomic physical common sense.)

This effect is expected to decrease the p^+ /carbon nucleus collision efficiency insofar as the flux of arriving p^+ with a larger solid angle can collide with a lower probability to hit a carbon nucleus (Fig. 12]. Protons will then be slow down and form a hydrogen atom. However, electron capture transforms a proton colliding with an electron in a neutron/neutrino pair which are not affected by the electrostatic barrier [8,135] and which therefore can react with the nucleus in favor of a more deformable electrostatic barrier of a carbon nucleus.

6.3. Anharmonic resonance of electrostatic barrier with phonon/nuclear interaction

Light atoms subject to nuclear fusion (such as He, Li, and Be) have an isotropic spherical electronic environment (1S and 2S electronic shells) which will not significantly modify their nuclear structure, all the more so because strong nuclear binding forces preserve high nucleus rigidity [8,135]. In contrast to heavier elements containing a higher number of charged particles, where the distributed electrostatic repulsion forces weaken the strong force cohesion energy in accordance with the observable Moessbauer effect [42,43], and show nuclear geometric and energy band structure dependence from environmental electronic distribution.

For boron and carbon materials where the 2S/2P electronic orbital can be sp^2 and sp^3 hybridized with important anisotropic distribution, it is believed that modification of the nuclear electrostatic barrier shape can be more significant than with smaller atoms having only spherical S orbitals. Static anisotropic distribution of the carbon electronic orbitals is expected to be at least able to induce some weak anisotropic deformation of the nuclear electrostatic barrier height [6] (Fig. 13). This will not significantly modify the fusion energy threshold. This is also the case with phonon vibration and electronic oscillation [129,130] which induce nucleus oscillation.

However, in the calculation of the anharmonic resonance effect, it has been predicted that some enhanced tunneling effect occurs during a nuclear collision [136]. Anharmonic resonance between specific phonon vibration modes and a nuclear electrostatic vibration mode may be achievable, considering the multipolar electrostatic configuration of a carbon nucleus and the non-linear electrostatic interaction between electrons and nucleus. With such resonant phonon/nuclear coupling it is then expected there will be a higher vibration amplitude of the nuclear electrostatic barrier.

Similar to the synchronic gating effect of phonon/conduction electron transport mechanism with which superconductivity can be described [130], a proton can more easily move through the oscillating electrostatic barrier when its displacement is synchronic to some specific phonon vibration, corresponding to a tunneling effect enhancement. This is what is to be qualitatively expected with ta-C carbon sp^3 longitudinal and transversal phonon vibration frequency ($1100/1400\text{ cm}^{-1}$ range) and arriving p^+ velocity (1 keV energy range) corresponding to displacement velocity $\sim 10^5\text{ m/s}$ and interatomic bypassing frequency $\sim 10^{15}$. These phonon vibration frequencies phonon can be activated with VIS/UV radiation ($\sim 5\text{ eV}$). Meanwhile at this stage no quantitative detailed results can be obtained with usual abstract quantum mechanical formalism.

Therefore, it is suggested that we look at some improved wave physical description of involved particles with can give clearer insight into the nuclear electrostatic barrier tunneling mechanism with which p^+ can more easily step across the electrostatic nuclear barrier.

7. Perspectives on Improved Physical Description of Quantum Mechanical Effects

Many results predicted with the abstract Quantum Mechanical formalism have been in agreement with experimentally observed effects. However, questions appear when more complex systems are considered, especially questions about the physical nature of the particle/wave duality [137]. Several unanswered questions remain, for instance, the origin of the limited absolute light velocity and significance of mass/energy equivalence, electric charge and different fields beyond the observed effects for which different concepts have been defined [138]. Examples can be given with the failing physical description of single particle interference effects [139]; physical description and material specificity predictions about superconductivity [140]; Raman double resonance theory where the so-called mislabeled D-disorder Raman peak is interpreted [103–105]; intrication phenomena and anomalous compressibility of condensed matter [141]; and the tunneling effect for colliding particles when no barrier width is considered [8]. Other questions arise

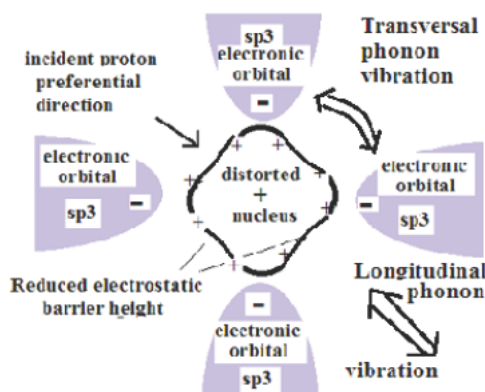


Figure 13. Scheme of electrostatic nuclear barrier distortion with 109° open space sp^3 orbital.

about the predicted existence and properties of cubic C₃N₄, which is supposed to have higher hardness than diamond [86,142] and about the existence of the so-called graphane material [93–98].

Roughly summarized, here is what we propose to be developed in more detail elsewhere. We suggest the main cause of many QM failures is linked to the arbitrary association of an abstract wave function which for many more complex subjects do not correspond to any usual physical wave [137,143], and that the time-dependent evolution of particles described with the Schrödinger equation is based on an approximate dual wave/particle physical description, which can sometimes lead to absurd conclusions, for instance the Schrödinger cat paradox, in which the cat is alive and dead at the same time; or more prosaically when the so-called D and D' disorder peaks in graphene are interpreted as abstract quantum mechanical effects, in contradiction with elementary observable solid state physical effects [28,105]. Several aspects of quantum mechanical fundamentals have also been questioned with more general theoretical consideration [144]).

It is then suggested that instead of a vacuum, some elastic non-viscous aether exists, which has variable density of cohesion energy (potential energy) and where local perturbation can generate waves with light propagation velocity according to formulae $c = \sqrt{(k/\rho_0)}$ and considering density of cohesion energy is equivalent to mass density and considering that density of thermal energy (nkT/volume) is defining the pressure of an ideal gases. It is known how wave packets formed with waves of different phase can have group velocity V_g , and considering their mean wave energy density amplitude A , some intrinsic wave packet energy can be defined with $E_{pk} = \frac{1}{2}kA^2 = mc^2$ defining mass m and kinetic energy $E_c = \frac{1}{2}mV_g^2$. Particle size is defined with the volume occupied by wave-packet wave length and energy wave amplitude in a 3D vortex (Eddy). 3D fluid dynamics [145] and wave oscillating modes with longitudinal and transversal modes for which complex mathematical treatment will have to be developed, similar to what has been developed with atmospheric phenomena and 3D wave modelling in liquids [146,147]. With such a model, nuclear particles could no longer be considered in terms of association of sub-particles sticking together with mysterious weak and strong cohesion forces, but resulting from a split of original larger particle wave packets having its own size, mass and electric charge. This model is then expected to provide some physical description of nuclear tunneling effects, enabling us to sort out optimized solid state nuclear reaction conditions.

8. Conclusions

With this analysis, we have shown some of the expected feasibility of a solid state Bethe CNO cycle solid state nuclear fusion reactor for the specific structure of amorphous tetrahedral carbon (ta-C), which is:

- (1) A particularly dense material which can be regenerated with the proton flux.
- (2) In an amorphous state with which atomic core scattering along μ m proton implantation depth range (for 1 keV range proton energy) can be kept significant in comparison to electronic exchange which reduces the arriving proton energy.

The theoretical ratio of produced/consumed energy appears to be in the range of 10–100 when no electronic screening remains during the nuclear collision process, comparing the conditions of proton/carbon nucleus reaction with similar proton/boron reaction results. Uncertainty remains about transposing proton/boron results to proton/carbon reaction with a lower nuclear reaction energy threshold. This uncertainty is expected to be cleared up with similar experiment with a laser driven proton/boron reaction. The collision and fusion efficiency is expected to be improved with phonon/proton interaction and phonon/nucleus anharmonic resonance with which a proton flux – being synchronic to coupled phonon/nuclear electrostatic vibration – can more easily get through the nuclear electrostatic barrier. At this stage, it appears the limitation of conventional quantum mechanical formalism which fail to produce better physical insight into the wave structure of subatomic particles, and with which different wave interference mechanisms and the nuclear electrostatic barrier tunneling effect might be clearly sorted out.

Considering that abstract quantum mechanical formalism has also failed in many other ways, we suggest revisiting fundamentals with a new separate investigation on some aether model with which 3D fluid and wave mechanics can give account of all acquired data with a dual wave/particle description QM particle/wave duality. This should also give clearer insight into the interference mechanisms and nuclear electrostatic barrier tunneling effect. Meanwhile experimental investigation into this phenomenon will have to be organized.

References

- [1] G. Mondet, Thesis. Propriétés radiatives des plasmas de fusion. Emissivité et opacité dans des structures atomiques complexes, Université Paris Sud - Paris XI, France, 2013.
- [2] M.R. Gomez, S.A. Slutz, A.B. Sefkow, D.B. Sinars, K.D. Hahn, S.B. Hansen, E.C. Harding, P.F. Knapp, P.F. Schmit, C.A. Jennings, T.J. Awe, M. Geissel, D.C. Rovang, G.A. Chandler, G.W. Cooper, M.E. Cuneo, A.J. Harvey-Thompson, M.C. Hermann, M.H. Hess, O. Johns, D.C. Lampa, M.R. Martin, R.D. McBride, K.J. Peterson, J. L. Porter, G. K. Robertson, G. A. Rochau, C. L. Ruiz, M. E. Savage, I. ?C. Smith, W. A. Stygar and R. A. Vesey, Experimental demonstration of fusion-relevant conditions in magnetized liner inertial fusion, *Phys. Rev. Lett.* **113** (2014) 155003.
- [3] H.L. van der Horst, VIIIc Neutron Generators, gas-discharge tubes, Philips Technical Library **16**. Eindhoven, Netherlands, Philips Technical Library (1964) 281–295.
- [4] J. Reijonen, Compact neutron generators for medical, homeland security, and planetary exploration, *Proc. 2005 Particle Accelerator Conference*, Knoxville, Tennessee, pp. 49–53.
- [5] J.M. Elizondo-Decanini, D. Schmale, M. Cich, M. Martinez, K. Youngman, M. Senkow, S. Kiff, J. Steele, R. Goeke, B. Wroblewski, J. Desko and A.J. Dragt, Novel surface-mounted neutron generator, *IEEE Trans. Plasma Sci.* **40** (9) (2012) 2145–2150.
- [6] J. Huizenga, N. Ramsey, A.J. Bard, N. Hackerman, S.E. Koonin, J. Bigeleisen, J. Landis, H.K. Birnbaum, P. Lipman, M. Boudart, B. Miller, C.F. Callis, D. Nelson, M. Desselhaus, J. Schiffer, L. Faulkner, J. Schoettler, T. K. Fowler, D. Stein, R.L. Garwin, M. Wrighton and J. Gavin, Cold Fusion research, A Report of the Energy Research Advisory Board to the United States Department of Energy (1989) DOE/S-0073 DE90 005611.
- [7] C. Labaune, C. Baccou, S. Depierreux, C. Goyon, G. Loisel, V. Yahia1 and J. Rafelski, Fusion reactions initiated by laser-accelerated particle beams in a laser-produced plasma, *Nature Commun.* **4** (2506) (2013).
- [8] K.S. Krane, *Introductory Nuclear Physics (Bethe cycle)*, Wiley, New York, 1988, p. 537.
- [9] S. Neuville and A. Matthews, *Thin Solid Films* **515** (2007) 6619.
- [10] R. McKenzie, D. Muller, B.A. Pailthorpe, Z.H. Wang, E. Kratchinskaia, D. Segal, P.B. Lukins, P.D. Swift, P.J. Martin, G. Amaratunga, P.H. Gaskel and A. Saeed, *Diamond and Related Materials* **1**(1) (1991) 51.
- [11] B.K. Tay, X. Shi, L.K. Cheah and D.I. Flynn, *Thin Solid Films* **308,309** (1997)199.
- [12] A. Hurkman, D.B. Lewis and W.-D. Münz, *Surf. Eng.* **19** (Part3) (2003) 205.
- [13] C. Corbella, I. Bialuch, M. Kleinschmidt and K. Bewilogua, Modified DLC coatings prepared in a large-scale reactor by dual microwave/pulsed-DC plasma-activated chemical vapour deposition, *Thin Solid Films* **517**(3) (2008)1125–1130.
- [14] M. Liehr, F. Fendrych, A. Taylor and M. Nesládek, Routes towards large area, low pressure nanodiamond growth via pulsed microwave linear antenna plasma chemistry, *MRS Proceedings*, Vol. 1282 (2011). DOI: <https://doi.org/10.1557/opl.2011.524>.
- [15] A. Kromka, O. Babchenko, T. Izak, K. Hruska and B. Rezek, Linear antenna microwave plasma CVD deposition of diamond films over large areas, *Vacuum* **86** (2012)776–779.
- [16] H.A. Mehedia, J. Acharda, D. Rats, O. Brinza, A. Tallairea, V. Millea, F. Silva, C. Provent and A. Gicquel, *Diamond and Related Materials* **47** (2014) 58–65.
- [17] S.J. Pearton, A. Katz, F. Ren and J.R. Lothian, ECR plasma etching of diamond, *Electronics Lett.* **28** (1992) 822.
- [18] D. T. Tran, T.A. Grotjohn, D.K. Reinhard and J. Asmussen, Microwave plasma-assisted etching of diamond, *Diamond and Related Materials* **17** (4–5) (2008)717–718.
- [19] R.A. Dandl, J.L. Dunlap, H.O. Eason, P.H. Edmonds, A.C. England, W.J. Herrmann and N.H. Lazar, Electron cyclotron heated “target” plasma experiments, Plasma Physics and Controlled Nuclear Fusion Research, *Proc. Third Int. Conf. Plasma*

- Physics and Controlled Nuclear Fusion Research*, Novosibirsk, USSR (Russian Federation), 1–7 Aug. 1968. International Atomic Energy Agency, Vienna (Austria), Vol. II, No. 3, 1969, pp. 435–447, IAEA-CN-24/J-6; ISSN 0074-1884.
- [20] Andre Anders (Ed.), *Handbook of Plasma Immersion Ion Implantation and deposition*, Wiley, New York, 2000, ISBN 0-471-24698-0.
- [21] A.A. Galeev and R.N. Sudan (Eds.), *Basic Plasma Physics I. Volume I of Handbook of Plasma Physics*, North-Holland, Amsterdam, New York, 1985.
- [22] J.A. Bittencourt, *Fundamentals of Plasma Physics*, Springer, Berlin, 2004. ISBN 9780387209753.
- [23] S.M. Pfothenhauer, O. Jäckel, A. Sachtleben, J. Polz, W. Ziegler, H.P. Schlenvoigt, K.U. Amthor, M.C. Kaluza, K.W.D. Ledingham and R. Sauerbrey, *New J. Phys.* **10** (2008) 033034 (14pp.).
- [24] J. Winter, *J. Nucl. Mater.* **131**(1987)145–147.
- [25] J.P. Coad, A.S. Kaye, C. Walker, A.J. Avery, D.J. Diskett and R.E. Walker, EMRS Meeting XVII, Proceedings by P. Koidl and P. Oelhafen, Les Editions de la Physique (Eds.) (1987) 417.
- [26] J. Eck and M. Balat-Pichelin, *Vacuum* **85**(3, 24) (2010) 380–389.
- [27] M. Balat-Pichelin, J. Eck, S. Heurtault and H. Glénat, *Appl. Surface Sci.* **314** (2014) 415–425.
- [28] S. Neuville, Carbon Structure Analysis with Differentiated Raman Spectroscopy (Lambert Academic Publishing Eds.), 2014, ISBN978-3-659-48909-9.
- [29] S. Neuville, *Surf. Coat. Technol.* **206** (4) (2011) 703.
- [30] F. Tuinstra and J.L. Koenig, *J. Phys. Chem.* **53** (1979) 1126.
- [31] P.V. Huong, *Diamond Related Mater.* **1** (1991) 33.
- [32] B. Gervais, M. Beuve, G.H. Olivera and M.E. Galassi, Numerical simulation of multiple ionization and high LET effects in liquid water radiolysis, *Radiation Phys. Chem.* **75** (2006) 493–513.
- [33] S.O. Kucheyev, *Ion Beam Processing*, Handbook of Material Processing, Chapter III, R. Groza (Ed.), Taylor and Francis Group CRC Press, Boca Raton, Florida, 2007.
- [34] T.E. Derry, Thesis /Dissertation Ion channelling in diamond. University of the Witwatersrand, Johannesburg (South Africa), 1978, Iaea. Org/inis/collection/NCLCollectionStore/Public/10/446/10446597.
- [35] B. Schmiedeskamp, P. Jonk, H.E. Roosendaal and H.O. Lutz, *J. Nucl. Instr. Methods Phys. Res. Section B* **17** (4) (1986) 309–313.
- [36] M. Moneta and J. Czerbniak, Influence of electron exchange on planar channeling of protons in diamond, *Nucl. Instr. Methods Phys. Res. Section B* **48**(1) (1990) 142–144.
- [37] A.V. Bagulya, O.D. Dalkarov, M.A. Negodaev, A.S. Rusetskii, A.P. Chubenko, V.G. Ralchenko and A.P. Bolshakov, Channeling effect in polycrystalline deuterium-saturated CVD diamond target bombarded by deuterium ion beam, *Phys. Ins.Det.* (2014) 1-8. ArXiv: 1408. 7109. DOI: 10.1016/j.nimb.2015.01.021. On-line Cornell University Library. Ithaca, NY.
- [38] D. Schroyen, M. Bruggeman, I. Dezsai and G. Langouche, Ion Implantation in highly oriented pyrolytic Graphite, *Nucl. Instr. Methods Phys. Res. Section B* **15** (1986) 341–343.
- [39] A.V. Krashenninnikov and K. Nordlund, Channeling of heavy ions through multi-walled carbon nanotubes, *Nucl. Instr. Methods Phys. Res. Section B* **228** (2005) 21–25.
- [40] D. Borka, S. Petrović and N. Neskovi, Channeling of protons through carbon nanotubes (2011). ArXiv: 1111. 1905v1 (Cond-Mat.Mes-Hall) (2011)1–58. On-line Cornell University Library. Ithaca, NY.
- [41] S. Neuville, New Application Perspective for Tetrahedral Amorphous Carbon Coatings QScience Connect 2014:8 <http://dx.doi.org/10.5339/connect.2014.8>.
- [42] L. Eyges, Physics of the Moessbauer effect, *Am. J. Phys.* **33** (10) (1965) 790–802.
- [43] V. Schuenemann and H. Paulsen, *Moessbauer Spectroscopy*, Wiley, New York, 2007. ISBN 978-0-470-03217-6.
- [44] R.W. Cahn and P. Haasen (Eds.), *Physical Metallurgy*, Fourth Edition, Elsevier, Amsterdam, 1996. ISBN: 978-0-444-89875-3.
- [45] T.J. Carter and L.A. Cornish, *Eng. Failure Analysis* **8**(2) (2001) 113–121.
- [46] M.S. Dresselhaus and R. Kalish, *Ion Implantation in Diamond, Graphite and Related Materials*, Springer, Berlin, 1992.
- [47] L. Schlapbach and A. Züttel, Review article hydrogen-storage materials for mobile applications, *Nature* **414** (2001)353–358.
- [48] D.F. Shriver, P.W. Atkins and C.H. Langford, *Inorganic Chemistry*, Oxford University Press, New York, 1989, p. 337.
- [49] O.J. A. Schueller, S.T. Brittain, C. Marzollin and G.M. Whitesiders, Fabrication and characterization of glassy carbon

- MEMS, *Chem. Mater.* **9**(6) (1997) 1399–1406 DOI: 10.1021/cm960639v
- [50] Y. Lin, L. Zhang, H.K. Mao, P. Chow, Y. Xiao, M. Baldini, J. Shu and W. Mao, *Phys. Rev. Lett.* **107** (2011) 175504.
- [51] Q. Zhang, M. Ju, L. Chen and X.C. Zeng, Differential permeability of proton isotopes through graphene and graphene analogue monolayer, *J. Phys. Chem. Lett.* **7** (17) (2016) 3395–3400.
- [52] J. Wagner, M. Ramsteiner, C. Wild and P. Koidl, EMRS XVII, Proceedings by P. Koidl and P. Oelhafen, Les Editions de la Physique. Paris (France), 1987, p. 351.
- [53] Y. Wang, D. Connétable and D. Tanguy, *Phys. Rev. B* **91** (2015) 094106 44.
- [54] P. Jakupi, J.J. Noel and D.W. Shoesmith, *Electrochemical and Solid States Lett.* **13**(3) (2010) C1–C3.
- [55] M.A. Stopher, P.E.J. Rivera-Diaz-del-Castillo, *Mat. Sci. Technol.* **32** (11) (2016) 1184–1193.
- [56] V. Demetriou, Study of the Effect of Hydrogen charging on the tensile properties and microstructure of four variant heat treatments of alloy 718, *Int. Conf. Adv. Energy Materials*, AEM-2016, Guildford, UK, ID 54.
- [57] A. Ohl and J. Röpke, *Diamond and Related Materials* **1** (1992) 243.
- [58] P. Roca I Cabarrocas and N. Layadi, *J. Vac. Sci. Technol. A* **16** (2) (1998) 436.
- [59] P.W. May, M. Clegg, T.A. Silva, H. Zanin, O. Fatibello-Filho, V. Celorrio, D.J. Fermin, C.C. Welch, G. Hazell, L. Fisher, A. Nobbse and B. Sue, Doped diamond-coated ‘black silicon’ as a promising material for high-surface-area electrochemical electrodes and antibacterial surfaces, *J. Mater. Chem. B* **4** (2016) 5737–5746.
- [60] X. Liu, P. Coxon, M. Peters, B. Hoex, J. Cole, D. Fray, Black silicon: fabrication methods, properties and solar energy applications, *Energy Environ. Sci.* **7** (10) (2014) 3223–3263.
- [61] L. Fayette, B. Marcus, M. Mermoux, G. Tourillon, K. Laffon, P. Parent and F. Le Normand, *Phys. Rev. B* **57** (22) (1998) 1412.
- [62] J. Robertson, *Diamond and Related Materials* **3** (1994) 732.
- [63] N.W. Ashcroft and N.D. Mermin, *Solid State Physics*, Cornell University, College Publishers Harcourt, New York, 1976, ISBN 978-0-03-083993-1.
- [64] A. Houari, S.F. Matar and V. Eyert, *Phys. Rev. B* **82** (2010) 241201.
- [65] B. Aufray, A. Kara, S. Vizzini, H. Oughaddou, C. Léandri, B. Ealet and G. Le Lay, *Appl. Phys. Lett.* **96** (18) (2010) 183102.
- [66] J.L. Bredas and G.B. Street, EMRS Meeting XVII, Proceedings by P. Koidl and P. Oelhafen, Les Editions de la Physique (Eds.), 1987, p. 237.,
- [67] D.G. Liu, J.P. Tu, C.F. Hong, C.D. Gu and S.X. Mao, *Surf. Coat. Technol.* **205** (2010) 152.
- [68] P.K. Bachmann and W. vanEckervort, *Diamond and Related Materials* **1** (1992) 1021.
- [69] Y.Y. Lin, H.W. Wei, K.C. Leou, H. Lin, C.H. Tung, M.T. Wei, C. Lin, C.H. Tsai, *JVST B* **24**(1) (2006) 97.
- [70] M. Endo, Grow Carbon fibers in the vapor phase, *Chemtech* (September 1988) 568576.
- [71] J. Campos-Delgado, Y.A. Kim, T. Hayashi, A. Morelos Gomez, M. Hofmann, M. Endo, H. Muramatsu, H. Terrones, R.D. Shull, M.S. Dresselhaus and M. Terrones, *Chem. Phys. Lett.* **469** (2009) 177182.
- [72] G. Flamant, R. Guillard and D. Laplaz, *Le Vide* **2,4** (300) (2001) 266.
- [73] S. Weissmantel, G. Reisse and D. Rost, *Surf. Coat. Technol.* **188–189** (2004) 268.
- [74] A. Grill, *Surf. Coat. Technol.* **94,95** (1997) 507–513. .
- [75] F. Sato, N. Saito, Y. Hirano, A.H. Jayatissa, K. Takizawa, S. Kavado, T. Kato, H. Sigiyaama and M. Ando, *J. Vac. Sci. Technol.* **16** (4) (1998) 2553.
- [76] S. Neuville, A. Taggliaferro, Y. Bounouh, S. Vallon, R. Etemadi, J. Perrin, CIP 95 Antibes, Le Vide, Sciences, Techniques et Applications, 64 by SFV (Eds), Paris (France), Vol. 275 (1995).
- [77] S. Neuville, *Diamond and Related Materials* **11** (2002) 1721–1730.
- [78] S. Anders, J.W. Ager III, G.M. Pharr, T.Y. Tsui and I.G. Brown, *Thin Solid Films* **308,309** (1997) 186.
- [79] A.P. Badzian, P.K. Bachmann, T. Hartnett, T. Badzian and R. Messier, EMR Meeting XVII, Proceedings by P. Koidl and P. Oelhafen, Les Editions de la Physique Paris (France) (1987) 63.
- [80] K.M. McNamara, K.K. Gleason, G.J. Vestyck and J.E. Butler, *Diamond and Related Materials* **1** (1992) 1145.
- [81] K.E. Spear, A.W. Phelps, W.B. White, *J. Mater. Res.* **5** (1990) 2277.
- [82] D. Rai, H. Joshi, A.D. Kulkarni, S.P. Gejji and R.K. Pathak, Electric field effects on aromatic and aliphatic hydrocarbons, *J. Phys. Chem. A* **111**(37) (2007) 9111–9121.
- [83] K.S. Sankara-Reddy and M. Satyam, Structural ordering of diamond-like carbon films by applied electric field, *Solid State*

- Commun.* **93** (10) (1995) 797799.
- [84] S. Neuville, *Sensors and Actuators B* **121** (2) (2007) 436.
 - [85] C.E. Borroni-Bird and D.A. King, *Rev. Sci. Instrum.* **62** (9) (1991) 2177.
 - [86] S. Neuville and A. Matthews, *MRS Bulletin* **22** (9) (1997) 22–26.
 - [87] M. Iwaki, K. Takahashi and A. Sekiguchi, *J. Mat. Res.* **5** (1990) 2562.
 - [88] D. Beeman, J. Silvermann, R. Lynds and M.R. Anderson, *Phys. Rev. B* **30** (1984) 870.
 - [89] J. Robertson and E.P. O'Really, *Phys. Rev. B* **35** (1987) 2946.
 - [90] Y. Pauleau, in C. Donnet and A. Erdemir, *Tribology of DLC*, Springer, New York, 2008, 102.
 - [91] A. Erdemir, M. Switala, R. Wei and P. Wilbur, *SurFace and Coatings Technology* **50** (1991) 17.
 - [92] X.H. Wang, G.H.M. Ma, W. Zhu, J.T. Glass, L. Bergman, K.F. Turner, R.J. Nemanich, *Diamond Relat. Mater.* **1** (1992) 828.
 - [93] J.O. Sofo, A.S. Chaudhari and G.D. Barber, *Phys. Rev. B* **75**, **153401** (2007). “Graphane: A two-dimensional hydrocarbon”. *Physical Review B* **75** (15) (2007) 153401–153404.
 - [94] D.C. Elias, R.R. Nair, T.M.G. Mohiuddin, S.V. Morozov, P. Blake, M.P. Halsall, A.C. Ferrari, D.W. Boukhvalov, M.I. Katsnelson, A.K. Geim and K.S. Novoselov, *Science* **323** (5914) (2009). Evidence for Graphane.
 - [95] J.C. Tolédano and P. Tolédano, *The Landau Theory of Phase Transitions*, World Scientific, Singapore, 1987, ISBN 9971500256.
 - [96] P. Tolédano and V. Dmitriev, *Reconstructive Phase Transitions in Crystals and Quasicrystals*, World Scientific, Singapore, 1996, ISBN 9810223641.
 - [97] T.S. Jackson, G. Möller and R. Roy, Geometric stability of topological lattice phases, *Nature Communications* **6**(Article number: 8629) (2015). doi:10. 1038/ncomms9629.
 - [98] G.K. Sunnardianto, Storing-hydrogen process on graphene activated by atomic-vacancy, *Int. Conf.on Adv. Energy Materials AEM-2016*, Guildford, UK, ID 54.
 - [99] N. Martsinovich, Computational design of carbon nitride photocatalysts for water splitting, *Int. Conf. on Advanced Energy Materials AEM-2016*, Guildford, UK. ID 132.
 - [100] N.B. Makarova, Catalytic naphthalene condensation as a means of producing nanostructured graphene: computational studies, *Int. Conf. on Advanced Energy Material Guildford AEM-2016*, Guildford, UK. ID133.
 - [101] P. Klán and J. Wirz, *Photochemistry of Organic Compounds: From Concepts to Practice*, Wiley, Chichester, 2009, ISBN 978-1405190886.
 - [102] J. Rouzaud, A. Oberlin and C. BenyBassez, *Thin Solid Films* **105**(1) (1983) 75–86.
 - [103] A.C. Ferrari, *Diamond and Related Materials* **11**(3–6) (2002) 1053–1061.
 - [104] L.M. Malard, M.A. Pimenta, G. Dresselhaus and M.S. Dresselhaus, Raman spectroscopy in graphene, *Phys. Reports* **473**(5–6) (2009) 51–87.
 - [105] M.S. Dresselhaus, A. Jorio, A.G. SouzaFilho and R. Saito, *Phil. Trans. Roy. Soc. A* **368** (2010) 5355–5377.
 - [106] L.G. Cançado, M.A. Pimenta, B.R. Neves, M.S. Dantas and A. Jorio, *Phys. Rev. Lett.* **93** (2004) 247401.
 - [107] L.G. Cançado, M.A. Pimenta, B.R. Neves, G. MedeirosRibeiro, T. Enoki, Y. Kobayashi, K. Takai, M.S. Dantas, K. Fukui, M.S. Dresselhaus, R. Saito and A. Jorio, *Phys. Rev. Lett.* **93** (2004) 047403.
 - [108] B. Marcus, L. Fayette, M. Mermoux, L. Abello and G. Lucazeau, *J. Appl. Phys.* **14** (1994) 3463.
 - [109] M. Lazzeri, C. Attaccalite, L. Wirtz and F. Mauri, *Phys. Rev. B* **7** (2008) 081406.
 - [110] B. Dischler, EMRS Meeting XVII, Proceedings by P. Koidl and P. Oelhafen, Les Editions de la Physique (Eds) Paris (France) (1987) 189.
 - [111] P.V. Huong, B. Marcus, M. Mermoux, D.K. Veirs and G. Rozenblatt, *Diamond and Related Materials* **I** (1992) 869.
 - [112] S. Praver, F. Ninio and I. Blanchonette, *J. Appl. Phys.* **68** (1990) 2361.
 - [113] T.E. J. Dallas, Thesis Structural Phases of Disordered Carbon Materials, Texas Tech University, 1996.
 - [114] R. Rammamurti, V. Shanov, R. Singh, S. Mamedov and P. Boolchand, *J. Vac. Sci. Technol. A* **24**(2)(2006) 179.
 - [115] R. Singh, C.V. Raman and the discovery of the Raman Effect, *Phys. in Perspective (PIP)* **4** (4) (2002) 39420.
 - [116] R. Zallen, *The Physics of Amorphous Solids*, Wiley, New York, 1983.
 - [117] J. Maultzsch, S. Reich and C. Thomsen, *Phys. Rev. B* **70** (2004) 155403.
 - [118] R. Saito, A. Jorio, A.G. Souza Filho, G. Dresselhaus, M.S. Dresselhaus and M. A. Pimenta, *Phys. Rev. Lett.* **88** (2002) 027401.

- [119] Y.N. Xu, D. Zhan, L. Liu, H. Suo, Z.H. Ni, T.T. Nguyen, C. Zhao and Z. X. Shen, *ACS Nano* **5** (1) (2011) 142.
- [120] Y.M. You, Z.H. Ni, T. Yu and Z.X. Shen, *Appl. Phys. Lett.* **93** (2008) 163112.
- [121] B. Fakrach, A. Rahmani, H. Chadli, K. Sbai and J.L. Sauvajol, *Physica E* **41**(2009) 1800.
- [122] K.A. Ritter and J.W. Lyding, The influence of edge structure on the electronic properties of graphene quantum dots and nanoribbons, *Nat. Mater.* **8** (2009) 235–242.
- [123] U. Ritter, P. Scharff, C. Siegmung, O.P. Dimmytrenko, N.P. Kulisch, Y.I. Priylutsky, N.M. Belyi, V.A. Gubanov, S.V. Lizunova, V.G. Poroshin, V.V. Shlapatskaya and H. Bernas, *Carbon* **44**(2006) 2694.
- [124] A.J. Smith and D.L. Trimm, *The Preparation of Skeletal Catalysts*, *Ann. Rev. Mat. Res.* **35** (2005) 127–142.
- [125] W.M. Mueller, J.P. Plackedge and G.G. Libowitz, *Transition Hydrides*, Academic Press, New York, London, 1968.
- [126] L.M. Currie, V.C. Hamister, H.G. Mac Pherson, *The Production and Properties of Graphite for Reactors*, National Carbon Company, 1955.
- [127] M. Fleischmann, S. Pons, M.W. Anderson, L.J. Li and M. Hawkins, Calorimetry of the palladium–deuterium-heavy water system, *J. Electroanal. Chem.* **287** (1990) 293–348.
- [128] F. Crundwell, M. Moats, V. Ramachandran, T. Robinson and W.G. Davenport, *Extractive Metallurgy of Nickel, Cobalt and Platinum Group Metals*, Elsevier, Amsterdam, 2011. ISBN: 978-0-08-096809-4.
- [129] V.V. Cheianov and V.I. Fal’ko, Friedel oscillations, impurity scattering, and temperature dependence of resistivity in graphene, *Phy. Rev. Lett.* **97** (22) (2006) 226801–226804.
- [130] S. Neuville, Superconductivity described with electron–phonon synchronic coupling, *1st Int. Conf. on Advanced Energy Materials*, 2016, ANM-3, Guildford, UK, to be published in Materials to Day.
- [131] R.J. Kamaladasa and Y.N. Picard, Science, Technology, and Application. A. Méndez-Vilas and J. Díaz (Eds.), 2010, Formatex Research center C/ Zurbarán 1, 2^o - Oficina 1. 06002 Badajoz, Spain.
- [132] J.D. Lawson, Some Criteria for a power producing thermonuclear reactor, (Technical report) (1955), Atomic Energy Research Establishment, Harwell, Berkshire, U.K., A.E.R.E., GP/R 1807.
- [133] C. Patrignani, K. Agashe, G. Aielli, C. Amsler, M. Antonelli, D.M. Asner, H. Baer, Sw. Banerjee, R.M. Barnett, T. Basaglia, C.W. Bauer, J.J. Beatty, V.I. Belousov, J. Beringer, S. Bethke, H. Bichsel, O. Biebel, E. Blucher, G. Brooijmans, O. Buchmueller, V. Burkert, M.A. Bychkov, R.N. Cahn, M. Carena, A. Ceccucci, A. Cerri, D. Chakraborty, M.-C. Chen, R.S. Chivukula, K. Copic, G. Cowan et al., (Particle Data Group), *Rev. Particle Phys., Chinese Physics C* **40** (2016) 100001.
- [134] N. Bohr, *Philosophical Magazine* **26** (6) (1913) 1–25.
- [135] Hideki Yukawa, Meson theory in its developments, Nobel Lecture, December 12, 1949.
- [136] V. Dubinko, Nuclear catalysis mediated by localized anharmonic vibrations, *Cond-Mat. Mtrl-Sci.* (2015) 1–36. ArXiv: 1510.06081v1. On-line Cornell University Library, Ithaca, NY.
- [137] L. de Broglie, The wave nature of the electron, Nobel Lecture, December 12, (1929).
- [138] L. Landau and E. Lifchitz, *Physique Theorique*. Coll. MIR. Ellipses Eds. 1997
- [139] P. Grangier, G. Roger and A. Aspect, *Europhys. Lett.* **1** (4) (1986) 173–179.
- [140] S. Massidda, Superconductivity Report from BCS to modern electronic theory, University of Cagliari, 2015.
- [141] A. Einstein and N. Rosen, The particle problem in the general theory of relativity, *Phys. Rev.* **48**(1935)73.
- [142] A.Y. Liu and M.L. Cohen, *Phys. Rev. B* **41** (1990) 10727.
- [143] E. Schrödinger Erwin, An undulatory theory of the mechanics of atoms and molecules, *Phys. Rev.* **28**(6) (1926) 1049–1070.
- [144] J.F. Geneste, *Physique de l’esprit des Lois*, 951(2010) Cepadue Editions, Sciences, Toulouse, France, ISBN: 9782854289510.
- [145] J.D. Anderson, *Governing Equations of Fluid Dynamics*, in *Computational Fluid Dynamics*, J.F. Wendt (Ed.), 3rd edition, Springer-Verlag, Berlin, Heidelberg, 2009.
- [146] C. Yulksel, PhD Dissertation, Real Time Water Waves with Wave Particles, Texas A&M University, 2010.
- [147] K. Kunisch and S. Volkwein, Galerkin proper orthogonal decomposition methods for a general equation in fluid dynamics, *SIAM J. Numer. Anal.* **40**(2) (2006) 492–515.